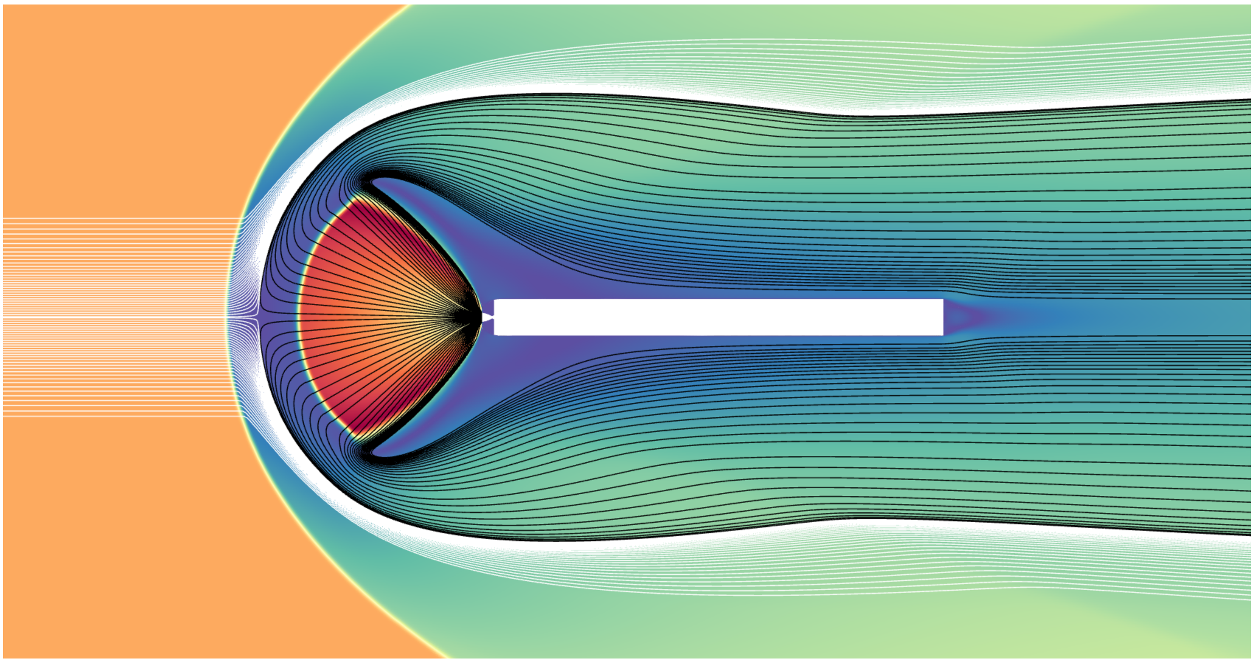

Aerothermal Analysis of a Rocket Booster during Reentry and Retro-propulsion

Master's thesis in Applied Mechanics

MOHAMMED KASSEM
AARON ROVELSTAD

DEPARTMENT OF MECHANICS AND MARITIME SCIENCE
CHALMERS UNIVERSITY OF TECHNOLOGY
Gothenburg, Sweden 2025
www.chalmers.se

Master's thesis 2025

Aerothermal Analysis of a Rocket Booster during Reentry and Retro-propulsion

MOHAMMED KASSEM
AARON ROVELSTAD

Department of Mechanics and Maritime Science
Division of Fluid Dynamics
Chalmers University of Technology
Gothenburg, Sweden 2025

Aerothermal Analysis of a Rocket Booster during Reentry and Retro-propulsion

Supervisor: Jan Östlund, GKN Aerospace Sweden AB
Supervisor: Alexandre Capitao Patrao, GKN Aerospace Sweden AB
Examiner: Carlos Xisto, Department of Mechanics and Maritime Science

Master's Thesis 2025
Department of Mechanics and Maritime Science
Division of Fluid Dynamics
Chalmers University of Technology
SE-412 96 Gothenburg
Telephone +46 31 772 1000

Cover: CFD simulation of the rocket booster during reentry with retro-propulsion.

Typeset in LaTeX
Printed by Chalmers Reproservice
Gothenburg, Sweden 2025

Aerothermal Analysis of a Rocket Booster during Reentry and Retro-propulsion
MOHAMMED KASSEM
AARON ROVELSTAD
Department of Mechanics and Maritime Science
Chalmers University of Technology

Abstract

In recent years the use of re-usable launch vehicles for payloads intended for earth orbits has gained popularity where retro-propulsion, when the engines are firing in the same direction of flight, is used to land the vehicles. Private companies such as SpaceX, Blue Origin and Rocket lab are developing reusable rocket boosters where the most prominent is the Falcon 9 rocket by SpaceX. To reduce costs for European space travel the European Space Agency (ESA) has funded several projects within reusable rocket boosters. The RETPRO and RETALT project was done to investigate the system components of a reusable rocket booster along with a CFD and wind tunnel verification of aerothermal calculations. GKN Aerospace is involved in the development of the Prometheus engine which utilizes a gas generator cycle that runs on liquid methane and liquid oxygen. This engine will power the European rocket demonstrator Themis which is a proof of concept of a reusable first stage rocket. In this thesis Computational Fluid Dynamics simulations were used to analyse the aerodynamic and thermodynamic loads on and around the nozzles. The heat transfer coefficient (HTC), temperatures, pressures and heat flux were investigated at the start and end of a reentry burn. Different chemical models were investigated with the aim to find the appropriate model in terms of computational cost and accuracy for simulating the reentry and retro-propulsion. It was found that for reentry without retro-propulsion the frozen chemistry model provides sufficient accuracy with lower computational cost compared to the chemical non-equilibrium model and was therefore chosen for all simulations when the engines were off. With retro-propulsion, however, the chemical non-equilibrium model was needed to accurately model the temperatures and heat flux on the rocket walls. It was concluded from the results that the largest HTC where found at the end of the burn and when the engines are off the highest HTC is located near the throat of the outer nozzles while during retro-propulsion it's the center nozzle that is most exposed to high local HTC near the nozzle exit.

Keywords: Computational Fluid Dynamics, Rocketry, Reentry, Retro-propulsion, Hypersonic flow, Compressible flow, $k - \omega$ SST, Chemistry models

Acknowledgements

First of all we would like to express our gratitude to our supervisors Jan Östlund and Alexandre Capitao Patrao at GKN Aerospace Sweden AB. Their insights and support in this project has been invaluable, this includes everything from CFD modeling and meshing to just casually talking about how a rocket engine works. This project has been one of the most interesting thing we have done during our studies and to have been able to work with rockets has been something truly exciting. We would also like to thank Carlos Xisto for being our examinator for this thesis. Lastly we would like to thank Tomas Fernström, the department manager and all the other people at the department for welcoming us and helping us with this project. A special thanks goes to Alexander Rodin, Merim Sakic and Jonathan Mårtensson, whom have not only provided enormous support, but also made the time at GKN memorable and rewarding.

Mohammed Kassem and Aaron Rovelstad, Gothenburg, 2025

List of Acronyms

Below is the list of acronyms that have been used throughout this thesis:

RLTS	Return To Launch Site
DRL	Down Range Landing
CFD	Computational Fluid Dynamics
ESA	European Space Agency
HTC	Heat Transfer Coefficient
FLPP	Future Launchers Preparatory Programme
DLR	German Aerospace Center (Deutsches Zentrum für Luft- und Raumfahrt)
RANS	Reynolds-Averaged Navier-Stokes
TIC	Truncated Ideal Contour nozzle
RL	Rocket Lengths
ISA	International Standard Atmosphere

Nomenclature

Below is the nomenclature of variables that have been used throughout this thesis.

Computational Fluid Dynamics Variables

ρ	Density (kg/m^3)
v_i, v_j	Velocity components (m/s)
x_i, x_j	Spatial coordinates (m)
t	Time (s)
P	Pressure (Pa)
f_i	External force per unit mass (N/kg)
e_0	Total internal energy per unit mass (J/kg)
σ_{ij}	Stress tensor (Pa)
S_{ij}	Strain rate tensor (1/s)
δ_{ij}	Kronecker delta (-)

Turbulence Variables

$\bar{v_i}, \bar{p}$	Mean velocity and pressure (m/s, Pa)
v_i', p'	Fluctuating velocity and pressure components (m/s, Pa)
$\rho\overline{v_i'v_j'}$	Reynolds stress tensor (Pa)
ν_t	Turbulent eddy viscosity (m^2/s)
k	Turbulent kinetic energy (m^2/s^2)
ϵ	Turbulent dissipation rate (m^2/s^3)
ω	Specific dissipation rate (1/s)
C_μ	Model constant (-)
$\sigma_{k1}, \sigma_{\omega 1}, \sigma_{k2}, \sigma_{\omega 2}$	Turbulence model coefficients (-)
$\beta^*, \beta_1, \beta_2$	Dissipation coefficients (-)

γ_1, γ_2	Production coefficients (-)
κ	Von Kármán constant (-)
F_1, F_2	Blending functions (-)
Ω	Vorticity magnitude (1/s)
a_1	Empirical model coefficient (-)

Compressible Flow Variables

τ	Compressibility (1/Pa)
υ	Specific volume (m^3/kg)
a	Speed of sound (m/s)
R	Specific gas constant (J/(kg K))
T	Temperature (K)
γ	Ratio of specific heats (-)
T_0	Total (stagnation) temperature (K)
P_0	Total (stagnation) pressure (Pa)
M	Mach number (-)

Heat Transfer Variables

q	Heat flux (W/m^2)
h	Heat transfer coefficient (W/(m^2 K))
T_w	Wall temperature (K)
T_∞	Freestream temperature (K)
T_{aw}	Adiabatic wall temperature (K)
q_c	Convective heat flux (W/m^2)
Nu_L	Nusselt number (-)
L	Characteristic length (m)
k	Thermal conductivity (W/(m K))

Retropropulsion and Plume Variables

C_T	Thrust coefficient (-)

T	Thrust (N)
p_∞	Freestream dynamic pressure (Pa)
A_m	Model base area (m^2)
M_∞	Freestream Mach number (-)
p_e	Nozzle exit pressure (Pa)
A_e	Nozzle exit area (m^2)
A	Reference area (m^2)
γ_j, γ_∞	Heat capacity ratios in jet and freestream (-)
EPR	Nozzle exit pressure ratio (-)

CHEMKIN Format Variables

c_p	Specific heat at constant pressure (J/(kg K))
R	Universal gas constant (J/(kmol K))
H	Enthalpy (J)
S	Entropy (J/K)
T	Temperature (K)
a_n	CHEMKIN polynomial coefficients (-)

Contents

List of Figures

List of Tables

1

Introduction

1.1 Background

The development of large scale rockets started during the WWII when Germany developed the V-2 rocket, the first rocket to reach the Kármán Line at an altitude of 100 km. After the war ended countries such as the USA and the Soviet Union started developing rockets with the intention of space exploration and a competition of putting the first person in space started. Later on more countries joined as focus was shifted into putting advanced technologies, such as satellites, into space [1].

Retro-propulsion, firing the engines in the same direction of travel, for rockets is a topic that has been discussed for many decades and is found in literature since the 1950s. Earlier, however, it was most often mentioned with regards to landing on celestial bodies. In later years re-usable launch vehicles used for payloads intended for earth orbits has become a big topic to reduce cost and increase sustainability [2, 3]. Today private companies', such as SpaceX, Blue Origin and Rocket Lab, are in the process of developing reusable rocket boosters, where the most prominent and commercially used is SpaceX's Falcon 9 rocket (introduced 2014) and Falcon Heavy rocket (introduced 2019) [2, 4]. To keep these private companies' advantage, limited information and validation results are published of their launchers and missions. Most of the validation results that has been published has been normalized and therefore has limited use in the field of research and since the cost of launch is much too high for most research institutes, the knowledge within this area is very limited [2].

Following the American companies, European Space Agency (ESA) has funded several projects within reusable rocket boosters to reduce costs for European space travel, improve flexibility and strengthen European launch operations on the global market [4]. The main project is Future Launchers Preparatory Programme (FLPP) of which the projects RETPRO and RETALT are a part of. RETALT is a project where the system components of a reusable rocket booster is researched while RETPRO is a CFD and wind tunnel verification of aerothermal calculations [2]. Another project, CALLISTO, a collaboration between CNES (France), DLR (Germany) and JAXA (Japan) has made significant research in the field of retro-propulsion and are currently developing a rocket as a demonstrator of the concept [5].

GKN Aerospace is involved in the development of the Prometheus engine which will power the rocket demonstrator Themis. The Prometheus engine is powered by a gas generator cycle which runs on liquid methane and liquid oxygen [6]. Themis will be a demonstrator for a future Ariane rocket which will demonstrate the possibility of a reusable first stage rocket. As GKN is part of developing the Prometheus engine it is of interest to know what kind of loads it will experience during the reentry and retro-propulsion of the rocket.

1.2 Earlier work

The state of the art when it comes to reentry and retro-propulsion experiments is the use of numerical tools, such as CFD [3]. There has been physical experiments, conducted in blow-down wind tunnels to simulate reentry without retro-propulsion where the high Mach numbers of hypersonic flying conditions can be simulated by accelerating a gas, often air, through a high expansion ratio nozzle. However, due to conservation of energy, when accelerating the flow the static temperature decreases as the total temperature is set constant resulting in different thermal properties compared to flight conditions as well as resulting in lower velocities due to decrease in speed of sound as the mach number needs to match [2]. Due to fire hazard, starting a rocket engine in a wind tunnel is generally not possible, limiting experimental testing to cold exhaust where one can investigate plume-air interaction, shockwave and rocket body exhaust immersion but very limited in thermal validations [3, 2]. In other words, reentry and retro-propulsion relies heavily on numerical simulations without much validation data [3].

Turbulence modeling is necessary to be be able to correctly capture the turbulence effect on the behavior of shockwaves and it has been noted from studies that RANS based models cannot correctly predict the interaction of turbulence with shocks. This is due to RANS limitations in not being able to taking the unsteady motion into account [2]. A study was done on retro-propulsion on a hydrogen-fueled engine which compared three different turbulence models (Spalart-Allmaras, $k-\omega$ SST and Wilcox $k-\omega$) and the difference between chemical models as it compared a reacting non-equilibrium flow and a frozen flow for a subsonic retro-propulsion. The results showed a significant difference in the shape and length of the plume between different turbulence models especially with the Spalart-Allmaras model. It also noted different temperatures in the plume when comparing a reacting flow and a frozen flow with larger temperatures in the reacting one. Both post combustion and turbulence model affects the temperature but as the study regards a hydrogen-fueled engine the post combustion will be limited compared to methane and kerosene based fuels which have been shown to have more post combustion effects [7, 2]. It has also been noted that for multi-nozzle configurations there will be strong oscillations between different modes of the plume (further discussed in 2.5) which both RANS and URANS cannot capture and therefore requires higher fidelity simulations. Another large uncertainty with RANS was seen with the prediction of the surface heat loads. But due to the low CPU requirements for RANS models it's seen as the only option for comprehensive design and development [2].

In general for combustion inside a combustion chamber with high pressures and temperatures, the chemical timescales for combustion is very small and the flow timescales large, making chemical equilibrium a good assumption. However, once ejected through the nozzle the timescales for post combustion is vastly different where the flow timescale is small due to the high velocities and large chemical timescales due to slow reactions, sometimes exceeding flow timescales by several orders of magnitude, making frozen chemistry a good assumption. This means that there are regions with high, low and intermediate Damköhler number(Da) which is the ratio between the flow- and chemical timescale, making frozen chemistry, chemical equilibrium and chemical non-equilibrium all good approximations in different regions of the flow [2]. Studies comparing chemistry models in supersonic retro-propulsion has shown that for hydrogen fuels, the rocket wall temperature was about 200 K higher for reacting chemistry while for the carbon based kerosene fuel, the difference was nearly 700 K (corresponding to 50% error). This shows that the choice of fuel will heavily impact the effects of post combustion, and therefore also the effects of chemistry models [2].

Studies have been made comparing the air models during reentry and one notable example is Zhao et. al. (2020) [8] studying the heat flux at different Mach numbers. They determined that at an altitude of 50 km and a reentry speed of Mach 9, the models resulted in similar heat flux making the 5-species model an appropriate choice. At Mach 15 they started to deviate where 7-species model was appropriate and finally at Mach 23 the full 11-species model was appropriate. A similar study was made by Zhao et. al. (2023) [9] comparing temperatures of Gupta, Park and Dunn-Kang air models (all containing different 5-, 7- and 11-species models). They concluded that up until Mach 29 the temperature, pressure and heat flux is comparable, meaning that 5-species model is sufficient, however at Mach 34 and Mach 39 they deviate rapidly making making 7- and 11-species models necessary.

For landing the first stage of a rocket there are two options, both displayed in figure 1.1. Either to bring back the booster to the launch site, called return to launch site (RTLS), or let the booster follow a ballistic trajectory after separation and land at a site further away, called a downrange landing (DRL). For a RTLS mission the booster will perform a boostback burn after separation. This is a burn which is done to reverse the horizontal component of the velocity to direct the velocity back to the launch site, this is done while the vertical component of the acceleration stays fairly unchanged. After reaching it's apogee and starting the descent back down, the booster will initiate the reentry burn. The reentry burn will help reduce the velocity as aerodynamic drag is minimal at the high altitudes due to low atmospheric density and will also help shield the components from high heat loads. After the velocities has decreased and the rocket is at lower altitudes with higher atmospheric densities, the atmospheric drag is utilized to slow down the booster until it's near enough to the ground to perform a last landing burn. In contrast to RTLS, the DRL trajectory does not perform a boostback burn but will coast until reaching the apogee, start its descent and do a reentry burn and then glide to the landing pad and perform a landing burn. A comparison of the different trajectories was done on a Falcon 9 which showed that stage separation occurs 10 seconds earlier for RTLS compared to

DRL. The earlier separation, together with the boostback burn, results in a decrease of the velocity at the reentry burn for RTLS compared to a DRL [2].

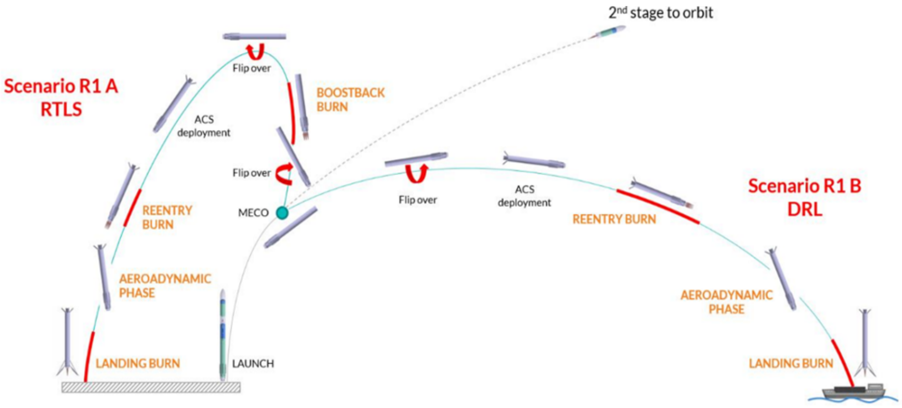

Figure 1.1: Landing scenarios: Return To Launch Site (RTLS), Down Range Landing (DRL) [10].

Due to limitations in time, the scope of this thesis will be to only investigate DRL. Comparing these two scenarios it has been noted that DRL is expected to experiences higher velocities during retro-propulsion compared to RTLS and therefore have higher loads. The main difference, other than the velocity, is that RTLS performs a boostback burn, however at the high altitudes of boostback burn there is very limited atmosphere meaning that no significant plume-air interaction to investigate. There is also the limitation on the use of computational methods as the atmospheric pressure is so low that the Navier-Stokes equations used in computational fluid dynamics (CFD) are no longer valid, exponentially increasing the complexity of the problem [2].

1.3 Aim of project

The aim of this project is to simulate the reentry and retro-propulsion of a first stage rocket booster and investigate the physical flow phenomena around the nozzles. The thermal loads and pressure loads on the nozzles will be evaluated along with the heat transfer coefficient(HTC). The main goal is to investigate the flow phenomena with engines turned on and off at the start and end of the reentry burn. A method will also be developed, and possible model reductions will be investigated. Due to limitations in time, the scope of this thesis will be to only investigate DRL. DRL was chosen over RTLS as the rocket is expected to experiences higher veloci- ties during retro-propulsion and therefore higher loads

1.4 Task and questions

The following questions will be answered during this thesis:

- How does the flow behave around the nozzles during the reentry burn.
- What are the heat loads, pressure loads and heat transfer coefficient on the nozzles during the reentry burn with and without retro-propulsion.
- What physics is present on and around the nozzles during reentry and retro-propulsion
- How can a CFD model be set up in order to investigate the thermal loads on the nozzles and what simplifications can be made.

2

Theory

In this section theory surrounding this thesis will be presented, starting with fluid dynamics and CFD, continuing with super-/hypersonic and compressible flows found in rocket reentry. Following is a short description regarding flow behaviour during retro-propulsion and finally theory of high altitude and high temperature flows will be discussed ending with chemistry and chemistry modeling.

2.1 Computational fluid dynamics

Any fluid flow is governed by the concept that mass, momentum and energy is conserved. These principles can be expressed with partial differential equations. Computational fluid dynamics is a way to numerically solve these partial differential equations with the help of Navier-Stokes equations for continuity, momentum and energy.

The continuity, momentum and energy equation is given by

$$
\begin{aligned}
\frac{\partial \rho}{\partial t} + \rho \frac{\partial v_i}{\partial x_i} &= 0, \\
\frac{\partial \rho v_i}{\partial t} + \frac{\partial \rho v_i v_j}{\partial x_j} &= -\frac{\partial P}{\partial x_i} + \frac{\partial \sigma_{ij}}{\partial x_j} + \rho f_i, \\
\frac{\partial \rho e_0}{\partial t} + \frac{\partial \rho e_o v_j}{\partial x_j} &= -\frac{\partial P v_j}{\partial x_j} + \frac{\partial}{\partial x_j}\left[C_p \frac{\mu}{P_r} \frac{\partial T}{\partial x_j} + v_i \sigma_{ij} \right]
\end{aligned}
\tag{2.1}
$$

where e_0 is the total internal energy and the stress tensor σ_{ij} is defined as

$$
\begin{aligned}
\sigma_{ij} &= 2\mu S_{ij} - \frac{2}{3}\mu S_{kk}\delta_{ij}, \\
S_{ij} &= \frac{1}{2}\left(\frac{\partial v_i}{\partial x_j} + \frac{\partial v_j}{\partial x_i} \right).
\end{aligned}
\tag{2.2}
$$

If the flow is turbulent, the behavior of the fluid drastically changes, and one way to solve it is by using time-averaged Navier-Stokes equation. This is done by decomposing the instantaneous velocity and pressure into a mean value and a fluctuating value, which gives

$$\begin{aligned} v_i &= \bar{v_i} + v_i' \\ p &= \bar{p} + p' \end{aligned} \tag{2.3}$$

where $\bar{v_i}$ is the mean component and v_i' is the fluctuating component. To make the derivation easier the equation for an incompressible flow with constant viscosity will be used. Putting this decomposition into the Navier-Stokes equation results in the following equation called Reynolds Averaged Navier-Stokes (RANS):

$$\begin{gathered} \frac{\partial \bar{v_i}}{\partial x_i} = 0, \\ \rho \frac{\partial \bar{v_i}\bar{v_j}}{\partial x_j} = -\frac{\partial \bar{p}}{\partial x_i} + \frac{\partial}{\partial x_j}\left(\mu \frac{\partial \bar{v_i}}{\partial x_j} - \rho\overline{v_i'v_j'}\right) \end{gathered} \tag{2.4}$$

where $\rho\overline{v_i'v_j'}$ is a new term called the Reynold's stress tensor which is unknown and needs to be modeled to be able to close the Navier-Stokes equation.

2.2 Turbulence modeling

There is a large variety of turbulence models, all approximating the Reynold's stress term differently. One way is to use different types of two-equation models which solves the turbulent kinetic energy equation and the dissipation equation. In order to calculate these, the Reynold's stress is modeled by introducing a turbulent eddy viscosity ν_t which is defined as,

$$\nu_t = C_\mu \frac{k^2}{\epsilon}. \tag{2.5}$$

With this turbulent viscosity the Boussinesq assumption is used which models the Reynold's stress as

$$-\overline{v_i'v_j'} = \nu_t\left(\frac{\partial \bar{v_i}}{\partial x_j} + \frac{\partial \bar{v_j}}{\partial x_i}\right) + \frac{1}{3}\delta_{ij}\overline{v_k'v_k'} \tag{2.6}$$

where δ_{ij} is the Kronecker delta.

2.2.1 The SST $k-\omega$ model

The SST $k-\omega$ model is an eddy-viscosity model which is a combination of the $k-\omega$ model and $k-\epsilon$ model. It uses $k-\omega$ in the inner part of the boundary layer and $k-\epsilon$ in the outer part of the boundary layer and the rest of the domain. The SST model also limits the shear stress in adverse pressure gradient regions [11]. Menter shows in [12] that by taking the original $k-\omega$ model which is defined as,

$$\begin{aligned}\frac{\partial \rho k}{\partial t}+\frac{\partial \rho u_j k}{\partial x_j}&=P_k-\beta^*\rho\omega k+\frac{\partial}{\partial x_j}\left[(\mu+\sigma_{k1}\mu_t)\frac{\partial k}{\partial x_j}\right]\\ \frac{\partial \rho \omega}{\partial t}+\frac{\partial \rho u_j \omega}{\partial x_j}&=\gamma_1 P_\omega-\beta_1\rho\omega^2+\frac{\partial}{\partial x_j}\left[(\mu+\sigma_{\omega 1}\mu_t)\frac{\partial \omega}{\partial x_j}\right]\end{aligned} \tag{2.7}$$

and the transformed $k-\epsilon$ defined as,

$$\begin{aligned}\frac{\partial \rho k}{\partial t}+\frac{\partial \rho u_j k}{\partial x_j}&=P_k-\beta^*\rho\omega k+\frac{\partial}{\partial x_j}\left[(\mu+\sigma_{k2}\mu_t)\frac{\partial k}{\partial x_j}\right]\\ \frac{\partial \rho \omega}{\partial t}+\frac{\partial \rho u_j \omega}{\partial x_j}&=\gamma_2 P_\omega-\beta_2\rho\omega^2+2\rho\sigma_{\omega 2}\frac{1}{\omega}\frac{\partial k}{\partial x_j}\frac{\partial \omega}{\partial x_j}+\frac{\partial}{\partial x_j}\left[(\mu+\sigma_{\omega 2}\mu_t)\frac{\partial \omega}{\partial x_j}\right]\end{aligned} \tag{2.8}$$

where ϵ is rewritten as a function of k and ω and

$$\begin{aligned}P_k&=\mu_t\frac{\partial u_i}{\partial x_j}\left(\frac{\partial u_i}{\partial x_j}+\frac{\partial u_j}{\partial x_i}\right)-\frac{2}{3}\rho k\delta_{ij}\frac{\partial u_i}{\partial x_j}\\ P_\omega&=\rho\frac{\partial u_i}{\partial x_j}\left(\frac{\partial u_i}{\partial x_j}+\frac{\partial u_j}{\partial x_i}\right)-\frac{2}{3}\rho\omega\delta_{ij}\frac{\partial u_i}{\partial x_j}\end{aligned} \tag{2.9}$$

and multiply the original $k-\omega$ model with a blending function F_1 and the transformed $k-\epsilon$ model with $(1-F_1)$ and then putting them together one ends up with the following SST model:

$$\begin{aligned}\frac{\partial \rho k}{\partial t}+\frac{\partial \rho u_j k}{\partial x_j}&=P_k-\beta^*\rho\omega k+\frac{\partial}{\partial x_j}\left[(\mu+\sigma_{k}\mu_t)\frac{\partial k}{\partial x_j}\right]\\ \frac{\partial \rho \omega}{\partial t}+\frac{\partial \rho u_j \omega}{\partial x_j}&=\gamma P_\omega-\beta\rho\omega^2+2\rho(1-F_1)\sigma_{\omega 2}\frac{1}{\omega}\frac{\partial k}{\partial x_j}\frac{\partial \omega}{\partial x_j}+\frac{\partial}{\partial x_j}\left[(\mu+\sigma_{\omega}\mu_t)\frac{\partial \omega}{\partial x_j}\right]\end{aligned} \tag{2.10}$$

The blending function F_1 should work in a way to preserve the features of the $k-\omega$ model in a large part of the boundary layer by being equal to one from the wall and up to the edge of the boundary layer where it switches to zero to obtain the $k-\epsilon$ model. The function is defined as,

$$F_1 = tanh(arg_1^4) \tag{2.11}$$

where

$$arg_1 = max(min(\frac{\sqrt{k}}{0.09\omega y}; 0.45\frac{\omega}{\Omega}); \frac{400\nu}{y^2\omega}) \tag{2.12}$$

The eddy-viscosity ν_t is now defined as,

$$\nu_t = \frac{a_1 k}{max(a_1\omega; \Omega F_2)} \tag{2.13}$$

and F_2 is defined as

$$F_2 = tanh(arg_2^2) \tag{2.14}$$

where

$$arg_2 = max(2\frac{\sqrt{k}}{0.09\omega y}; \frac{400\nu}{y^2\omega}) \tag{2.15}$$

The constants used in the SST $k-\omega$ model are:

$$\begin{gathered} \sigma_{k1} = 0.85, \sigma_{\omega 1} = 0.65, \beta_1 = 0.075, \gamma_1 = \beta_1/\beta^* - \sigma_{\omega 1}\kappa^2/\sqrt{\beta^* 0} \\ \sigma_{k2} = 1.0, \sigma_{\omega 2} = 0.856, \beta_2 = 0.0828, \gamma_2 = \beta_2/\beta^* - \sigma_{\omega 2}\kappa^2/\sqrt{\beta^* 0} \\ \beta^* = 0.09, \kappa = 0.41 \end{gathered} \tag{2.16}$$

By using the SST $k-\omega$ model one mitigates two of the weaknesses of the $k-\epsilon$ model which is that in adverse pressure gradient flows it will over-predict the shear stress which the SST model mitigates by a limitation of the shear stress. The other weakness is that it requires a near-wall modification but the $k-\omega$ model does not need that which is why the SST model switches to $k-\omega$ inside the boundary layer. The SST model also mitigates the disadvantage of the standard $k-\omega$ model which is that it is dependent on the free-stream value of ω which the $k-\epsilon$ model is not and is therefore used in the free-stream[11].

2.3 Compressible flow

Compressible flow is defined as a flow with varying density (ρ), in contrast to an incompressible flow where the density is assumed to be constant [13]. Compressibility is defined as the fractional change in volume of the fluid element per unit change in pressure and is defined as,

$$\tau = -\frac{1}{\upsilon}\frac{d\upsilon}{dp}, \tag{2.17}$$

where υ is the specific volume and is equal to the inverse of density ρ. Rewriting the compressibility in terms of density results in the equation

$$\tau = \frac{1}{\rho}\frac{d\rho}{dp}. \tag{2.18}$$

Compressibility therefore says that a change in density will occur when a fluid experiences a change in pressure of which the magnitude is dependent on the properties of the fluid [13]. From the momentum equation for a one-dimensional flow one can derive the speed of sound which becomes,

$$a^2 = \left(\frac{\partial p}{\partial \rho}\right)_s . \tag{2.19}$$

For a perfect gas, using the perfect gas law $\frac{p}{\rho} = RT$, the speed of sound becomes

$$a = \sqrt{\gamma RT}. \tag{2.20}$$

Consider a fluid element with a velocity, temperature and pressure. If this fluid element would stagnate, in other words, if it would have been brought to rest with zero velocity isentropically, the resulting temperature and pressure would have been defined as the total temperature and total pressure (T_0 and P_0). For supersonic adiabatic flows, one could use the energy equation to derive T_0 and P_0 as functions of their static temperature, pressure, Mach number and ratio of specific heats (γ) [13]. The equations are the following.

$$\begin{aligned} \frac{T_0}{T} &= 1 + \frac{\gamma - 1}{2} M^2 \\ \frac{P_0}{P} &= \left(1 + \frac{\gamma - 1}{2} M^2\right)^{\left(\frac{\gamma}{\gamma - 1}\right)} \end{aligned} \tag{2.21}$$

2.3.1 Shockwaves

Lets consider a body immersed in a fluid where the flow is moving toward the body. Information about the presence of the body will be propagated through the fluid through pressure waves, also known as sound waves. For a subsonic flow the sound waves will propagate faster than the flow and therefore be able to propagate upstream and inform the flow about the presence of body and pressure gradients will build up. The flow will then adjust by changing properties such as direction. For a supersonic flow the sound waves travel slower than the flow and can no longer propagate upstream resulting in the loss of information to the flow about the presence of the downstream body. Multiple sound waves will then coalesce a short distance ahead of the body and form a shock wave. Upstream of the shock wave the flow is supersonic and has no information of the presence of the body while after the shock wave the flow is subsonic and will therefore know about its presence and the velocities and properties will then be able to adjust for it. For a flat-faced body the flow will react by creating a normal shock, in other words the shockwave is perpendicular to the flow. The normal shock is assumed to be a discontinuity where the flow properties abruptly change. Across the shock the static pressure, temperature and density will increase while velocity will decrease [13].

If instead the flow meets a surface with an angle θ deflected upward the flow will have to "turn into itself" and an oblique shock will occur, deflecting the flow with the same angle θ. In contrast if the flow meets a surface which is deflected downwards the flow will have to be "turned away from itself" and through an expansion fan. For an oblique shock a similar phenomena to a normal shock will occur where it's seen as a discontinuity where the properties suddenly change. While for an expansion fan the properties changes smoothly and continuously with the exception for the very tip of the wall edge where the wall streamline where the changes will occur discontinuously. As opposed to a normal shock and oblique shock, across an expansion wave the Mach number will increase while the pressure, temperature and density will decrease [13].

2.3.2 Supersonic and hypersonic flows

As from oblique shock theory one can show that for a given flow deflection angle, the density increase across the shock wave will become larger for an increased Mach number. Which means that the mass flow behind the shock can "squeeze through" smaller areas more easily as the density is higher. That means that for a flow over a hypersonic body the shock wave will lie closer to the body compared to a supersonic flow as the for a given mass the area can be smaller as the density is now higher. [13].

Consider a hypersonic flow over a flat plate. For a hypersonic flow which contains a large kinetic energy, when the flow within the boundary layer is slowed down by viscous effects the kinetic energy will in part be transformed into internal energy. This will increase the temperature inside the boundary layer. When the temperature increases it will in turn increase the viscosity coefficient which will make the boundary layer thicker. In addition to that because the pressure is constant in the normal direction in the boundary layer when the temperature increases it will lead to a decrease in density because of the equation of state $\rho = p/RT$. As mass flow needs to be conserved inside the boundary layer a decrease in density means that the boundary layer thickness must increase. These two phenomena will make the boundary layer grow more rapidly compared to slower speeds [13].

2.3.3 Boundary layer and heat transfer

When a temperature difference between a wall and a fluid exists heat transfer will occur by conduction and when conduction is accelerated by the motion of the fluid it's called convection. In a lot of cases when there is heat transfer between a wall and a fluid there will be a smooth variation in temperature in the thermal boundary layer. For a given heat flux, it will be proportional to the temperature difference between the wall temperature and the freestream temperature defined as,

$$q = h(T_w - T_\infty). \tag{2.22}$$

The adiabatic wall temperature is defined as the temperature attained at the surface of an adiabatic wall. For high speed flows the adiabatic wall temperature(T_{aw}) will not be the stagnation temperature of the fluid as would be expected as the fluid will be brought to rest. This is because the temperature rise due to stagnation will be large enough that the viscous effects slowing it down won't be adiabatic. This will result to a significant heat transfer from the high temperature region near the wall and lower temperature further away from the wall. Therefore the stagnation temperature near the wall will be lower than that in the free stream. But to satisfy the steady-state energy equation, there must be a region between the wall and the freestream where the stagnation temperature is larger than the free stream [14]. The convective heat transfer experienced at a wall is defined as

$$q_c = h(T_{aw} - T_w), \tag{2.23}$$

where h is the heat transfer coefficient and T_{aw} is the adiabatic wall temperature (the resulting wall temperature if there is no heat transfer). T_w is the wall temperature attained for the given flow.

The Nusselt number is a non-dimensional number which is defined as ratio between the total heat transfer and conductive heat transfer and is defined as

$$Nu_L = \frac{hL}{k} \tag{2.24}$$

where h is the convective heat transfer, L is a characteristic length and k is the thermal conductivity of the fluid.

2.4 Plume-air interaction

During the ascent the rocket engines exhaust is pointed in the same direction of travel. The exhaust will then accelerate through the nozzle to supersonic speeds and will, after ejection, expand to match the ambient pressure of the atmosphere. In descent during a retro-propulsion maneuver, the supersonic exhaust will meet supersonic or hypersonic flow from the atmosphere creating strong shock waves and stagnating the flow. The behavior of the flow will depend on a multitude of variables, such as nozzle exit conditions, atmospheric conditions and Mach number [2].

As mentioned, during the ascent the plume structure is dependent on the ambient pressure as it generally expands to match the ambient pressure, this is however not necessarily true for retro-propulsion. It is well known that information cannot travel upstream in supersonic flows and neither over a shockwave. This means that the exhaust ejected from the nozzle does not know the freestream pressure and therefore will not expand in order to match it. The exhaust will instead expand in order to match the dead air pressure (p_d) which is the pressure next to the nozzle, outside the plume and behind the shock waves, it's location can be seen in figure 2.1a. The dead air pressure correlates to but is usually not equal to the ambient pressure. The dead air pressure is also not possible to calculate analytically making the plume size and structure hard to predict [2, 15].

Studies have shown that there are two plume types in retro-propulsion, blunt plume (also known as short penetration mode) and penetrating plume (also known as long penetrating mode), and can be seen in figures 2.1a and 2.1b respectively [2, 16]. A blunt plume is characterized by a highly underexpanded plume, caused by the low ambient pressures at high altitudes and large opposing free stream Mach numbers. The penetrating plume is characterized by an overexpanded plume that usually has a series of reflected shocks following an incident shock. As the penetrating plume penetrates the bow shock it reduces its strength, compared to the bow shock for a blunt plume [2]. It is generally understood that the change from one plume structure to another happens sharply, but the reason and timing of the change remains undetermined, and researchers have yet to reach a consensus on the underlying mechanisms [10]. Some researchers claim that transition from a blunt plume to penetrating happens when the thrust coefficient $C_T \approx 1$ where a higher C_T results in a blunt plume and lower than one results in a penetrating plume [15]. Thrust coefficient, a dimensionless number defined according to eq. 2.25, where T is thrust, p_∞ is freestream dynamic pressure, A_m is model base area, M_∞ is free stream Mach number, p_e is nozzle exit pressure, A_e is nozzle exit area, A is reference area and in this case the cross-sectional area of the rocket, γ_j and γ_∞ are heat capacity ratio in the jet and free stream respectively, is a parameter that has been shown to have a correlation with the shape of the plume [15, 17]. When the freestream velocities decrease (lower supersonic velocities) the point of transition is increased and when the velocities increase, the transition C_T is decreased. The plume behavior in subsonic velocities can generally be considered as a penetrating plume and are highly unsteady regardless of C_T [15]. Other studies have shown that the transition point is not dependent on C_T, but rather is dependent on the nozzle exit pressure ratio ($EPR = \frac{p_e}{p_\infty}$) and transitions sharply at a certain EPR while others say that it happens as the exhaust transitions from underexpanded to overexpanded [17, 10].

$$C_t = \frac{T}{p_\infty A_m} = \frac{1}{M_\infty^2} \frac{p_e}{p_\infty} \frac{2A_e(1+\gamma_j M_e^2)}{\gamma_\infty A} \tag{2.25}$$

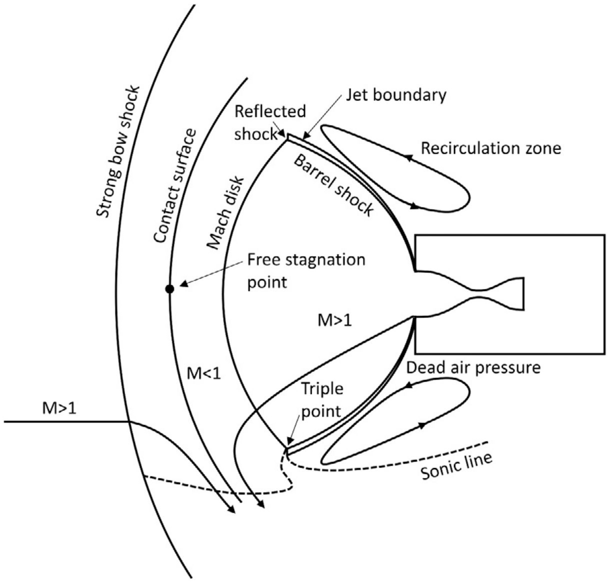

(a) Blunt Plume [2].

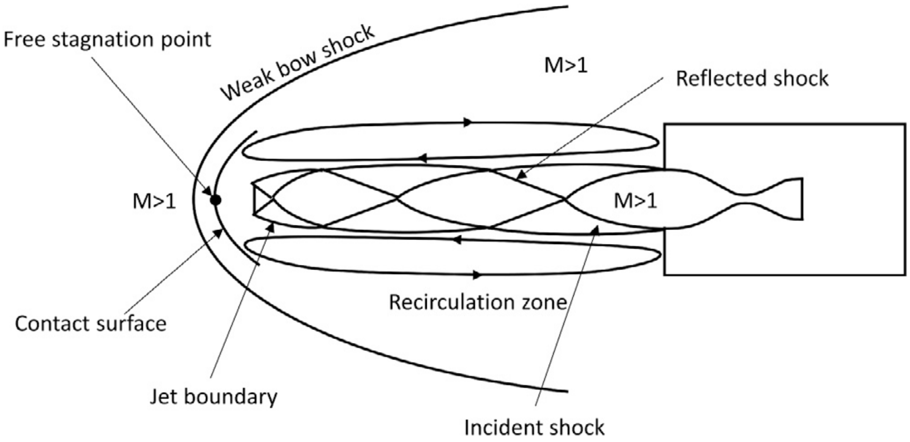

(b) Penetrating Plume [2].

Figure 2.1: Comparison of Blunt and Penetrating Plumes.

The blunt plume, more common at higher altitudes where the exit pressure ratio is larger, is characterized by a bow shock (from the freestream), contact surface (between freestream and exhaust) and a Mach disk (from highly underexpanded exhaust). After the flow passes the shockwave, they turn along the contact surface bending towards the sides of the rocket, accelerate to supersonic speeds and once more reattach to the surface of the rocket [17]. In the recirculation zone, next to the nozzle in an area with subsonic flow, a large shear layer is created which plays a major role in plume structure [17]. The contact surface is the surface that separates the freestream gases and the exhaust gases, and mixing may occur over the contact surface if properties, such as velocities and pressures, differs. Mixing may also occur in the recirculation zone between the plume and the dead air zone as well as in the jet boundary [15].

2.5 Plume-plume interaction

Modern day vertical take off vertical landing rockets generally do not use a single engine but rather a cluster of engines. Often during the different phases of flight, instead of throttling the engines, certain engines are turned on and off where Space-X Falcon 9 rocket, that uses a nine engine cluster, all nine engines are used during ascent, three (in a vertical line) are used during reentry burn and only one (central engine) is used during the landing burn [2]. This means that during the reentry burn the flow will not be characterized by a single plume as discussed in sec 2.4, but rather by multiple plumes interacting not only with the atmosphere, but also with each other.

At lower velocities during the landing phase, where the plumes are less underexpanded or even overexpanded due to the higher ambient pressures, the plumes behave as a penetrating plume and the plume-plume interaction happens far downstream from the nozzle. At higher altitude, where the plumes behaves as blunt plumes, with large expansions the interactions are closer to the nozzle exit and it becomes more complex as can be seen in figure 2.2 [2]. As the flow of the jets meet, oblique shocks will form and propagate through the flow [18]. There will also be a stagnation point between the nozzles near the exit creating reverse flow where hot gases are deflected back toward the walls of the nozzle and the base plate of the rocket, an effect that is insensitive to the freestream Mach number [2, 16]. It has also been shown that the plume structure is highly unsteady where experiments show the plume rapidly switching between blunt plume and penetrating plume while steady state CFD often predict it to penetrating plume [2].

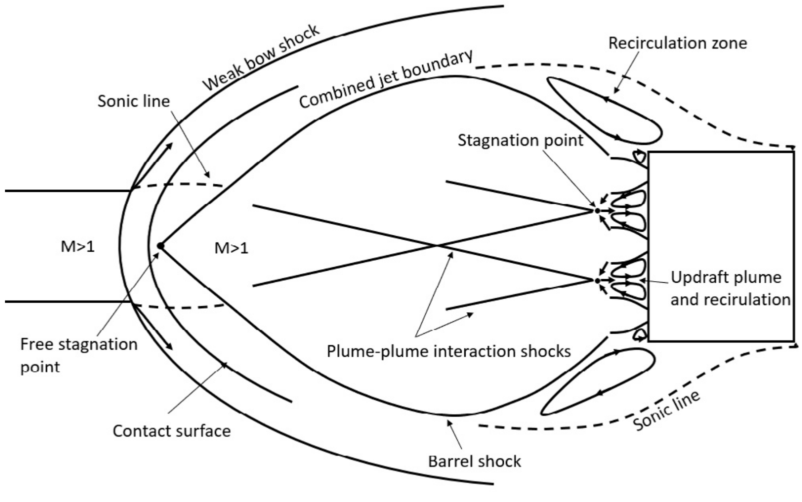

Figure 2.2: Plume-plume interaction at supersonic velocities [2].

2.6 Properties of high-temperature gas

In most fluid flow one assumes that the fluid adheres to the ideal gas law, in other words that pressure and temperature relate through eq. 2.26, where R is the specific gas constant. The assumption of ideal gas is that the molecules in space are small and distance between them are large, and therefore the intermolecular forces, which effect gas properties, are negligible [13]. When temperature decreases and pressure increase the molecules gets pact closer together decreasing the accuracy of this assumption. However, in this case where there is high temperature from the exhaust and shocks and low atmospheric pressures found at high altitude the ideal gas law, in other words eq. 2.26, still holds [13]. Worth to note is that chemical reactions can occur in gases with very high temperatures which will change the properties of $R = \Re/M$, where $\Re$ is the universal gas constant and M is molecular weight which is not constant during chemical reactions [13], however more on this in section 2.8.

$$p = \rho RT \tag{2.26}$$

Before delving deeper into the concept of gas-laws some talk about chemistry and quantum physics is needed to be able to understand what effects the properties of gases. To begin with, assume that only one species is regarded, in other words a homogeneous gas containing only one type of molecule or element.

For a single species, there are different modes of energy, different states that an element or molecule can have that all contain a certain amount of energy. An element consisting of a single atom have two modes of energy, translational energy and electronic energy while a molecule consisting of two or more molecules has 4 energy modes, translational energy (ϵ_t), rotational energy (ϵ_r), vibrational energy (ϵ_v) and electronic energy (ϵ_e) [13].

- **Translational energy (ϵ_t)** is the movement of a species through space, in other words the displacement of center of mass. The movement of center of mass can occur in three direction (x, y, z) and therefore has three thermal degrees of freedom [13].

- **Rotational energy (ϵ_r)** is the rotation of atoms around its own axis. The rotation can also occur in three dimension (x, y, z) resulting in three thermal degrees of freedom. For linear polyatomic molecules, such as bi atomic molecules or CO_2, where all nuclei are aligned in a strait line, the rotational energy in the axis of the molecules is minimal compared to the other directions of rotation. For these types of molecules generally only two thermal degrees of freedoms are considered while for nonlinear polyatomic molecules, such as H_2O, all three needs to be considered [13].

- **Vibrational energy (ϵ_r)** is the movement of atoms with respect to other atoms within the same molecule. This mode, governed by intramolecular forces, can be seen as atoms with relative velocity connected by a spring. Vibrational energy is therefore the sum of kinetic energy (the translation of the atom) and the potential energy (the energy stored in the relative position of the atoms with regard of the neutral position, consider as potential energy stored in the spring). This means that vibrational energy has two thermal degrees of freedom [13].

- **Electronic energy** (ϵ_e) comes from the electrons circulating the atom or molecule and can, as vibrational energy, also be split into two. The two energies are kinetic, the movement of electrons relative to the atom, and potential energy due to the electrons position in the electromagnetic fields. Electronic energy therefore has two thermal degrees of freedom [13].

The total energy for an element can be written as

$$\epsilon = \epsilon_t + \epsilon_e \tag{2.27}$$

while the total energy for a molecule can be written as

$$\epsilon = \epsilon_t + \epsilon_r + \epsilon_v + \epsilon_e. \tag{2.28}$$

Due to quantum mechanics these energy levels can only exist at certain discrete values, and it is these values that the different energy modes are at that effect the gases thermodynamic properties. Translational and rotational modes have, specially in lower values, their discrete levels so close together that they can almost be considered a continuum [13]. The second level for vibrational energy, in other words the first level after lowest allowable energy level found at zero Kelvin, occurs at quite high energy levels where each successive level is closer together than the previous while the second electronic energy mode is found even higher than that [13]. Many different combinations of discrete levels of energy can combine up to the same total energy, in other words the same total energy for a single atom is $\epsilon = \epsilon_t + \epsilon_e$ and the resulting total energy would be the same if $\epsilon_t = 1$ and $\epsilon_e = 2$ as well as $\epsilon_t = 2$ and $\epsilon_e = 1$. The combination of energy level is determined by statistical probability on a micro scale. This can then be used to calculate the most probable macro scale state [13].

The background and derivation of the equation of energy, found in quantum mechanics, is too heavy and not necessary to recite for the purpose of this thesis. However *theorem of equipartition of energy* state that each thermal degree of freedom contributes by $\frac{1}{2}RT$ to the energy level of the molecule with the exception of ϵ_e and ϵ_v [13]. This means that $\epsilon_t = 3(\frac{1}{2}RT) = \frac{3}{2}RT$, $\epsilon_r = 2(\frac{1}{2}RT) = RT$ (for linear polyatomic molecules) while $\epsilon_v = \frac{hv/kT}{e^{hv/kT}-1}$ and ϵ_e is obtained from spectroscopic measurements. The resulting total energy of a molecule then becomes:

$$\epsilon = \underbrace{\frac{3}{2}RT}_{Translational} + \underbrace{RT}_{Rotational} + \underbrace{\frac{hv/kT}{e^{hv/kT}-1}RT}_{Vibrational} + \underbrace{\epsilon_e}_{Electronic} \tag{2.29}$$

where R is the specific gas constant, T is the temperature, h is Planck's constant, v is the vibrational frequency and k is the Boltzmann's constant. One can then divide by T to get

$$c_v = \frac{3}{2}R + R + \frac{hv/kT}{e^{hv/kT} - 1}R + \frac{\partial \epsilon_e}{\partial T} \tag{2.30}$$

As eq. 2.30 shows, c_v is only a function of T and that different modes has different effect on internal energy. It should be emphasized that these terms take discrete values and therefore are constant up until a certain point and that statistical probabilities dictates the distribution of energy over the different modes. It is once a energy mode gets excited, in other words reach a higher energy level, that the thermodynamical properties change and this generally happens at different temperatures. These levels then create different regions of gas-laws that can be approximated in CFD [13]. Note that specific heat at constant pressure, $c_p = R - c_v$, as well as the ratio of specific heat, $\gamma = \frac{c_p}{c_v}$, is generally what is used in discussions of thermodynamical properties in fluid mechanics and is what will generally be talked about going forward. The temperature ranges of the regions vary with species and pressures, where lower pressures generally decrease the temperature, but for air at sea level the following behaviour is:

- **0 to 1 K:** Only translational energy is excited and all other energy modes are either zero or at their lowest energy level possible. In this region thermodynamical properties, such as γ, are constant [13].

- **1 to 3 K:** Rotational energy starts to get excited at 1 K and reaches fully excited at 3 K. During this range, as more and more molecules get their rotational energy exited, γ becomes non-constant [13].

- **up to 800 K:** The upper limit is not a strict limit and is a graduate transition, and therefore varies between sources but is generally said to be around 500 - 800 K. During this range translational and rotational energy is fully excited resulting in constant value for c_p [13, 19]. This range is what is considered *calorically perfect gas* and is a common assumption in many CFD simulations. Since c_p is constant enthalpy, $h = c_p T$, becomes a linear function of temperature.

- **800 to 2000 K:** After approximately 800 K, vibrational energy starts to get excited, again creating a region of non-constant γ. In this region c_p vary, and generally increase, with temperature creating non-linear relationship between temperature and enthalpy. If there is no chemical reaction and one disregards intermolecular forces, which is assumed in ideal gas, this region can also be considered *thermally perfect gas*, in other words that all thermodynamical properties vary only with temperature [13]. In other words, $c_v = c_v(T)$, $c_p = c_p(T)$, $\gamma = \gamma(T)$ and $R =$ constant [19].

- **2000 to 9000 K:** In this region translational, rotational and vibrational energy modes are all excited. When $T \to \infty$ the theoretical limit of c_p should converge towards a determined value, however, this is generally not the case as chemical reactions starts to occur the temperature won't reach that value. Specifically as dissociation occurs which is when molecules break down to into their individual atoms. But also during exchange, when molecules exchange atoms. Between 2000 and 4000 K O_2 dissociates through the reaction $O_2 \Leftrightarrow 2O$ and between 4000 and 9000 K N_2 dissociates through $N_2 \Leftrightarrow 2N$. Between 2000 and 9000 K exchange between $N_2 + O \Leftrightarrow NO + N$ and $NO + O \Leftrightarrow N + O_2$ occurs [20]. As this happens new species are being created which means that not only does the properties of the old species at that current temperature change, but also the properties of the new species. Another thing that needs to be considered is mixing and concentration of each species in each cell.

- **$>$ 9000 K:** After 9000 K ionization starts to occur where electrons break free from species. Among other reactions, oxygen become oxygen ions through $O \Leftrightarrow O^{+}+e^{-}$ and nitrogen react to become nitrogen ions through $N \Leftrightarrow N^{+}+e^{-}$ [20]. Similar to the chemical reactions found in 2000 - 9000 K region, γ will be a function of the local species, with the difference that more types of reactions and species needs to be considered. Another phenomena that can occur is catalytic walls. When the flow hits a shockwave, the temperature rapidly increase and chemical reactions occur. These particles can then react once more as they near the wall, which is generally lower temperature than the flow or due to reaction with the material of the wall itself [20, 19].

2.7 Properties of high altitude atmosphere

During reentry the spacecraft flies through the atmosphere down to earth. During this flight it experiences many different layers in the atmosphere where there is slightly different chemical composition, temperatures and most significantly the change in pressure and density going from vacuum to 1 atm. The different properties of the gas at these different altitudes will, just as mentioned earlier with temperature, also play a part in the behavior of the flow and how it is modeled. The regions, that can be seen in figure 2.3, are divided into transition regime, continuum regime, thermochemical equilibrium flow and the non-equilibrium flows which includes chemical non-equilibrium and thermochemical non-equilibrium flow that both depend on flight velocity and altitude [20].

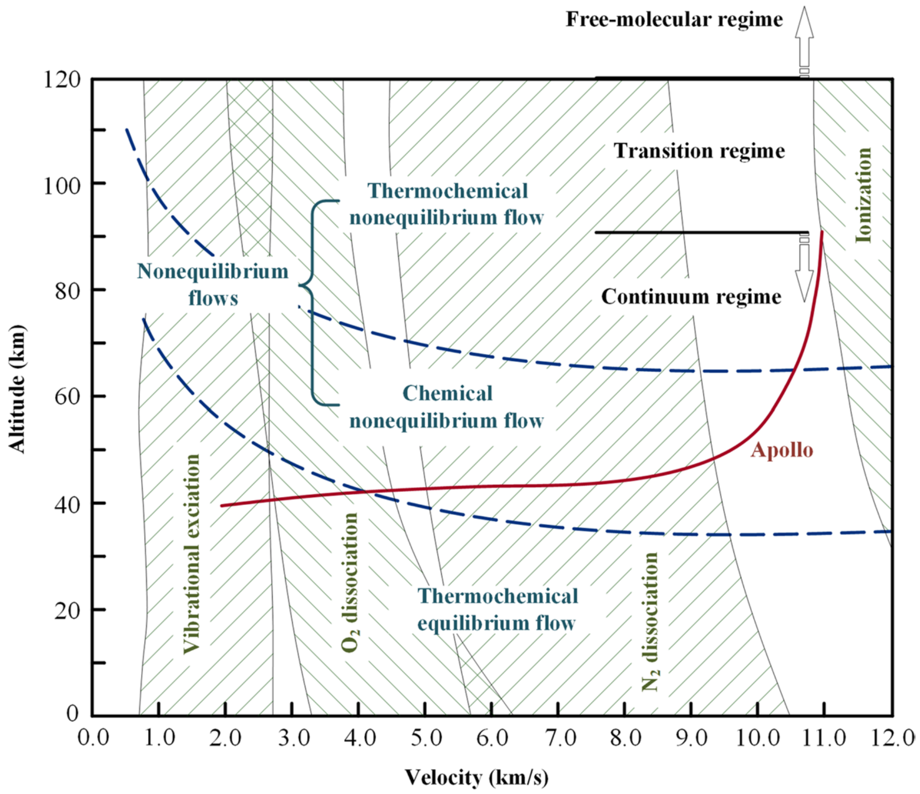

Figure 2.3: Gas models at different speeds and altitudes [20]

An important factor when looking at high altitudes is the Knudsen number (Kn) defined as:

$$Kn = \frac{\lambda}{L} \tag{2.31}$$

where λ is the local mean free path and L is the characteristic flow length. At higher altitudes the mean free paths of the particles increase making the Knudsen number increase. The Knudsen number can then be used to split the atmosphere into different regimes as follows [20]:

- **Continuum regime,** $Kn < 0.001$**:** In static cases it is generally found at altitudes <90 km. In the continuum regime the flow can be considered continuous .[20].
- **Slip flow regime,** $0.001 < Kn < 0.1$**:** Local non-equilibrium is important near surfaces, and boundaries has a slight tangential component [20].
- **Transitional regime,** $0.1 < Kn < 10$**:** For static cases it is generally found at altitudes $90 < h < 120$ km. Distance between molecules large enough to make collisions rare making flow deviate from equilibrium [20].
- **Free-molecular regime** $Kn > 10$**:** Intermolecular collisions neglected and

gas only interacts with walls [20].

2.7.1 Thermochemical equilibrium flow

Thermochemical equilibrium flow means that the fluid is in both chemical equilibrium and thermal equilibrium and is found at lower altitudes and velocities. Chemical equilibrium (explained in more detail in section 2.8.2) is when reactions occurs at the same rate in both directions, in other words that a species is being produced and destroyed at the same rate. Thermodynamical equilibrium is when all of the energy states $\epsilon = \epsilon_t + \epsilon_r + \epsilon_v + \epsilon_e$ (explained in more detail in section 2.6) are in equilibrium in their most probable macro state [20]. In other words that no individual energy state is abnormally excited above any other (note that for both thermochemical equilibrium and non-equilibrium $\epsilon_t \neq \epsilon_r \neq \epsilon_v \neq \epsilon_e$) [13]. In this region the internal energies can be expressed by a single temperature and the chemical reactions have been fully carried out and only depend on temperature and pressure. This means that the chemistry can be uncoupled from the flow equations and can be solved by the conventional Navier-Stokes equations [20].

2.7.2 Thermochemical non-equilibrium

Thermochemical non-equilibrium is when the flow is in thermodynamical and chemical non-equilibrium. Only a brief description of chemical non-equilibrium will be given here, a more detailed description is given later in sections 2.8.2 and 2.8.3. Assume we have the species A and B reacting to make the species AB. The triggering of the reaction is often made by a collision of an arbitrary third party species X resulting in the reaction $A + B + X \Leftrightarrow AB + X$ [13]. In chemical equilibrium the reactions is equal in speeds for both directions, in other words, there is equal amounts of A, B and AB being produced. At high altitudes, where the pressure and density is low and distance between molecules are greater, the probability of collision is much lower resulting in a longer time before sufficient collisions have occurred to equilibrate the reactions [19, 13]. As figure 2.3 show, this is prominent from approximately 40 km altitude at high velocities, or up to 80 km at lower velocities [20]

Thermodynamical equilibrium, just as as chemical equilibrium, is often achieved when atoms collide, triggering energy exchange, both between molecules and between states within the same molecule [13]. One example of this occurring is after a shockwave the translational energy is suddenly increased, however the other energy states has not been able to equilibrate due to lack of collisions creating a relaxation region where they try to "catch up" the translational mode [19]. As earlier mentioned in section 2.6, the thermodynamical properties of the fluid is determined by the energy states which is why it is important to calculate the excitation of the different states.

When there is thermochemical equilibrium, one can relate the energy level by using a 1-temperature model, in other words, if the temperature is known, the total energy of the different states of the molecule can be deduced through most probable macro state [20]. However, when thermodynamical non-equilibrium is present, the different energy modes needs to be represented by an individual temperature, compensated by in 2- or 3-temperature model. In the 2-temperature model translational-rotational temperature (T_{tr}) represents the translational and rotational energy states, and vibrational-electron-electronic temperature (T_{ve}) represent the vibrational and electronic energy states. Translational and rotational energy states are assumed to be close to equilibrium at all times, which is why 3-temperature model splits vibrational-electronic temperature into vibrational temperature (T_v) and electronic temperature (T_{ele}). The result is in other words: 1-temperature model $\Rightarrow T = T$, 2-temperature model $\Rightarrow T = T_{tr} + T_{ve}$ and 3-temperature model $\Rightarrow T = T_{tr} + T_v + T_{ele}$ [20]. Each temperature in the different temperature models have their own transport- and production equations added to the traditional Navier-Stokes equations [20].

2.7.3 Continuum and transition regime

At very high altitudes, above 90 km the atmospheric pressure and density is near vacuum resulting in continuum, a fundamental assumption needed for the traditional Navier-Stokes equations, can no longer be assumed [2, 20]. The assumption of continuum is that there are sufficient number of fluid particles in all CFD cells to say that the macroscopic properties (such as density, speed and temperature) are given by the average of all particles within the cell [19]. As the density and pressure decrease, distance between molecules increase and the number of molecules in each cell becomes less, the macroscopic properties are no longer determined by the average properties. The Navier-Stokes equations are valid in the continuum regime where $Kn < 0.001$ [20], and can work up to $Kn < 0.03$ [19]. One of the first fundamental assumptions to fail is the no-slip condition, in other words that velocities at walls and stationary boundaries are no longer zero and that fluid temperature is not equal to the wall temperature [19]. Assuming a no-slip condition as well as using thermochemical non-equilibrium models one can extend the use of the Navier-Stokes equations and CFD up to about $Kn = 0.1$ with good results while the continuum model has to be replaced with molecular model for $Kn > 0.2$ where conventional CFD is no longer applicable [19, 20]. At larger Knudsen numbers another method, such as Boltzmann equation, a more computationally expensive method, needs to be used that takes particle collisions into considerations [20].

2.8 Chemistry models

As explained above, one needs to have different chemical models to be able to simulate gases with high temperatures or when the gas composes of multiple species. This is necessary, not only to capture any potential chemical reactions, but also to model the change of c_p as you get outside the *constant γ region*. The different chemical models have different features, capturing different parts of the chemistry and physics, with different levels of fidelity and proximity to the real world. An important aspect when it comes to chemistry models is that it heavily affects the runtime of the simulations, this means that a balance needs to be made between computational cost and accuracy of the model [2]. The balance includes both how to treat reactions, but also the transport of species and what species to regard.

An important dimensionless parameter used in chemical simulations is the Damköhler (Da) number wich represents how chemical reactions behave with respect to the flow [2]. Damköhler is defined according to eq. 2.32 where τ_f is the flow timescale and τ_c is the chemical timescale, and defines what chemical models are appropriate. A large Damköhler number imply fast chemical reactions with the respect to the flow, while a small number imply slow reactions. Another definition of Damköhler number is comparing chemical reaction rates to turbulence, where a large Damköhler would imply good mixing between species and the system behaves as a perfectly stirred reactor while a small Damköhler would imply that reactions highly depend on local concentrations of species [21]. The chemical timescales in high temperatures and pressures found in regular combustion are generally low, however, secondary effects, such as post combustion in exhaust, plume-air interaction reactions and NO_x formations when the temperatures and pressures are lower, are significantly larger and can exceed the flow timescales by orders of several magnitudes [2]. This results in different chemistry models having different accuracies in different regions of the combustion and reaction process [2].

$$Da = \frac{\tau_f}{\tau_c} \tag{2.32}$$

Computational fluid dynamics treats species in the flow as any other property that has a tranport equation. The equation is given by

$$\frac{\partial}{\partial t}(\rho Y_k) + \frac{\partial}{\partial x_i}(\rho u_i Y_k) = \frac{\partial}{\partial x_i}(\rho D_k \frac{\partial Y_k}{\partial x_i}) + \dot{\omega}_k \tag{2.33}$$

where Y_k denotes the species k, D_k is the species diffusion coefficient and $\dot{\omega}_k$ is the source term that stems from chemical reactions [22]. Equation 2.33 is the same for all chemistry models where species is considered with the difference being how the source term $\dot{\omega}_k$ is modeled.

As the species are being transported through the flow the thermodynamics properties, such as γ and R, and transport properties, such as viscosity and conductivity, needs to be evaluated. The most common ways of evaluating these are table-lookup and curve fitting [20]. As table-lookup is cumbersome in CFD applications, curve-fitting, fitted from the values in the tables, is often preferred as they are easy and effective to incorporate into numerical schemes [20]. Ansys fluent allows for curve-fitting through CHEMKIN format, a common format to calculate and evaluate properties as a function of temperature, more on this in section 3.6.1.

2.8.1 Frozen chemistry

A common assumption when modeling chemistry is assuming frozen chemistry or frozen reaction. Frozen chemistry is when only the transport of species is considered and no reactions occur, in other words when $\dot{\omega}_k$ is assumed 0. This is a good approximation when the Damköhler number is very low, in other words when the chemical reactions occur slowly with respect to the flow [2, 19]. Since there is no reactions in frozen chemistry the gas constant, $R = \frac{\Re}{M}$, is constant while thermodynamical properties (γ and c_p) are a function of temperature, meaning that frozen chemistry is an assumption of thermally perfect gas [19]. This means that the properties is only dependent on *one* property, temperature, making frozen chemistry the simplest and computational cheapest option of chemistry model [19].

Since frozen chemistry only models transport of species it is a good assumption as long as no reactions are significant in the flow. Figure 2.4 highlight the difference between frozen chemistry model and chemical equilibrium model for air at one atmosphere [19]. It shows that for lower temperatures ($< 2000\,\mathrm{K}$), frozen chemistry and chemical equilibrium will give similar values of c_p while at higher temperatures they differ drastically.

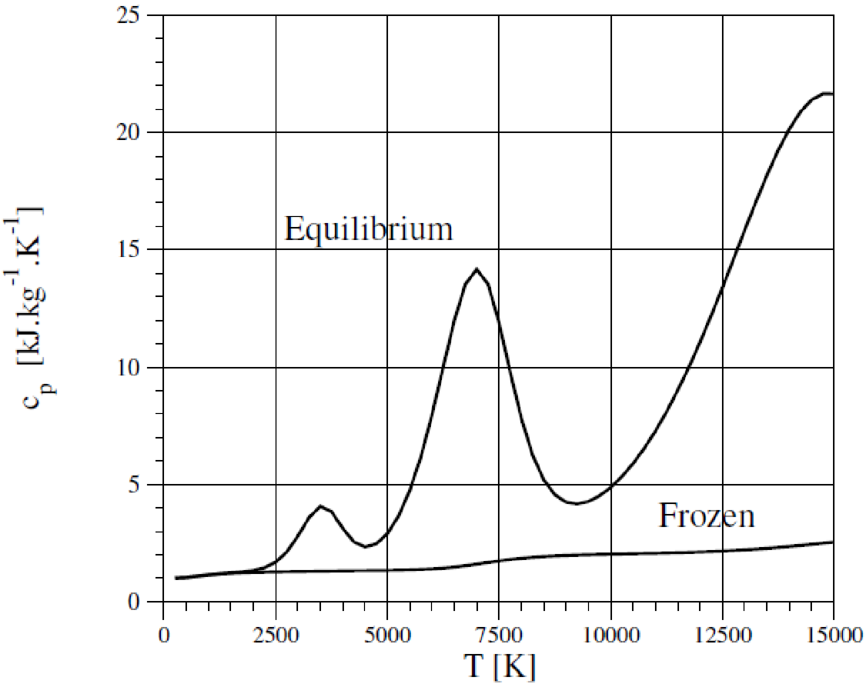

Figure 2.4: c_p of air at one 1 atm [19]

2.8.2 Chemical equilibrium

Reacting chemistry is when the chemistry model allows the different species to react with each other. This includes dissociation, exchange and ionization. Chemical reactions just as most other physical effects, is not instantaneous, it takes time for chemical reactions to occur and stabilize. This is a very difficult and computationally heavy [2] to simulate and there a couple different ways to model this where they generally fit into one of the two groups: *chemical equilibrium* and *chemical non-equilibrium*.

In general, reactions will not only occur one way, but will go back and forth. Assume that we have two species A and B and they react through equation 2.34 to create AB. The reaction will occur in both directions, in other words A and B will react to produce AB while AB will also dissociate and produce A and B [13]. These two reactions occur in different rates, however as the concentrations change, both reactions will converge towards reacting in equal speeds meaning that equal amounts of A, B and AB is being produced. This will occur if the reactions are left undisturbed for long enough time. When the reaction at a position and instance react in both directions at the same speed it is considered *chemical equilibrium* [13].

$$A + B \Leftrightarrow AB \tag{2.34}$$

Statistical thermodynamics [13] show:

$$N_j^A = N^A \frac{g_j^A e^{-\epsilon_j^A/kT}}{Q^A} \tag{2.35}$$

$$N_j^B = N^B \frac{g_j^B e^{-\epsilon_j^B/kT}}{Q^B} \tag{2.36}$$

$$N_j^{AB} = N^{AB} \frac{g_j^{AB} e^{-\epsilon_j^{AB}/kT}}{Q^{AB}} \tag{2.37}$$

$$\frac{N^A N^B}{N^{AB}} = e^{-\Delta\epsilon_0/kT} \frac{Q^A Q^B}{Q^{AB}} \tag{2.38}$$

where N_j^i is the number of the i species at the energy level j, g_j is number of generate energy states, ϵ is energy level, ϵ_0 is lowest possible energy level for given specie, and Q is a partition function defined as $Q \equiv \sum_j g_j e^{-\epsilon/kT}$, k is Boltzmann's constant and T is temperature.

The ideal gas law can be rewritten to $pV = NkT$ and can be reused to calculate partial pressures p_i for species i:

$$p_i V = N_i kT \tag{2.39}$$

where p_i is partial pressure, N_i is the number of particles to fill up the volume V. Combining equations 2.38 and 2.39 gives

$$\frac{p_A p_B}{p_{AB}} = \frac{kT}{V} e^{-\Delta\epsilon_0/kT} \frac{Q^A Q^B}{Q^A B} = K_p(T). \tag{2.40}$$

$K_p(T)$ is called the equilibrium constant for the reaction $A + B \Leftrightarrow AB$ and is, for ideal gas, a function of only temperature [19]. Using the general chemical equation:

$$v_1 A_1 + v_2 A_2 + v_3 A_3 \Leftrightarrow v_4 A_4 + v_5 A_5 \tag{2.41}$$

where v_i is the stoichiometric mole number for species i and A_i is the chemical symbol for species i, one define the equilibrium constant as:

$$K_p(T) \equiv \frac{(p_{A_4})^{v_4}(p_{A_5})^{v_5}}{(p_{A_1})^{v_1}(p_{A_2})^{v_2}(p_{A_3})^{v_3}}. \tag{2.42}$$

The equations 2.34-2.42 can be used to show that the composition for the chemical equilibrium is a function of both pressure and temperature [13]. This means that the composition will change over the domain, due to temperature and pressure changes, even though no new species are introduced.

When assuming chemical equilibrium from a computational simulation point of view, this generally means that one assumes that all chemical timescales are very low compared to fluid timescales and reactions occur instantaneously [19, 2]. Chemical equilibrium is, in other words, a good approximation when the Damkhöler number is large [2]. In a steady state simulation the pressure and temperature is constant for a given point. This means that, in that point, K_p is constant and the composition of species is also constant. The result is, just as in frozen chemistry, the source term ($\dot{\omega}_k$) is equal to zero [19]. As mentioned, chemical equilibrium is a function of *two* parameters, temperature and pressure, making it more computational heavy than frozen chemistry.

2.8.3 Chemical non-equilibrium

The second type of reacting chemistry is called chemical non-equilibrium and occur when the reactions back and forth occur at different rates. This model is generally a good assumption if the Damköhler number is ≈ 1, in other words when the flow timescale and chemistry timescale is comparable [2].

Assume that we have a reaction defined as :

$$\sum_{k=1}^{N_s} \nu'_{kr} X_k \Leftrightarrow \sum_{k=1}^{N_s} \nu''_{kr} X_k \tag{2.43}$$

where ν_{kr} is the stoichiometric coefficient of species k of reaction r and X_k is a dummy symbol of species k [19]. A chemical reaction often reacts with regards to a separate species that is not apart of the original reaction. An example is dissociation of oxygen through the reaction $O_2 + X \Leftrightarrow 2O + X$ where X is an arbitrary third party species. In the destruction of O_2 the molecule will collide with the species X and will dissociate into $2O$ where X is neither produced or destroyed, and reversely $2O$ collide with X to produce O_2. In other words X is an important ingredient in the reaction and will effect the rates and properties of the reaction [19]. The production rate for chemical non-equilibrium can be calculated as [19]:

$$\dot{\omega}_{k,r} = M_i \left[\underbrace{(\nu''_{k,r} - \nu'_{kr}) k_{fr} \prod_{j=1}^{N_s} (\frac{\rho_j}{M_j})^{\nu'_{jr}}}_{production} - \underbrace{(\nu''_{k,r} - \nu'_{kr}) k_{br} \prod_{j=1}^{N_s} (\frac{\rho_j}{M_j})^{\nu''_{jr}}}_{destruction} \right]. \tag{2.44}$$

where $\dot{\omega}_{k,r}$ is the production rate for species k through reaction r. M_k is molecular weight, k_{fr} and k_{br} is forward and backward rate coefficient respectively, the product is over all third party species j in the system, N_s is the total number of species and ρ is density. This equation can then be rewritten into a general production rate including all reactions relating to species i by [19]:

$$\dot{\omega}_k = M_k \sum_{r=1}^{N_r} (\nu''_{kr} - \nu'_{kr}) \left[\underbrace{k_{fr} \prod_{j=1}^{N_s} (\frac{\rho_j}{M_j})^{\nu'_{jr}}}_{production} - \underbrace{k_{br} \prod_{j=1}^{N_s} (\frac{\rho_j}{M_j})^{\nu''_{jr}}}_{destruction} \right]. \tag{2.45}$$

where N_r is the total number of reactions related to species k. As one can see, if the production term is equal to the destruction term, in other words if eq. 2.46 is true, the total production rate of species k through reaction r is equal to zero and this is what is considered chemical equilibrium.

$$k_{fr} \prod_{j=1}^{N_s} (\frac{\rho_j}{M_j})^{\nu'_{jr}} = k_{br} \prod_{j=1}^{N_s} (\frac{\rho_j}{M_j})^{\nu''_{jr}} \tag{2.46}$$

The main unknown in eq. 2.45 is the forward and backward rate coefficients k_{fr} and k_{br}. In theory it is possible to derive k_{fr} through kinetic theory, assuming interaction potential, dissociation-recombination probabilities and exact distribution functions are known. In practice however, this is difficult due to much of the information is unknown. Instead a semi-empirical equation, called Arrhenius equation is used, and is defined as:

$$k_{fr} = A_r e^{\frac{-E_r}{RT}} \tag{2.47}$$

where A_r is a constant pre-exponential factor, E_r is the activation energy for reaction r, R is universal gas constant and T is temperature [23, 19]. In this equation, A_r is considered temperature independent, which is an approximation, resulting in this equation often being rewritten to the modified Arrhenius equation:

$$k_{fr} = A_r T^n e^{\frac{-E_r}{RT}} \tag{2.48}$$

where a temperature dependence is added to the pre-exponential factor [23]. A_r and n are derived from experimental data of k_f resulting in a large differences, often up to several magnitudes, between different authors [19]. The modified Arrhenius equation is only valid for thermal equilibrium [19].

The backward rate constant k_{br} can be modeled in several different ways and is not as straight forward as k_{fr}. Generally two approaches can be made, first is assuming k_{br} follows Arrhenius equation 2.49, where A_{br}, n_{br} and E_{br} are the backward reaction values and is independent of k_{fr}, second is assuming k_{br} is a function of k_{fr} according to equation 2.50 where K_p is the equilibrium constant defined by equation 2.40 [19, 20]. For high velocity flows, the second method, using equation 2.50, is considered more accurate [20].

$$k_{br} = A_{br} T^{n_{br}} e^{\frac{-E_{br}}{RT}} \tag{2.49}$$

$$k_{br} = \frac{k_f}{K_p} \tag{2.50}$$

2.8.4 Chemical timescales of reentry

In general the chemical timescales for combustion is very small and the flow timescales large at high temperatures and pressures found in the combustion chamber making chemical equilibrium a good assumption. However, once ejected through the nozzle the timescales for post combustion is vastly different where the flow timescale is small due to the high velocities and large chemical timescales due to slow reactions, sometimes exceeding flow timescales by several orders of magnitude, making frozen chemistry a good assumption. This means that there are regions with high, low and intermediate Da, making frozen chemistry, chemical equilibrium and chemical non-equilibrium all good approximations in different regions of the flow [2]. Studies comparing chemistry models in supersonic reentry propulsion has shown that for hydrogen fuels, the rocket wall temperature was about 200 K higher for reacting chemistry while for the carbon based kerosene fuel, the difference was nearly 700 K (corresponding to 50% error). This shows that the choice of fuel will heavily impact the effects of post combustion, and therefore also the effects of chemistry models [2].

2.8.5 Air species model for reentry

As mentioned earlier a chemistry model needs to be chosen as a balance between computational cost and model accuracy. This means that the best model is the simplest model that still captures relevant chemistry. As also mentioned earlier, air will dissociate, exchange atoms and ionize all different at temperatures. This means that an air model needs to be chosen that is appropriate for the temperatures reached at different altitudes and velocities.

Many air models taking chemical reactions into considerations has been developed containing a variety of different species . For air there are three common species models, 5-species, 7-species and 11-species [19].

- **5-species:** This is the simplest species and is used when dissociation and atom exchange is present, but ionization is neglegible. The species considered is: N_2, O_2, NO, N, O.
- **7-species:** When ionisation starts to become relevant (usually around 9000 K) one needs to add ions and electrons as species to the model. The species then become: $N_2, O_2, NO, N, O, NO^+, e^-$.
- **11-species:** When temperatures increase even further more species begin to ionize and additional ion-species needs to be considered. The species then become:
  $N_2, O_2, NO, N, O, N_2^+, O_2^+, NO^+, N^+, O^+, NO^+, e^-$

The reactions can be broken down into thermal dissociation, bimolecular exhange, associative ionization-dissociative recombination, charge exchange, heavy particle impact ionization and electron impact ionization where the 11-species model takes all of the reactions into consideration [19]. The reactions are displayed in table 2.1 where X denotes arbitrary third party species. Reactions 1-5 is considered in the 5-species model, 1-6 in the 7 species model and 1-23 in the 11-species model [9].

Thermal dissociation	
1	$O_2 + X \Leftrightarrow O + O + X$
2	$N_2 + X \Leftrightarrow N + N + X$
3	$NO + X \Leftrightarrow N + O + X$
Bimolecular exchange	
4	$O_2 + N \Leftrightarrow NO + O$
5	$N_2 + O \Leftrightarrow NO + N$
Associative ionization-dissociative recombination	
6	$N + O \Leftrightarrow NO^+ + e^-$
7	$N + N \Leftrightarrow N_2^+ + e^-$
8	$O + O \Leftrightarrow O_2^+ + e^-$
Charge exchange	
9	$NO^+ + O \Leftrightarrow N^+ + O_2$
10	$O_2^+ + N \Leftrightarrow N^+ + O_2$
11	$O^+ + NO \Leftrightarrow N^+ + O_2$
12	$N^+ + N_2 \Leftrightarrow N_2^+ + N$
13	$O_2^+ + N_2 \Leftrightarrow N_2^+ + O_2$
14	$O^+ + N_2 \Leftrightarrow N_2^+ + O$
15	$NO^+ + N \Leftrightarrow N_2^+ + O$
16	$O_2^+ + O \Leftrightarrow O^+ + O_2$
17	$NO^+ + N \Leftrightarrow O^+ + N_2$
18	$NO^+ + O_2 \Leftrightarrow O_2^+ + NO$
19	$NO^+ + O \Leftrightarrow O_2^+ + N$
Heavy particle impact ionization	
20	$O_2 + N_2 \Leftrightarrow NO + NO^+ + e^-$
21	$NO + X \Leftrightarrow NO^+ + e^- + X$
Electron impact ionization	
22	$O + e^- \Leftrightarrow O^+ + e^- + e^-$
23	$N + e^- \Leftrightarrow N^+ + e^- + e^-$

Table 2.1: 11-species reactions scheme from Gupta et. al. 1990 and Park 1993 [19]

3

Methods

In this chapter the methodology used during the thesis will be presented. This includes the general approach to the study, the used software such as the meshing tool and CFD program along with the CAD model and the used chemistry- and turbulence models.

3.1 General Methodology

The first thing carried out in this thesis was a literature study. The study was done to both increase the authors knowledge in the relevant field but also to investigate the state-of-the-art simulation tools/models for this research topic. The literature study went through general theory about reentry and retro-propulsion. This includes different chemical air models, turbulence models and experiments associated with reentry. CFD simulations in ANSYS Fluent were conducted, starting with simple models and geometry and gradually increase the complexity. The next step was to take the rocket geometry developed by the German Aerospace Center (DRL), and remove the landing legs and control fins as the flow behaviour on and around the nozzles and base of the rocket is the main focus of investigation in this project.

A prestudy was conducted using a 2D axisymmetric model to compare multiple model settings at a lower computational cost, allowing for additional simulations to be performed within the available time. Apart from general settings to improve convergence and accuracy, investigative simulations were made, with- and without retro-propulsion, and analyzed in order to derive: chemical models effects on temperature, chemical models effects on heat transfer coefficient and chosen wall temperature boundary conditions effects on heat transfer coefficient. The result from the prestudy was then used in order to run accurate 3D simulations with lower computational cost.

A final model was set up in 3D, with a quarter domain due to symmetry. The 3D simulations used the computationally cheapest but necessary settings found from the prestudy in order to investigate adiabatic wall temperature, heat transfer coefficient and wall heat flux with and without retro-propulsion for start and end burn on the nozzles and baseplate of the rocket.

3.2 Standard rocket model

The data used for this project such as engine data, trajectory and CAD model used to investigate aerodynamic and thermal loads on a re-usable launch vehicle was taken from a EU project carried out by the German Aerospace Center (DLR) [24]. The engine data includes velocity, temperature and pressure along with other properties as a function of the radius at the nozzle exit. This data was used as a boundary condition at the nozzle exit in the CFD simulation. This was done to save computational time as the flow inside the nozzle doesn't have to be simulated. During the reentry burn the nozzle will be underexpanded and therefore the flow outside won't affect the flow inside the nozzle and therefore putting a profile of the velocity, pressure and temperature as boundary condition will be a good approximation. The trajectory data contains atmospheric data, the velocity that the spacecraft is traveling with and what state (on/off) each engine is. This data was used to specify the air properties at the pressure farfield for the simulation at a given operating point. The data used is presented in table 3.1 and showcases the operating point at the start of the reentry burn and the end of it.

Table 3.1: Air data used as boundary condition at the pressure farfield.

	Start of burn	End of burn
Mach	7.14	5.35
Altitude	57.66 km	39.06 km
Pressure	30.02 Pa	327.6 Pa
Temperature	253.33 K	247.88 K

The CAD model was also taken from DLR and was used for the simulations. The model was simplified by removing parts which was deemed uninteresting and would only increase complexity for meshing. This included parts such as the landing legs and the control fins. A comparison between the original rocket and the simulated one in this thesis is illustrated in figure 3.1. The simulated rocket was also reduced to only a quarter of the rocket, this is due to the presence of symmetry as the rocket will have 3 engines on during the reentry burn at 100 % throttle (engine 1, 5 and 9 in figure 3.2).

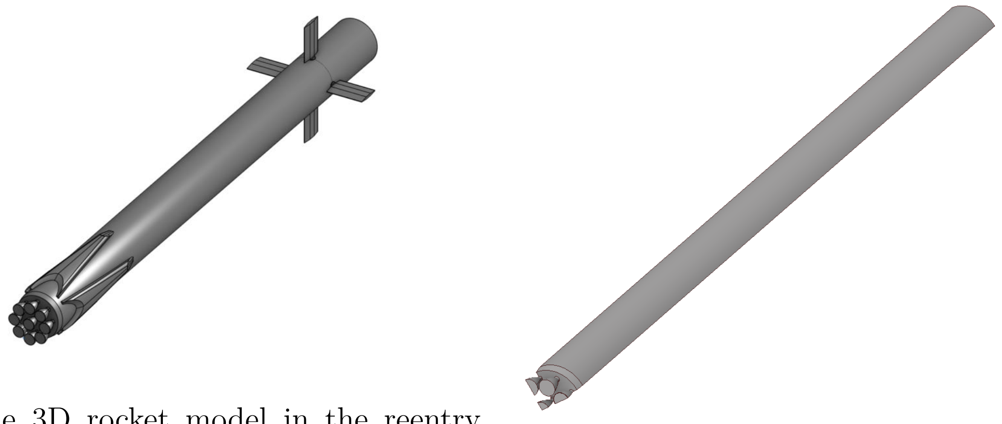

(a) The 3D rocket model in the reentry configuration used by DLR in the RETPRO project [24].

(b) The simplified 3D model without fins and landing gear.

Figure 3.1: Comparison between the rocket model used in the RETPRO project and the simplified model used in this project.

For the 2D axisymmetric case only the center nozzle was simulated as it wasn't possible to include the outer engines with an axisymmetric model. Even though the reentry burn has all three engines on at 100 % throttle the 2D case will only simulate 1 of the engines.

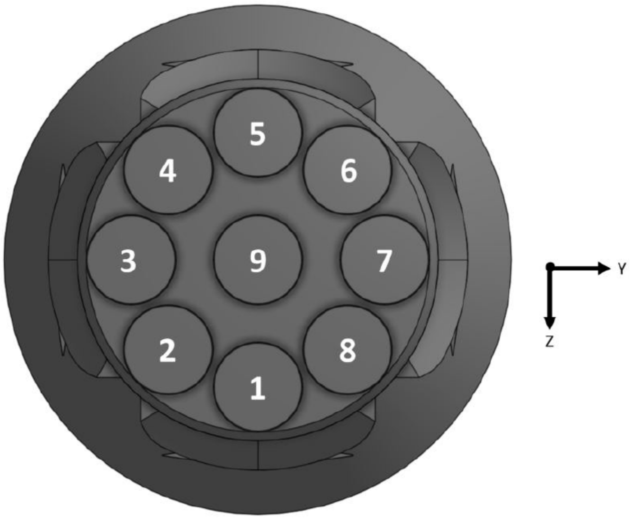

Figure 3.2: The nozzle configuration with numbering of each engine [24].

The nozzle geometry used in the DLR rocket is a truncated ideal contour (TIC) nozzle and is illustrated in figure 3.3. This nozzle geometry will be used for all simulations including both the 2D axisymmetric and the 3D simulations. However the nozzle was intruded a couple of cell lengths as can be seen in figure 3.8d. This was done so that the flow at the exit could develop a boundary layer before it meets the exit where there will develop an expansion fan. If there is no boundary layer, the flow will exhibit a large expansion due to the turning of a supersonic flow which was found to cause numerical difficulties in the region. The modification of an intruded nozzle mitigated the divergence of the flow around the nozzle exit. As mentioned, an exit profile of the velocity, pressure and temperature was used for the nozzle and is shown in figure 3.4 below. Even though the outer CAD is that of a TIC nozzle, the exit conditions were for a similar RAO nozzle designed for the same thrust and fuel configuration. The small deviation in the exit profile is not considered to affect the simulation results.

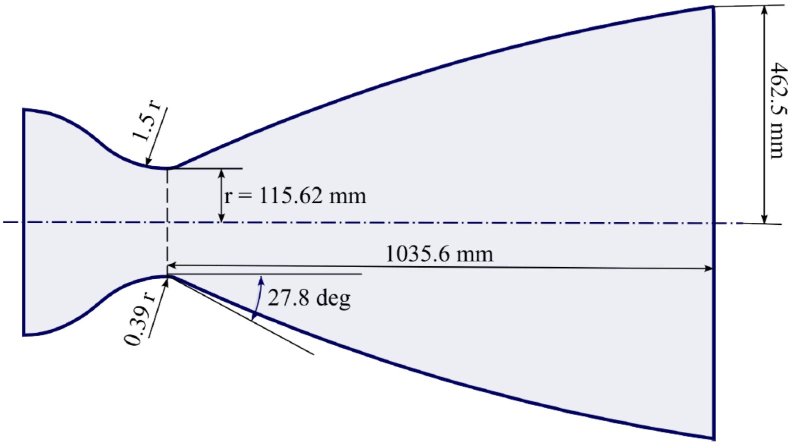

Figure 3.3: The nozzle contour and it's dimensions used in this simulation [25].

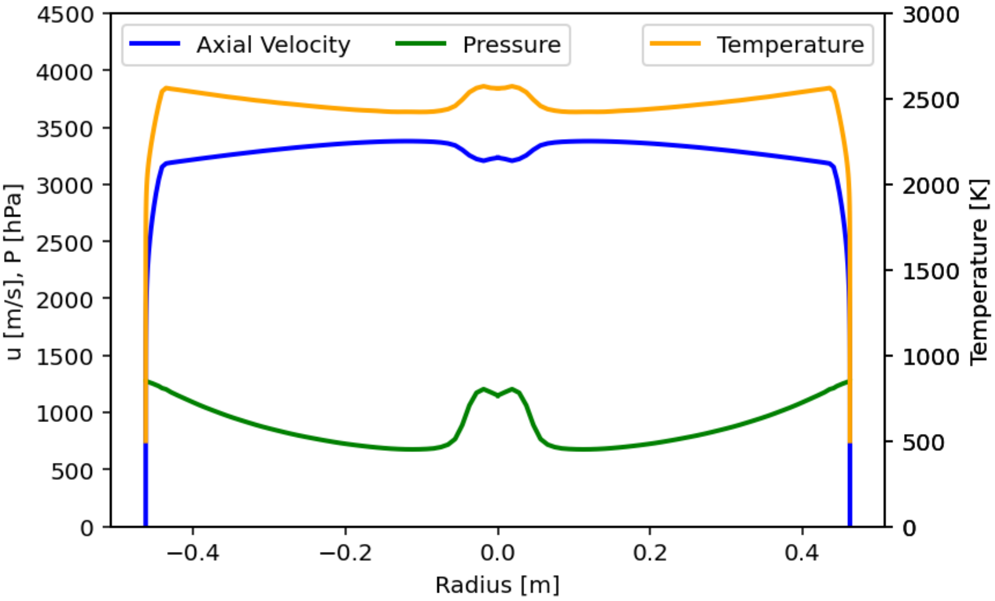

Figure 3.4: Exit profiles for axial velocity, pressure and temperature for the nozzle taken from [25].

3.3 Simulation set-up

Two different domains were used for simulating the reentry burn. One 2D axisymmetric domain used for prestudy and one 3D domain, illustrated below in figure 3.5 and 3.6 respectively. For both cases ANSYS Fluent was used to run the CFD simulations. An implicit density based steady state solver was used with second order spatial discretization scheme for the flow (pressure, momentum and energy), turbulent kinetic energy and the specific dissipation rate. The built-in high speed numerics in Fluent was used for the simulations as it helped with preventing local divergence during retro-propulsion around the nozzle exit, where the exhaust is expanding, as well as around the shock waves. The turbulence model used in this thesis is the $k-\omega$ SST model with Fluent's correlation based y^+-insensitive near-wall treatment which uses analytical expressions to blend between the viscous sublayer and the logarithmic part. The model uses a low Reynolds number formulation when $y^+ < 5$ and a high Reynolds number formulation which utilizes wall functions is used for $y^+ > 30$. A criteria of a $y^+ < 0.1$ was used for the nozzle wall and rocket base plate, in order to accurately capture the heat fluxes, while the rest of the rocket walls has a $y^+ < 1$. Therefore, every first cell on the rocket will be in the viscous sublayer and thus a low Reynolds number formulation will be used. One exception is the wall normal to the flow at the intruded nozzle wall where the first cell height will be in the buffer layer. But as that area is only made to help with convergence and will not be analyzed, it's deemed fine for this project. As the simulation is expected to be well below the limit for thermochemical non-equilibrium, a one temperature model was used for the energy equation. For the 2D case a semicircle of the domain is used where the radius of the circle has a size of 50 rocket lengths (RL). The boundary conditions used for this setup is:

- **Pressure far-field:** The boundary condition used for the arch of the domain was a pressure far-field where the Mach number, pressure and temperature was specified using the DLR data which represents International Standard Atmosphere (ISA). The chemical composition used for air was 24 % O_2 and 76 % N_2.

- **Axis:** For the symmetry line an axis boundary condition was used.

- **Rocket walls:** For all the rocket walls an adiabatic wall with no-slip condition was used. When the heat transfer coefficient is being calculated a prescribed temperature is used as a temperature boundary condition for the walls under investigation.

- **Nozzle exit:** For the case during retro-propulsion a velocity inlet is used where a profile on the velocity, pressure and temperature is used. For the case where the engines are off a no-slip adiabatic wall is used and when the heat transfer coefficient is being calculated a prescribed temperature is used as a temperature boundary condition.

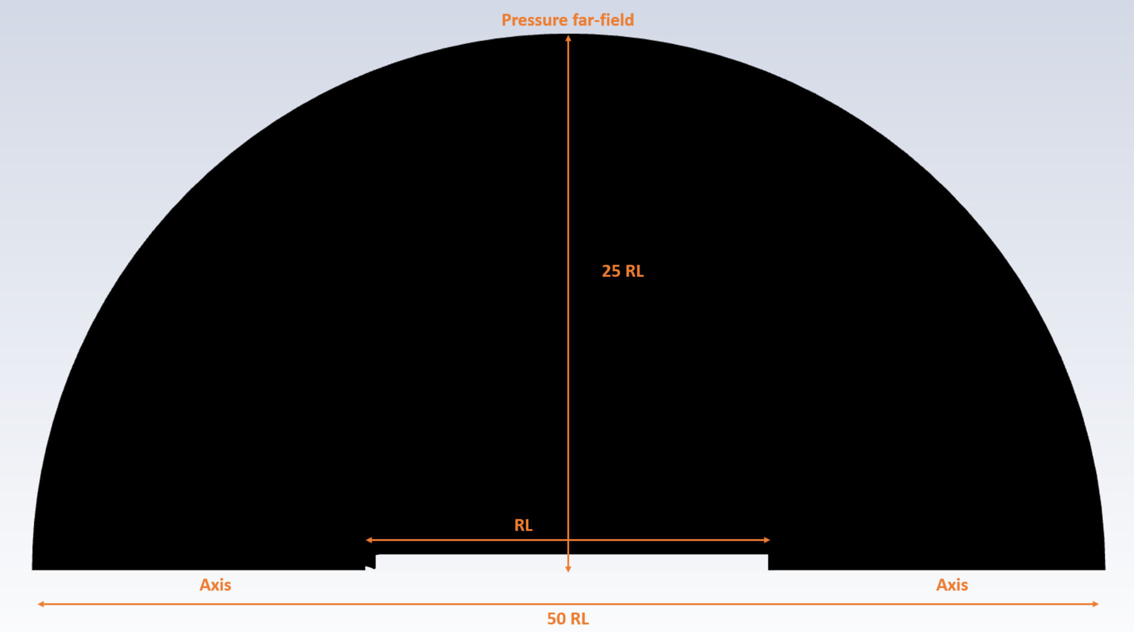

Figure 3.5: The 2D axisymmetric domain, where a rocket length is denoted as RL. The rocket has been enlarged to make it visible in the domain

For the 3D domain a quarter of the domain was simulated as the rocket can be divided due to symmetry as it has 3 active engines, located in line, as illustrated in figure 3.7. In contrast to the 2D case the domain was changed to a cylinder. This was due to the fact that initial simulations utilized poly-hexcore cells (which work better with a cylinder domain) with an adaptive mesh. But due to large final mesh sizes, this was replaced with a fixed unstructured mesh with polyhedral cells. After the change in mesh the cylindrical domain was kept for all 3D simulations. The domain size in terms of the radius was also changed compared to the 2D case. The radius was reduced to half it's original length as it was deemed to be large enough from the 2D results. The boundary conditions used in this setup are as follow:

- **Pressure far-field:** The boundary condition used for the inlet, outlet and arch of the domain was a pressure far-field where the Mach number, pressure and temperature was specified using the DLR data and the chemical composition used for air was 24 % O_2 and 76 % N_2.

- **Symmetry:** For the symmetry surface at each side of the quarter a symmetry boundary condition was used.

- **Rocket walls:** For all the rocket walls an adiabatic wall with no-slip condition was used. When the heat transfer coefficient is being calculated, the adiabatic temperature profile is used as a temperature boundary condition for the walls under investigation.

- **Nozzle exit:** For the case during retro-propulsion a velocity inlet is used for two of the nozzles as shown in figure 3.7 where a profile on the velocity, pressure and temperature is used according to figure 3.4. The chemical composition used for the exhaust species is according to table 3.7. For the case where the engines are off a no-slip adiabatic wall is used and when the heat transfer coefficient is being calculated, the adiabatic temperature profile is used as a temperature boundary condition on all the nozzles.

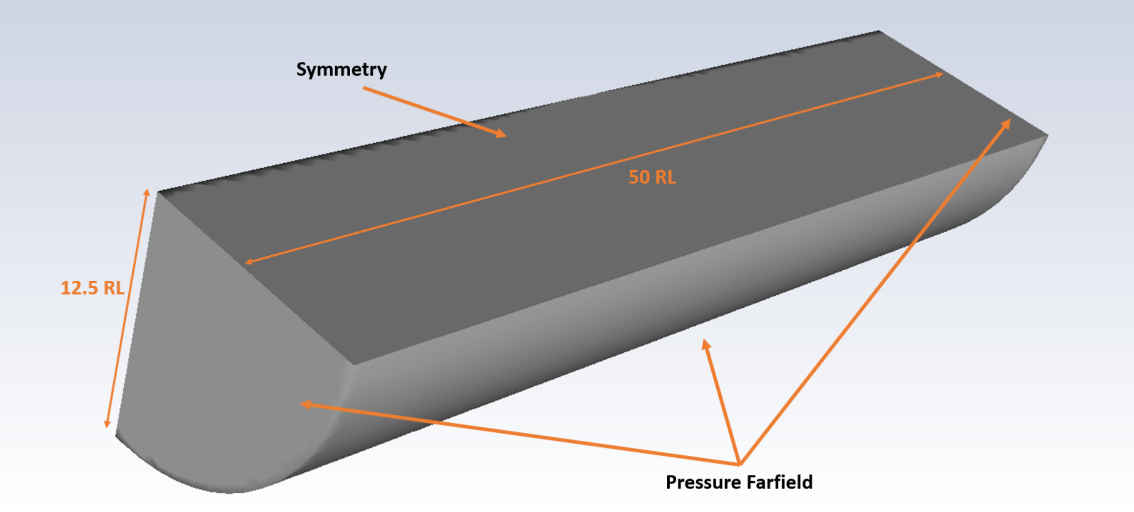

Figure 3.6: The 3D domain used in ANSYS Fluent.

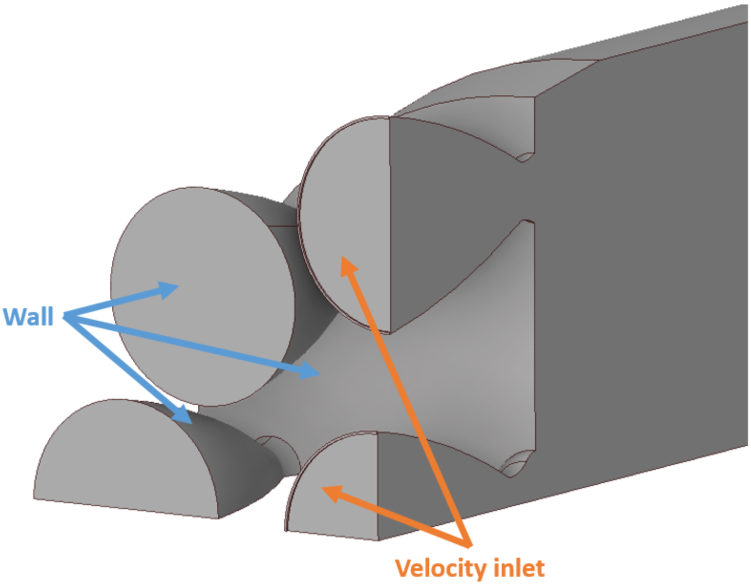

Figure 3.7: A close-up view of the nozzles in the 3D domain and the used boundary condition.

3.4 Heat transfer simulations in 3D

To conduct the heat transfer simulations which is to calculate the HTC and heat flux, an initial adiabatic simulation was needed. This is because the adiabatic temperature will be used according to equation 2.23 to calculate the heat transfer coefficient. The extracted temperature profile was then used to subtract 100 K from every point and then import it as a temperature boundary condition at the rocket nozzle walls and base plate. The 100 K was chosen as it was large enough to minimize effects of numerical errors, but low enough to not affect the flow behavior. From here on, one can use equation 2.23 together with the resulting heat flux and adiabatic wall temperature in order to calculate the heat transfer coefficient h. When the heat transfer coefficient was to be calculated, both simulations with and without retro-propulsion, the frozen chemistry model was used in order to extract both the adiabatic temperature and the heat flux. In section 4.1.2, it was shown that the heat transfer coefficient is fairly similar between the frozen chemistry model and the chemical non-equilibrium model, and to save computational time, the frozen chemistry model was used to calculate the heat transfer coefficient regardless if the engines were on or not.

Additional simulations were also conducted in order to estimate the total wall heat flux, which used a constant wall temperature of 300 K. 300 K was chosen as it is a feasible temperature of the nozzle walls when being cooled from the cooling channels, and a constant temperature of 300 K is also the most common temperature used in earlier studies [2] on heat flux during retro-propulsion. For simulations without retro-propulsion the frozen chemistry model was used while with retro-propulsion a non-equilibrium chemistry model was used. The choice of chemical model stems from the results in section 4.1.1 where it was showed that frozen chemistry was an accurate model for simulations with the engines off while during retro-propulsion a non-equilibrium chemistry model is needed to accurately model the temperature, and as a result capture the heat fluxes.

3.5 Mesh

Two different meshing tools was used in this thesis. The meshing tool ANSYS ICEM CFD was used for the 2D axisymmetric case while Ansys Fluent Meshing was used to mesh the 3D case. In ICEM a structured mesh was used as shown in figure 3.8. The choice to use a structured mesh was made because of the simplicity and high quality that it offers. Due to limitations of structured meshes in terms of handling complex geometries an unstructured mesh was used for the 3D case. For the 2D case, the mesh was divided into blocks with four levels of o-grids around the rocket. The outermost o-grid was designed in order to capture the freestream and get the flow to settle, the second layer was designed to capture the behaviour of the plume, the third layer to capture flow around the rocket while the innermost was designed to capture the boundary layers and heat transfer. In regions of investigation, the first layer height was determined such as the average y^+ at the nozzle wall should be under 0.1 to make sure that both the velocity- and the thermal boundary layer was resolved.

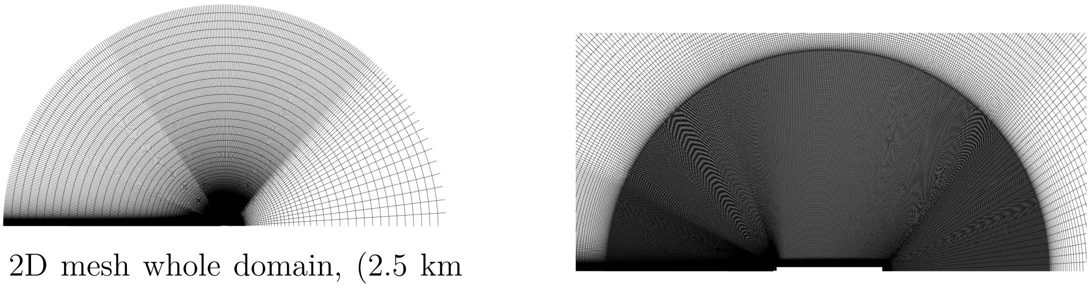

(a) 2D mesh whole domain, (2.5 km wide).

(b) 2D mesh zoom.

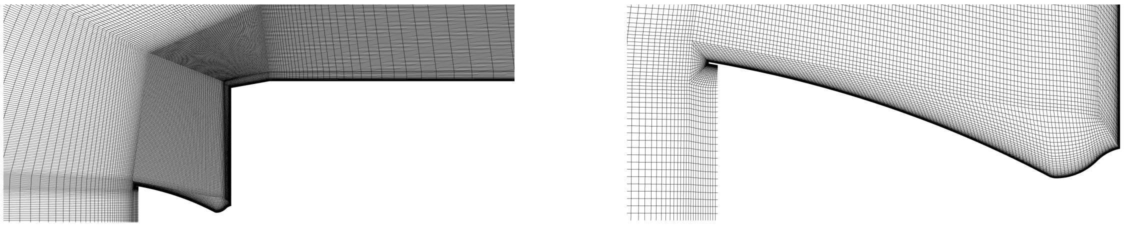

(c) 2D mesh front of rocket.

(d) 2D mesh nozzle.

Figure 3.8: 2D structured mesh made in Ansys ICEM, 255,000 cells.

Due to the significant difference in flow behavior between simulations with and without retro-propulsion, it was decided to make two different meshes. By having two meshes, it was possible to greatly reduce the number of elements for the simulations without retro-propulsion as there was no plume that needed to be resolved, and thereby significantly reducing the computational cost. The mesh was an unstructured polyhedral mesh with inflation layers to ensure a $y^+ < 0.1$ around the nozzle walls and base plate. Both the meshes generated are shown in figure 3.9 and 3.10 respectively.

In order to resolve the flow, boxes with different mesh sizes was used in the same way as the ogrids in the 2D mesh. The outermost box encapsulating the entire domain was designed in order to settle the freestream flow, the second box to capture the plume (only for mesh for retro-propulsion), third box to captures the flow around nozzles and a final inflation layers to capture boundary layers. A surface refinement was also made on the nozzles to better capture the large gradients.

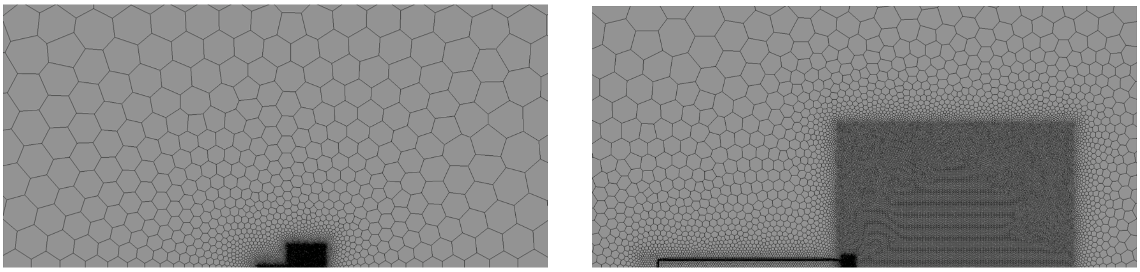

(a) 3D mesh whole domain. **(b)** 3D mesh zoom.

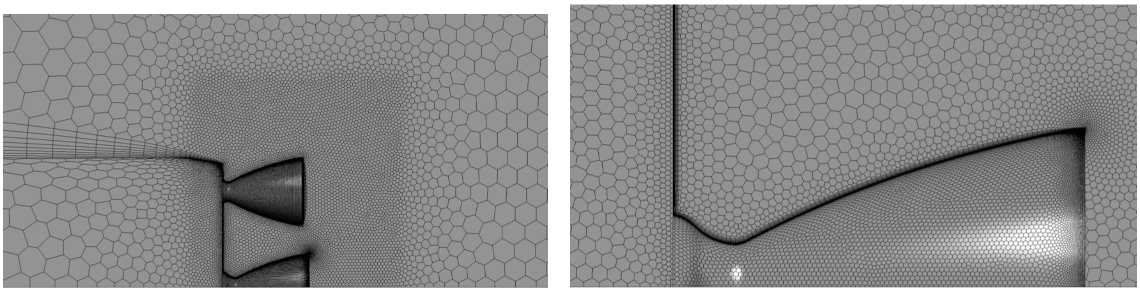

(c) 3D mesh front of rocket. **(d)** 3D mesh nozzle.

Figure 3.9: 3D unstructured polyhedral mesh done in ANSYS Fluent Meshing for the case with the engines on.

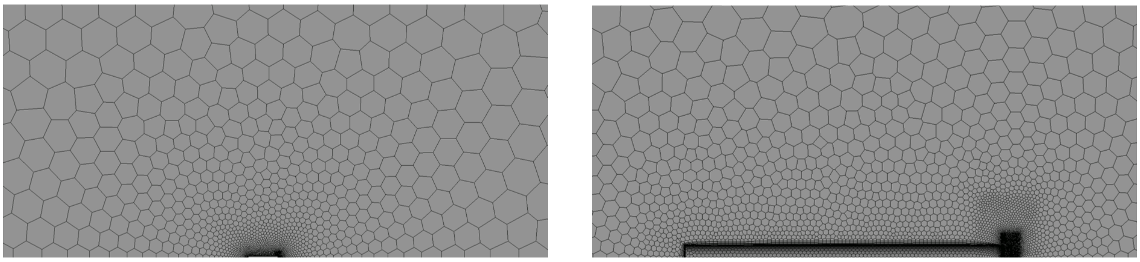

(a) 3D mesh whole domain. **(b)** 3D mesh zoom.

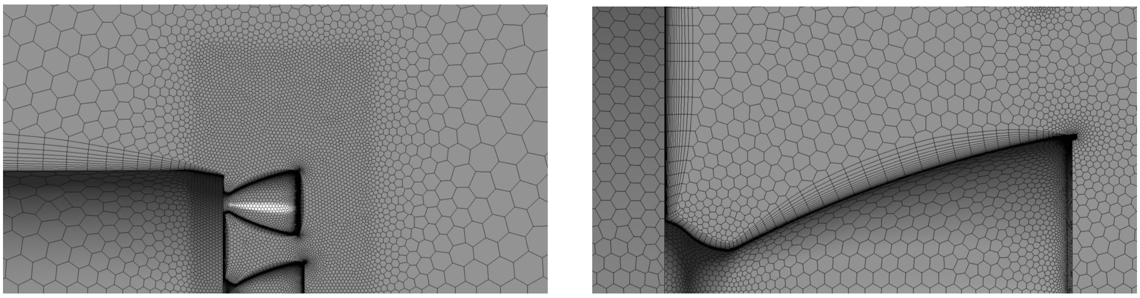

(c) 3D mesh front of rocket. **(d)** 3D mesh nozzle.

Figure 3.10: 3D unstructured polyhedral mesh done in ANSYS Fluent Meshing for the case with the engines off.

3.5.1 Mesh convergence study

The first mesh convergence study was made for the 2D case without retro-propulsion. To save time, calorically perfect gas was used to conduct the mesh convergence study as that resulted in faster simulation times. A Richardson extrapolation was used on the study according to the following equations:

$$\begin{aligned} p &= \frac{ln(\frac{f_3-f_2}{f_2-f_1})}{ln(r)} \\ f_{h=0} &= f_1 + \frac{f_1-f_2}{r^p-1} \end{aligned} \tag{3.1}$$

where f is a variable of the simulation, p is the order of convergence and r is the grid refinement ratio. The Richardson extrapolation should yield a value representing the quantity of the variable the mesh would achieve with zero grid spacing. Three different meshes was used in the mesh study with the area weighted average temperature on the nozzle wall as the value to assess convergence. Temperature was chosen as a convergence criteria as it is highly related to thermal loading, the main goal of this project. All of the meshes has an area-weighted average y^+ of below 0.1 at the nozzle wall. The difference in temperature was compared to the extrapolated value and is shown in table 3.2 below.

Table 3.2: Mesh convergence study for the 2D case without the exhaust plume. The temperature is the average value of the nozzle wall with adiabatic wall boundary condition.

Mesh	$N_{cells}[10^5]$	T [K]	$\Delta T[\%]$
Richardson Extrapolation	-	2778.60	0
Fine	6.694	2775.727	0.103
Medium	**2.975**	**2773.880**	**0.169**
Coarse	0.744	2768.713	0.356

A common criteria for convergence is that the quantity observed shouldn't change more than 1 % from one mesh to the next. It can be observed that all achieves that criteria which indicates that the coarsest mesh should be used to save computational time. But as there are shocks in the simulation, the ability to capture the shock without too much numerical dissipation was also taken into consideration and therefore the medium mesh was chosen.

It was observed that all of the meshes achieved an area-weighted average of y^+ of below 0.005 which is lower than the set criteria of 0.1. This contributes to a higher computational time without a noticeable gain in accuracy and therefore the chosen mesh was adjusted by increasing the first cell height which resulted in an area-weighted y^+ of 0.042 which is still below the criteria. This new mesh resulted in an averaged wall temperature of 2770.16 K which is 0.134 % difference from the original chosen mesh and a 0.304 % difference to the extrapolated value which meant that revised mesh could still be chosen. A mesh convergence study was made for retro-propulsion with the new revised mesh and calorically perfect gas. The new medium mesh showed good correlation with only a 0.6% difference compared to coarse mesh and a y^+ of 0.003. The results were not added to the table due to numerical errors with fine mesh, but due to medium mesh being chosen and having good correlation with coarse, this was not deemed an issue.

For the 3D simulation a similar mesh convergence study was done as to 2D but two different meshes were generated, one for simulations with retro-propulsion and one without. This is due to simulations without retro-propulsion the bow shock will be located close to the rocket and therefore one could decrease the size of the refinement region compared to the case with the engines on and save computational time. The mesh convergence study used the frozen chemistry model due to calorically perfect gas would expand the plume further which results in a a larger refinement region needed which would be unnecessary when later switching to the chemical models. The results are shown below in table 3.3 and 3.4.

The results for the case with retro-propulsion shows that there is a difference of 5.54 % between the fine mesh and the extrapolated value. This value is higher than the set requirement of < 1 % and indicates that a refinement should be made. But it was noted that when using a chemical non-equilibrium model, the simulation ran into RAM problems(as described in section 3.6.3) and therefore it could not be refined more. Even though this comes with a cost in accuracy it will result in higher temperatures, and as a result, conservative heat fluxes.

For the case without retro-propulsion, the difference between the meshes were negligible but as the coarse mesh resulted in a lot of numerical dissipation across the bow shock the medium mesh was chosen. The increase in y^+ for the medium mesh compared to the coarse and fine mesh is due to the fact that the transition ratio and growth ratio in the boundary layers had to be modified to ensure a high quality mesh and in the case of the medium mesh it resulted in an increase in y^+ but as the value is close to 0.1 it was deemed ok. It was later shown that large temperature gradients existed near the nozzle exit and therefore the mesh needed to be refined around the exit which resulted in an increase in amount of cells. This increase resulted in around 2.09 million cells but the area averaged temperature of the center nozzle was 2458.06 K which is a 0.024 % difference from the chosen mesh and a 0.033 % difference to the extrapolated value and was therefore deemed fine to use.

Table 3.3: Mesh convergence study for the 3D case with an exhaust plume. The temperature is the average value of the nozzle wall with adiabatic wall boundary condition.

Mesh	$N_{cells} [10^6]$	T [K]	$\Delta T [\%]$	y^+
Richardson Extrapolation	-	3018.87	0	-
Fine	**6.24**	**3186.91**	**5.54**	**0.045**
Medium	2.45	3249.03	7.59	0.06
Coarse	0.989	3333.44	10.41	0.074

Table 3.4: Mesh convergence study for the 3D case without an exhaust plume. The temperature is the average value of the nozzle wall with adiabatic wall boundary condition.

Mesh	$N_{cells}[10^6]$	T [K]	$\Delta T[\%]$	y^+
Richardson Extrapolation	-	2457.24	0	-
Fine	1.54	2457.647	0.0167	0.0896
Medium	**0.639**	**2458.66**	**0.0578**	**0.1107**
Coarse	0.336	2458.952	0.097	0.0697

3.6 Chemistry models

As mentioned earlier, the chemistry models is an important parameter in the simulations. One of the things investigated during the prestudy was how the chemistry models affects the temperature around the plume, shockwave and the nozzle wall, as well as how the models affects the shape and position of the plume and shock waves. The chemical models investigated were: calorically perfect gas (where there was only one and the same specie for the atmosphere and exhaust), frozen chemistry, chemical equilibrium and chemical non-equilibrium. All chemistry models where simulated at two different phases of flight (start burn and end burn, values from table 3.1) as well as with and without retro-propulsion. In other words, all chemistry models were simulated at four different operating conditions.

3.6.1 CHEMKIN

As previously mentioned, a CFD solver needs to have information about the species present in the flow. The easiest and most appropriate way to incorporate this in Ansys Fluent is the use of datafiles in CHEMKIN format. For thermodynamic properties CHEMKIN format uses NASA 7-coefficient format where the individual species' properties specific heat constant (c_p), enthalpy (H) and entropy (S) are calculated based on the equations 3.2, 3.3 and 3.4 respectively, where R is universal gas constant, T is temperature solved for in the simulations and a_n are the given polynomials [26]. Transport properties are given as a table containing the information seen in table 3.5 [27]. Lastly, the reactions are given according to the the constants A_r, n and E_r used in the modified Arrhenius Equation (eq. 2.48) [28]. The backward reaction rate constant is determined by reverse Arrhenius Equation (eq. 2.49) if not directly specified, otherwise the backward reaction rate constant is determined by eq. 2.50 [29].

$$\frac{c_p}{R} = a_1 + a_2 T + a_3 T^2 + a_4 T^3 + a_5 T^4 \tag{3.2}$$

$$\frac{H}{RT} = a_1 + \frac{a_2}{2} T + \frac{a_3}{3} T^2 + \frac{a_4}{4} T^3 + \frac{a_5}{5} T^4 + \frac{a_6}{T} \tag{3.3}$$

$$\frac{S}{R} = a_1 \ln T + a_2 T + \frac{a_3}{2} T^2 + \frac{a_4}{3} T^3 + \frac{a_5}{4} T^4 + a_7 \tag{3.4}$$

Table 3.5: Transport parameters in CHEMKIN format [27].

Parameter	Unit
Index for geometrical configuration	[-]
Lennart-Jones potential well depth ($\frac{\epsilon}{k_B}$)	[K]
Lennart-Jones collision diameter (σ)	[Å]
Dipole moment (μ)	[D]
Polarizability (α)	[Å^3]
Rotational relaxation collision number at 298 K (Z_{rot})	[-]

3.6.2 Species & chemical data

For air, the chosen composition was 24% O_2 and 76% N_2 in line with DRLs' study in the RETPRO project [4]. A 5-specie air model containing N_2, O_2, NO, O and N was chosen as previous studies has shown it to be sufficient to capture relevant reactions while also minimizing computational cost [19]. The transport and thermodynamical properties were taken from CHEMKIN transport- and thermodynamical databases respectively while reaction data were taken from Park2001 model [30] and displayed in appendix A.1.

The exhaust species were calculated using NASA CEA tool, a chemical equilibrium solver for theoretical rocket performance analyses. The input for NASA CEA was taken from the standard rocket model [24] where the geometry and flight data is also taken from. The standard rocket model was originally developed for a kerosene engine, however a later study was made for the same rocket design by DLR but with modified data for a methane engine designed to have the same thrust as the original kerosene engine [25]. The data from [25], which can be seen in table 3.6, was used as input data for NASA CEA. The outcome from NASA CEA is the mass fraction of species seen in table 3.7 which was used as a homogeneous specie composition for the boundary conditions for the exhaust of the nozzle.

Table 3.6: Input data from [25].

Variable	Value
Chamber pressure	106 bar
Oxidiser/fuel	3.5
Area ratio (A_e/A_t)	16
Chemistry model	Chemical equilibrium

Table 3.7: Output data from NASA CEA, species with massfraction $< 5 \cdot 10^{-6}$ were disregarded.

Species	Mass fraction
H_2O	0.45582
CO_2	0.40774
CO	0.12849
H_2	0.00460
OH	0.00268
O_2	0.00053
H	0.00008
O	0.00006

The methane reaction model used was a skeletal combustion model developed by Zhukov and Kong in 2018 for liquid methane and liquid oxygen rocket engines and is a reduced model based on a larger model, also by Zhukov and Kong, from 2009 [31]. The original model contained 207 species and 1260 reactions which, with the newer model, was reduced to 23 species and 51 reactions maintaining high accuracy with greatly improved computational cost. The model was originally developed for reactions in combustion chambers with high pressures (evaluated at 60 bar [31]) and low chemical timescales in contrast to post combustion in retro-propulsion where the pressures are near vacuum and time-scales significantly larger. Due to limited options of chemical models at low pressures, Zhukov-Kongs' model was chosen since it contained many of the reactions likely also found in post combustion. The model can be seen in appendix A.2-A.4. A modification was made where the species Ar (Argon) and He (Helium) were removed in order to decrease computational costs. This was deemed to not impact the results as they are not present in our domain. Since the Zhukov-Kong model only contained methane combustion model, Park2001 air model was added to be able to model atmospheric reactions along with methane reaction.

3.6.3 Reduced chemical model

For the final 3D simulations with exhaust and reacting chemistry the model had about 6 million cells and 24 species. This resulted in a unfeasible amount of RAM memory in order to initiate and run the simulations. Since the mesh size was deemed necessary and a mesh size reduction would come at a great cost of accuracy a study was made on the effect of reducing the number of species in the domain. Species with a global maximum of mass fraction less than $1 \cdot 10^{-7}$ was removed from the methane chemistry model resulting in 10-specie model (seen in appendix A.5). The reduced methane model was, as earlier, combined with the Park2001 air model to make a 13-specie chemistry model. A comparison between the full 24-specie model and the reduced 13-specie model was conducted in 2D and can be seen in section 4.1.3 and show nearly perfect coincidence with the full chemistry model and therefore this reduced chemistry model was used for all simulations in 3D with exhaust and chemical non-equilibrium.

3.7 Chemistry model and heat transfer

As is later shown in section 4.1.2 the heat transfer coefficient ($h = \frac{\Delta T}{q}$) is only a function of flow and geometry and is temperature independent. As the chemistry models will heavily affect the temperature in the flow, however, the impact of the flow and therefore the heat transfer coefficient is uncertain. The theory being that frozen chemistry will give a similar heat transfer coefficient as chemical equilibrium and therefore a reduced frozen chemistry model could be adopted in order to further reduce the computational cost of the 3D simulations. The results from 2D simulations, shown later in section 4.1.3, show that even if a non-equilibrium model is more conservative, the difference is small and therefore frozen chemistry was adopted for heat transfer coefficient simulations in 3D. For heat flux simulations however, the adiabatic wall temperature effects is necessary and therefore used.

4

Results & Discussion

In this section the results from the simulations will be shown and discussed starting with the prestudy in 2D and moving towards the full 3D simulations with and without retro-propulsion.

4.1 Prestudy in 2D

The flow behavior in 2D without retro-propulsion can be seen in figure 4.1. In front of the nozzle a bow shock takes place which rapidly decreases the mach number and increases the temperature. On the side of the nozzle the bow shock becomes more angled as it's turning the flow around the nozzle and the rocket. The highest temperatures are found near the nozzle and the base plate of the rocket (the area connecting the nozzle with the rocket) which later is transported downstream.

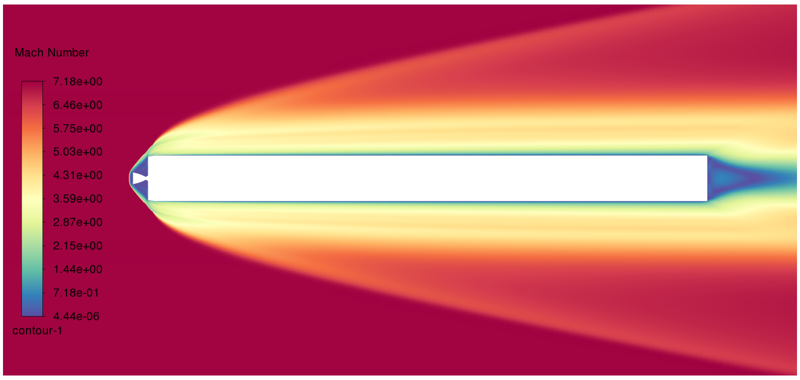

(a) Mach number.

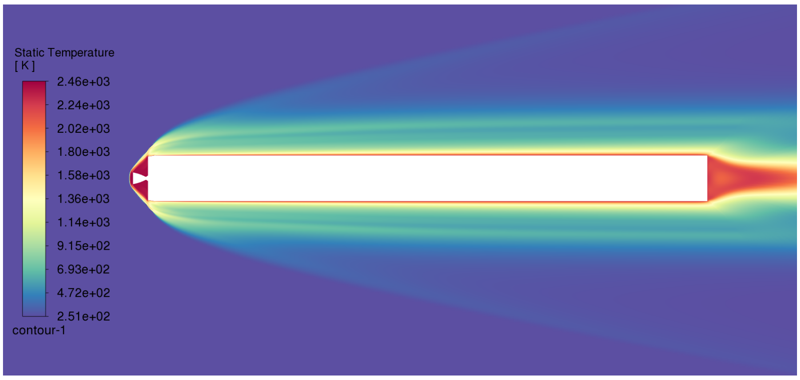

(b) Temperature.

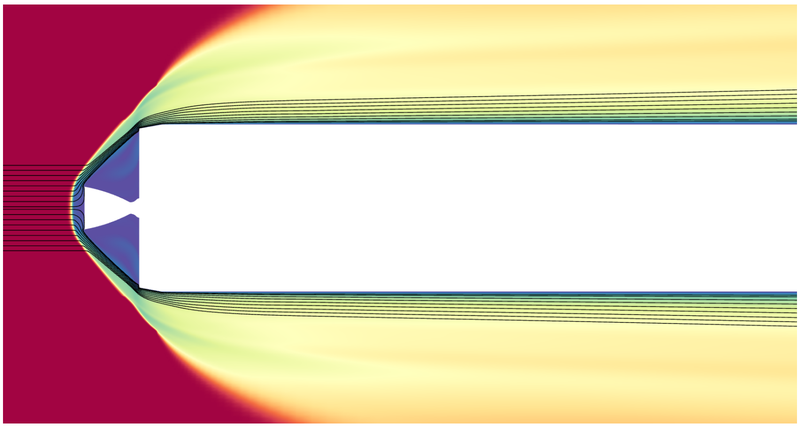

(c) Path-lines from farfield.

Figure 4.1: Flow behavior without retro-propulsion, start burn, frozen chemistry.

Figure 4.2 illustrates the flow behavior for retro-propulsion where the engine is turned on. The flow shows great resemblance with the blunt penetrating mode described in section 2.4. The hypersonic atmospheric flow meets the supersonic exhaust creating a bow shock from the freestream and a Mach disc from the exhaust. The bow shock increases the temperature of the flow while the mach disc produces a higher temperature increase which is later transported to the side of the rocket. As figure 4.2c display, there is little mixing between the exhaust and the freestream and the rocket appears to be flying in a 'bubble' of exhaust gases.

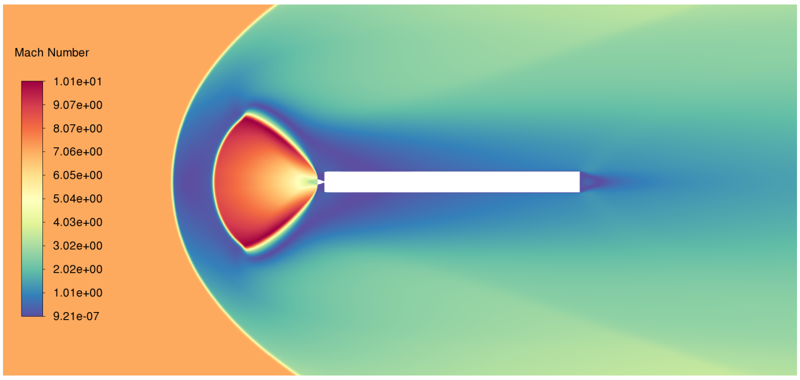

(a) Mach number.

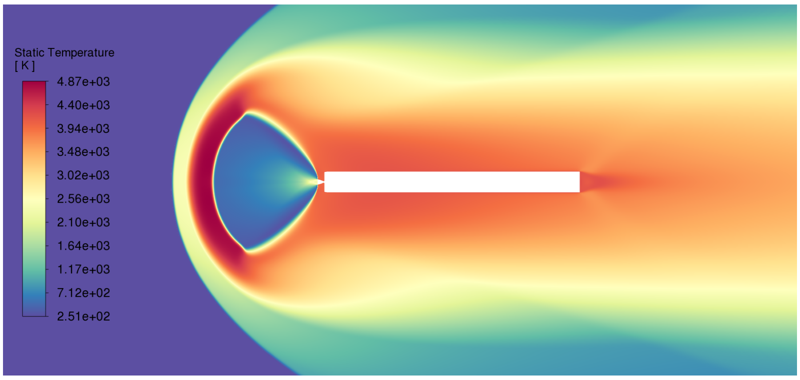

(b) Temperature.

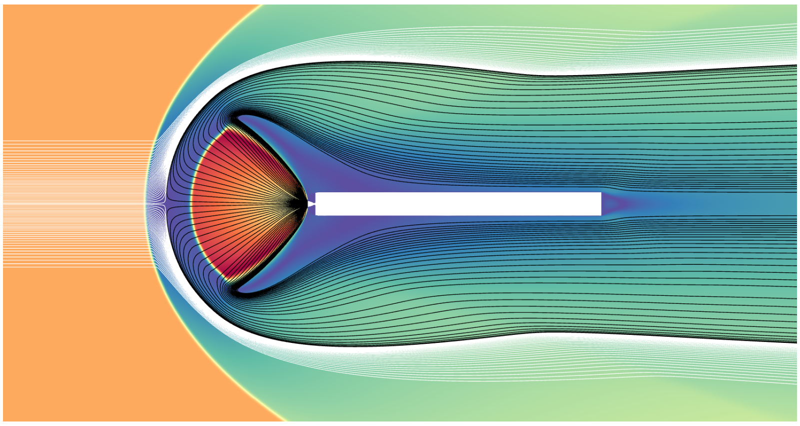

(c) Path-lines, white = farfield, black = exhaust.

Figure 4.2: Flow behavior with retro-propulsion, start burn, frozen chemistry.

4.1.1 Comparison of chemistry models

Comparison of the temperatures of the different chemistry models (calorically perfect gas, frozen chemistry, chemical equilibrium and chemical non-equilibrium) were made at the locations seen in figure 4.3. Worth to note that calorically perfect gas is modeled as only air, in other words, the exhaust is also considered to have thermodynamic- and transport properties of air. Therefore, the simulations with retro-propulsion will not have the properties of the exhaust gases which will affect the temperatures, pressures, and size of the plume. As a consequence the calorically perfect gas model of air will only be used as a comparison of trends with the rest of the models instead of analyzing their absolute values. Contour plots of the results can be seen in appendix A.4.2 while figure 4.3 shows where the data presented in figure 4.4 and 4.5 is taken from.

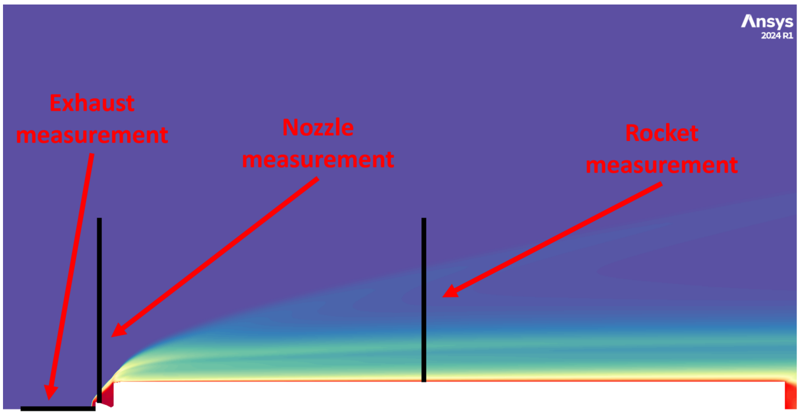

(a) Measurement lines for simulations without retro-propulsion.

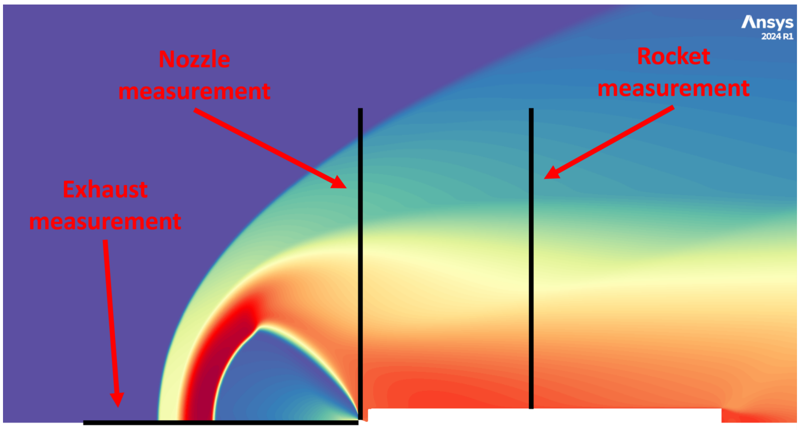

(b) Measurement lines for simulations with retro-propulsion.

Figure 4.3: Positions of measurements for simulations on nozzle and rocket side.

The comparison between chemical models for start burn without retro-propulsion can be seen in figures 4.4a, 4.4c and 4.4e. The results show that calorically perfect gas, close to the walls, deviates significantly at all three measurements resulting in temperatures several hundreds of degrees higher than the other chemical models. One can also note that frozen chemistry and chemical non-equilibrium show nearly identical results for all measurements while chemical equilibrium result in approximately 200 K lower. The reaction species for start burn, seen in figure A.2, show significantly higher mass fraction of species from reactions compared to chemical non-equilibrium. The placement of the shock waves differs slightly between the models, with the most notable being calorically perfect gas which places the shockwave approximately 0.5 m further upstream. The other models however, estimate the placement of the shock wave in approximately the same location.

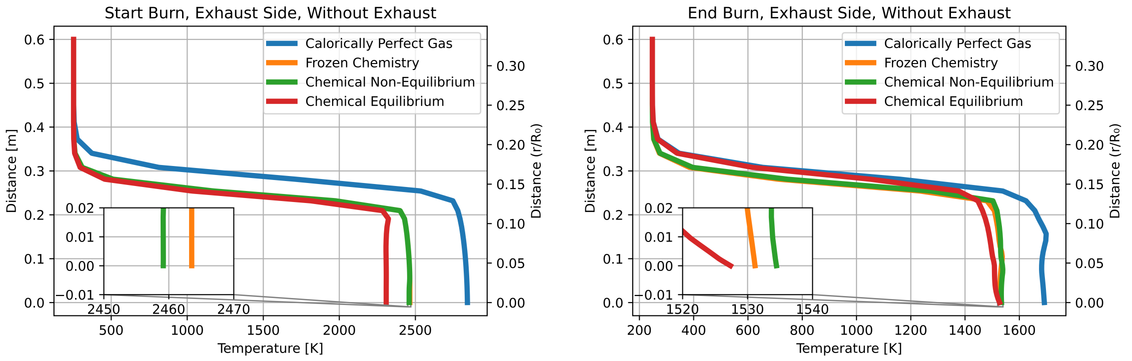

(a) Start burn at exhaust measurement. **(b)** End burn at exhaust measurement.

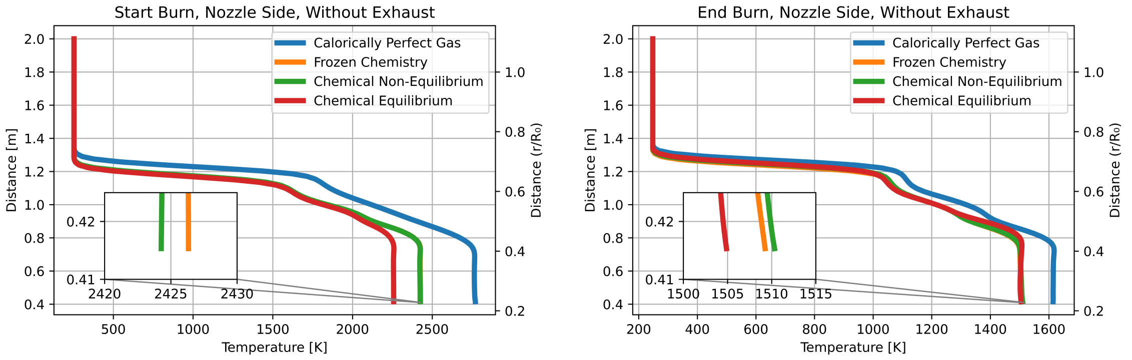

(c) Start burn at nozzle measurement. **(d)** End burn at nozzle measurement.

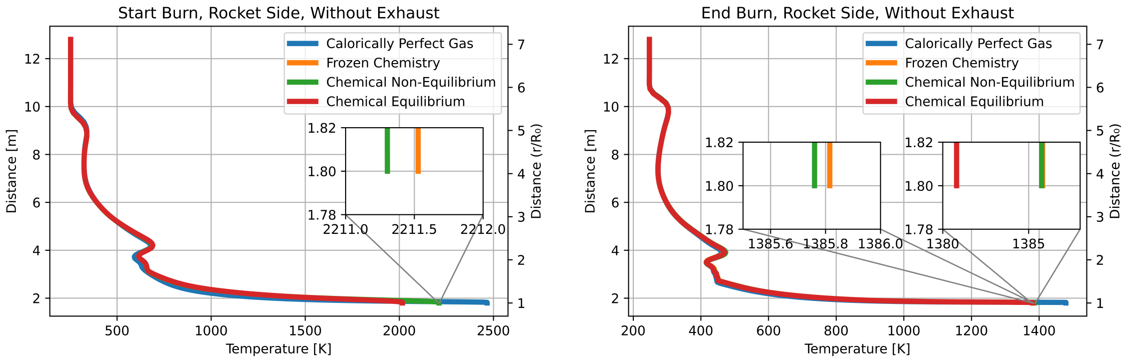

(e) Start burn at rocket measurement. **(f)** End burn at rocket measurement.

Figure 4.4: Comparison of chemistry models without retro-propulsion, r is radius from symmetry line and R_0 is rocket body radius.

The comparison between chemical models for end burn without retro-propulsion can be seen in figures 4.4b, 4.4d and 4.4f. The results conclude, just as for start burn, that calorically perfect gas estimates a significantly higher temperature compared to the other models. A major difference for end burn, compared to start burn, is that frozen chemistry, equilibrium and non-equilibrium result in very similar temperature, specially near the walls where the variation is only a couple degrees. The difference in placement of shock wave between the chemical models in end burn is less than in start burn. A major difference however is that chemical equilibrium places the shock wave in line with calorically perfect gas further upstream compared to frozen chemistry and chemical non-equilibrium.

Calorically perfect gas was found to not be an accurate model for any flight conditions simulated in this report, and even for end burn without retro-propulsion (where the lowest temperatures were found), it still produced 100 to 300 K difference in temperature. The deviance of calorically perfect gas is expected since the simulation is above 800 K which is when vibrational energy gets excited and thermodynamical properties stop being constant, which is the main assumption for calorically perfect gas. The results displayed in figure 4.4 highlight a negligible difference between the chemical models frozen, equilibrium and non-equilibrium for end burn while equilibrium resulted in 200 to 300 K lower for start burn. The temperatures during end burn with no exhaust, is approximately 1500 K, which is high enough for calorically perfect gas not to be an accurate model, but not high enough for chemical reactions to take place. For start burn however, the temperatures reach close to 2500 K, high enough for dissociation of oxygen and for nitrous-oxide formation to occur, which made equilibrium deviate from frozen. The reason for equilibrium to deviate and not non-equilibrium is most likely due to the low flow timescales compared to the chemical timescales, in other words the Damköhler number is low. The flow was fast enough for reactions to not have sufficient time to react in chemical non-equilibrium making it behave similarly to frozen chemistry. Figure A.2 further enhances this hypothesis. This suggests that the chemical-equilibrium model is unlikely to provide the most accurate representation of the flow.

The reason behind the displacement of the bow shock in calorically perfect gas (seen in figure 4.4a) is a bit harder to explain. The most likely explanation is from compressible flow theory, that say that a higher Mach number will give higher density after the shock wave and therefore more mass be able to 'fit' between the shock and the nozzle placing the shock wave closer to the body. With the case of calorically perfect gas, the temperature will be overestimated, and according to ideal gas law, this will result in a lower density and will therefore displace the shock wave upstream and locate it further away from the body.

As frozen chemistry and chemical non-equilibrium yielded virtually identical results for all measurement locations for both start and end burn, frozen chemistry is deemed the most appropriate model for simulations without retro-propulsion.

The results for the simulations with retro-propulsion (seen in figure 4.5) show a larger difference between the models. The general trend is that calorically perfect gas, frozen chemistry, chemical non-equilibrium and chemical equilibrium, in this order, will result in falling temperatures. In figures 4.5a and 4.5b one can see that the size of the plume differs significantly between the start and end burn (also seen in figure A.1). A distinctive behavior noticed in the simulation at the start of the burn is that the chemical equilibrium model shows a nearly constant temperature when approaching the rocket and nozzle wall compared to the other models (figures

4.5c - 4.5f). The temperatures are also plotted in figures A.3a and A.3b as well as species in figure A.4.

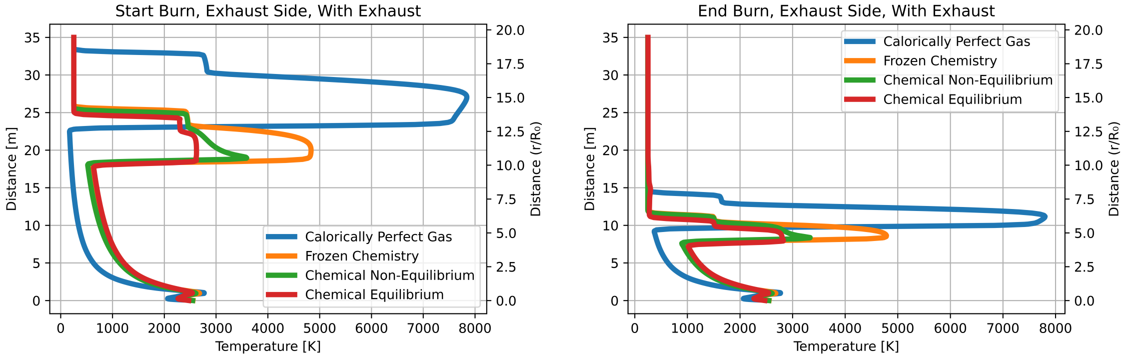

(a) Start burn at exhaust measurement. **(b)** End burn at exhaust measurement.

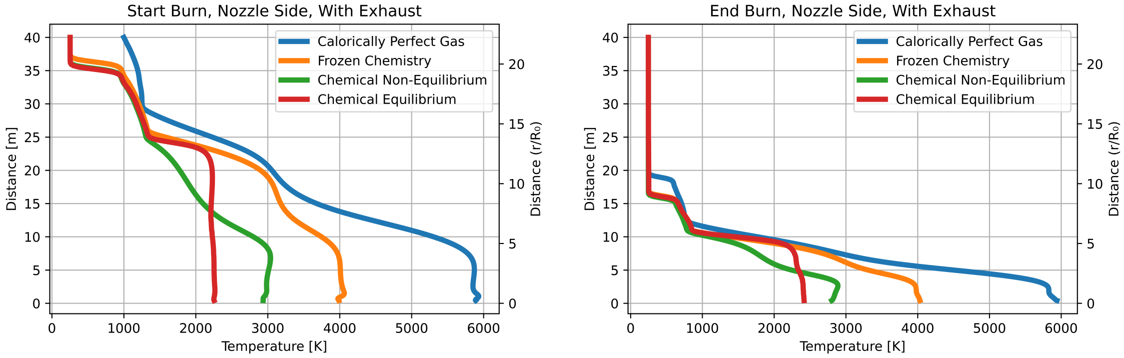

(c) Start burn at nozzle measurement. **(d)** End burn at nozzle measurement.

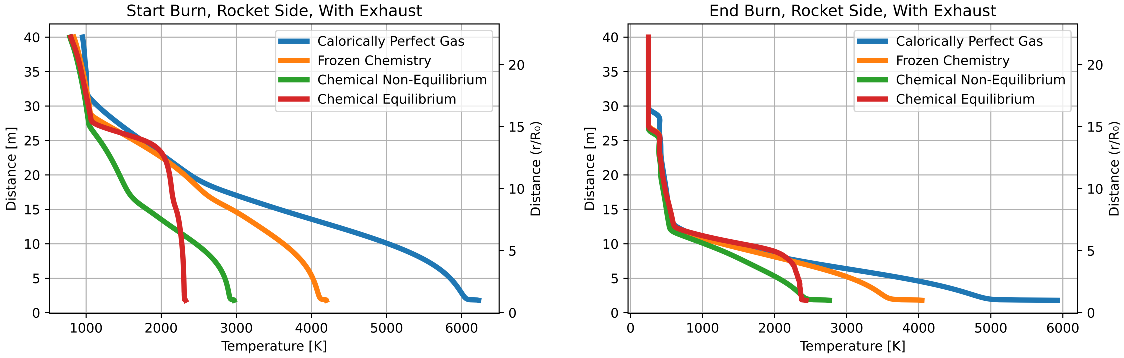

(e) Start burn at rocket measurement. **(f)** End burn at rocket measurement.

Figure 4.5: Comparison of chemistry models with retro-propulsion, r is radius from symmetry line and R_0 is rocket body radius.

The results from the exhaust measurements, figures 4.5a and 4.5b, show that the major temperature increase comes from the shock wave from the exhaust rather than the shock wave from the atmosphere. The static temperature increase over a shock wave is a function of Mach number, static temperature and the ratio of specific heat before the shock. As seen in figure A.1, for frozen chemistry the plume exhaust expands up to about Mach 10 for start burn (compared to Mach 7 in free stream) and about Mach 7 in end burn (compared to Mach 5 in free stream). The higher Mach number will result in a stronger shock wave and therefore higher temperature increase, but note that the different gas properties will differ which will also affect the shock strength. But both the temperature increase and the temperature value after the shock will be higher after the exhaust plume compared to the bow shock from the air.

The simulations from the chemical models have shown that chemistry play a significant role in retro-propulsion simulations and has major effects on the results. As all of the chemical models deviate substantially from one another, it indicates that there is significant chemical reactions in the flow, and this is also proven with the species shown in figures A.4. As all models show a temperature of over 2500 K the air from the atmosphere is hot enough to react, and the post combustion of the exhaust species is shown by the presence of reactions containing hydrogen, which is only found coming from the exhaust. The small temperature variation in the plume between frozen, equilibrium and non-equilibrium seen in figure 4.5a, as well as the small variation of species mass fraction seen in figure A.4 show that there is only a small amount of reactions ongoing in the plume itself, while the major differences, both in temperature and species, reveals that the greater part of the reactions occur in and around the shock waves.

The uniform temperature that chemical equilibrium produce for nozzle and rocket measurement, seen in figures 4.5c and 4.5d, shows that a low variation of species and flow properties on and around the nozzle walls in the radial direction. The uniform temperature and species concentration can not be found in chemical non-equilibrium as the time effects of reactions spread out the production of species making greater local variations of properties.

The plateaus in the temperature plots, specially the one found by the nozzle measurement in figures 4.5c and 4.5d, can most likely be explained by the planes between the flows. If one diverts its attention to figure 4.2c and A.3 one can see that the first plateau (nearest the nozzle) is where the flow goes from the mixing area to the exhaust flow area (exhaust flow area being the area with the black streamlines). The next plateau found at approximately 25 m from the nozzle for start burn and 10 m for end burn is the mixing plane between the exhaust (black streamlines) and the atmosphere (white streamlines). The final plateau, found at approximately 35 m for start burn and 15 m for end burn, is the bow shock from the atmosphere.

For every chemistry model that has with an increase in reactions $frozen \rightarrow non-equilibrium \rightarrow equilibrium$ the temperature keeps decreasing. This indicates that the majority of reactions are endothermic, most likely from dissociation, instead of exothermic reactions often found in post combustion.

The results from the chemistry simulations with retro-propulsion in 2D show that due to significant chemical reactions in the flow, frozen chemistry overestimates the temperature of the flow with over 1000 K making it a non accurate model for this case. As there is a big variation of velocity in the flow, from stagnated flow at 0 m/s to several kilometers per second, as well as a big variation in temperature, from 250 K to several thousand kelvin, there is a big difference in both chemical and flow timescales resulting in a great variation of Damköhler number in the different regions. This makes the equilibrium model less suitable for simulations with retro-propulsion, and the chemical non-equilibrium model, suitable when chemical and flow timescales are similar in magnitude, appear to provide the most accurate results for this specific case.

4.1.2 Heat transfer coefficient in 2D

For calculating the heat transfer such as HTC and heat flux, all simulations without retro-propulsion are run as frozen chemistry and simulations with retro-propulsion, unless specified, are simulated with chemical non-equilibrium. The adiabatic wall temperature on the nozzle contour can be seen in figure 4.6 where the left figure shows the simulation without retro-propulsion and the right with retro-propulsion. It's evident that the start of the burn achieves a lot higher temperature without retro-propulsion (around 1000 K while with retro-propulsion the temperature are of a similar magnitude where the start of the burn tops at around 2900 K while the end of the burn is around 2600 K. In contrast to without retro-propulsion the start of the burn achieved lower temperatures near the nozzle exit compared to the end of the burn during retro-propulsion.

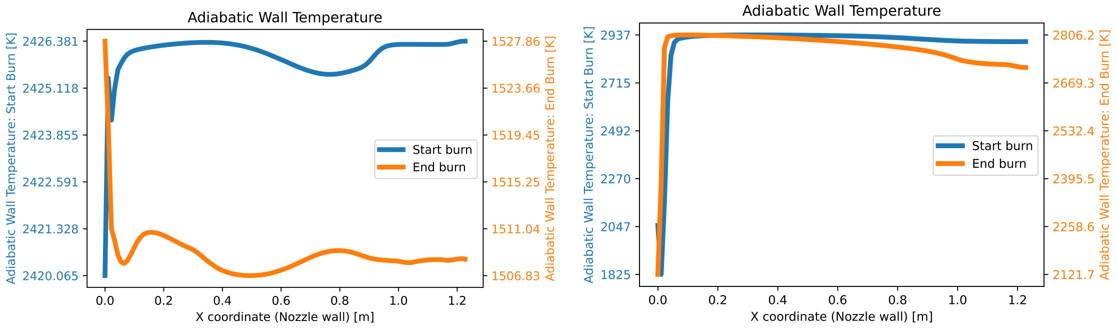

Figure 4.6: The adiabatic temperature at the nozzle without retro-propulsion with frozen chemistry model (left figure) and with retro-propulsion with chemical non-equilibrium (right figure) at the start and end of the burn.

The results from heat transfer coefficient simulations, calculated through equation 2.23, can be seen in figures 4.7 and 4.9. All simulations without retro-propulsion are run as frozen chemistry and simulations with retro-propulsion, unless specified, are simulated with chemical non-equilibrium. For simulations with retro-propulsion, only the end burn was simulated, this due to convergence issues for heat transfer at start burn.

The ΔT simulations, where the prescribed wall temperature is a profile set as an offset from the adiabatic wall temperature, show a strong temperature independence with close to identical solutions for different ΔT. For a constant temperature without retro-propulsion however, there is a slight variation between temperatures but they follow the same trend. There is also a shift of heat coefficient values where a constant temperature estimates a lower heat transfer coefficient. For simulations with retro-propulsion however (figure 4.9), the constant temperature also shows strong temperature independence and very close values to those simulated with ΔT.

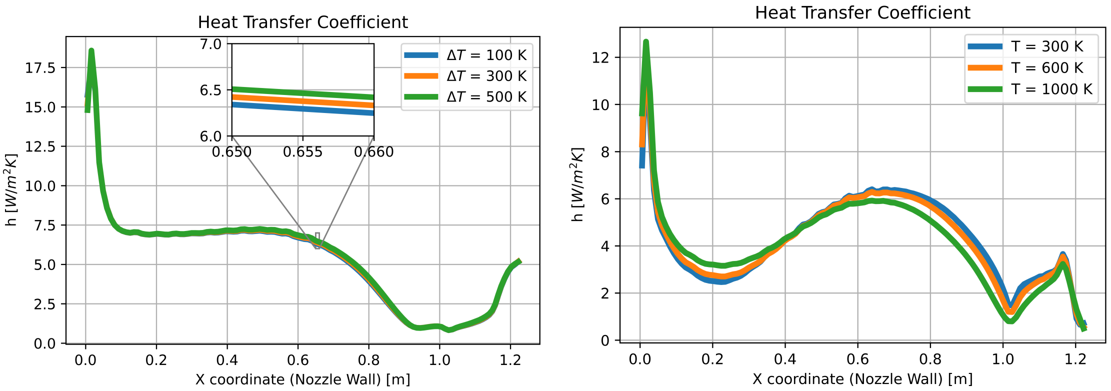

(a) Start burn with nozzle wall temperature as a profile.

(b) Start burn with nozzle wall temperature as a constant.

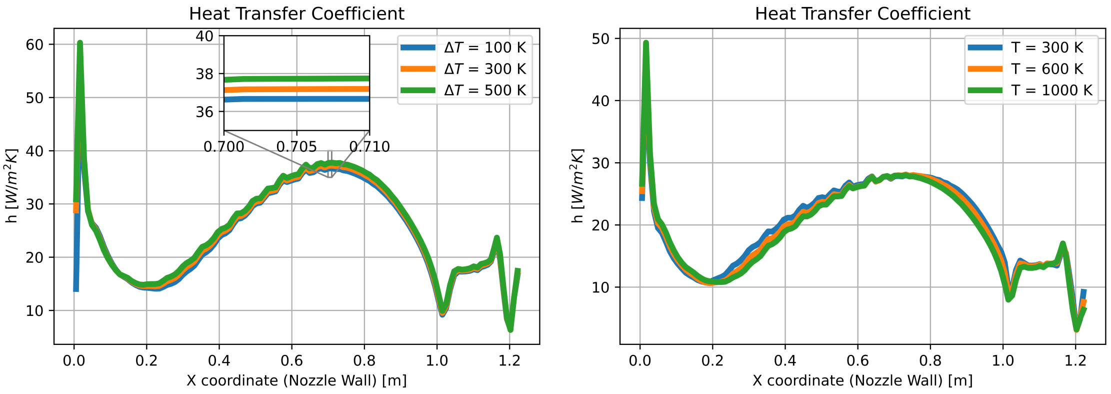

(c) End burn with nozzle wall temperature as a profile.

(d) End burn with nozzle wall temperature as a constant.

Figure 4.7: Heat transfer coefficients for 2D simulations *without* retro-propulsion. Profile values are set as a fixed difference from adiabatic wall temperature. $X = 0$ is at nozzle exit.

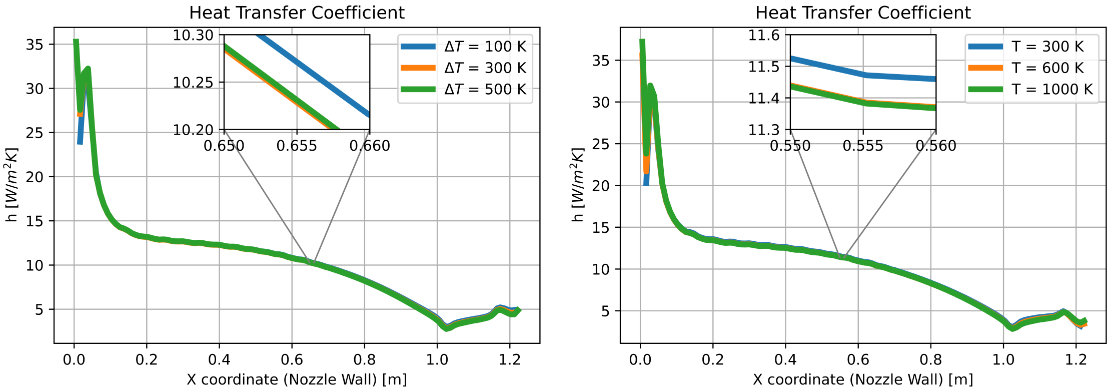

(a) End burn with nozzle wall temperature as a profile.

(b) End burn with nozzle wall temperature as a constant.

Figure 4.8: Heat transfer coefficients for 2D simulations **with** retro-propulsion. Profile values are set as a fixed difference from adiabatic wall temperature. $X = 0$ is at nozzle exit.

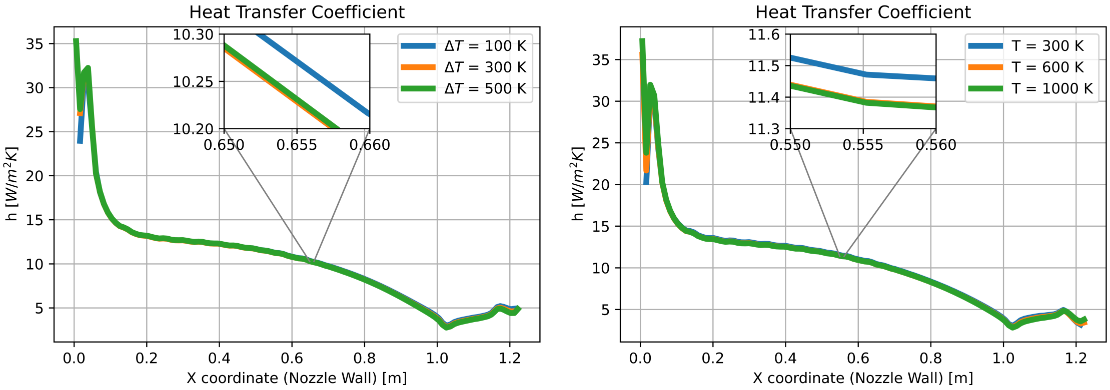

(a) End burn with nozzle wall temperature as a profile.

(b) End burn with nozzle wall temperature as a constant.

Figure 4.9: Heat transfer coefficients for 2D simulations with retro-propulsion. Profile values are set as a fixed difference from adiabatic wall temperature. $X = 0$ is at nozzle exit.

HTC, in theory, should be dependent on flow- and geometric properties and be independent of wall temperature. However, in some cases, there is a chance that the wall temperature will affect the behaviour or chemical reactions within the flow. The simulations with a profile (ΔT) in figures 4.7a, 4.7c and 4.9a, show that a change in wall temperature will not affect the HTC for either with or without retro-propulsion, which is in line with theory. With a constant wall temperature, however, there is a variation between set temperatures. The most likely reason is due to transport of properties in the boundary layer. When a constant temperature is set, the temperature of the flow near the wall will be transported in the boundary layer downstream. This transport will affect the temperature, and therefore the heat flux and HTC, downstream causing a variation between set wall temperatures. When the wall temperature is a profile, the transport of temperature is taken into consideration, and the temperature more carefully follows the 'natural' temperature of the flow, as it is calculated from the adiabatic wall temperature. This hypothesis is further supported by the fact that the HTC measured at constant temperatures are well aligned near the exit of the nozzle, where it is has not yet been affected by boundary conditions upstream, and the difference become more pronounced further downstream.

Which of the measurement methods is more accurate, HTC from constant wall temperature or HTC from a profile, is also uncertain. Before the launch of the rocket, the nozzle temperature will start at a constant temperature, but as the flight and flight properties change the thermal loads and therefore the temperature of the nozzle will change. This means that, with the engines shut off, the temperature will most likely go towards the adiabatic wall temperature (with a profile), but due to thermal inertia in the material, this will occur over time. As the engines are ignited, coolant will flow through the nozzle cooling the outside, making the nozzle most likely go towards a more of a constant temperature once more, and again due to inertia, this will occur over time. The reality is therefore most likely somewhere in between the two cases. The chosen method, deemed more useful, is a HTC calculated from a profile as this will produce temperature independent values and more conservative estimates of HTC compared to constant temperature.

It has been showed that the choice of chemical model has a significant effect on temperature in the flow, however, its affect on the flow behavior is uncertain. Since HTC is temperature independent, a study was made to see if simulations with retro-propulsion differed between chemical non-equilibrium and frozen chemistry. If they were to display similar results, the models for HTC simulations in 3D could be reduced to save computational costs. The results, seen in figure 4.10a, show that HTC with frozen chemistry during retro-propulsion is, as chemical non-equilibrium, also temperature independent. Comparison with chemical non-equilibrium can be seen in figure 4.10b, which shows that there is a noticeable difference, however only with a magnitude of approximately 1 to $1.5\,\mathrm{W/(m^2\,K)}$. Chemical non-equilibrium is slightly more conservative in a design perspective compared to frozen chemistry.

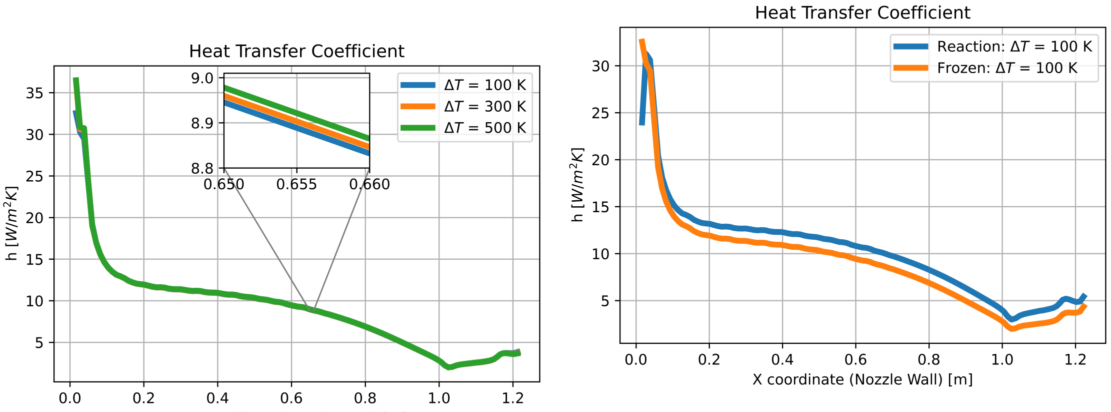

(a) End burn, frozen chemistry, with nozzle wall temperature as a profile.

(b) End burn, comparison between chemical non-equilibrium and frozen chemistry.

Figure 4.10: Heat transfer coefficients for 2D simulations during retro.propulsion, frozen chemistry. Profile values are set as a fixed difference from adiabatic wall temperature. $X = 0$ is at nozzle exit.

The results in figure 4.10a are in line with the earlier findings that HTC is temperature independent if a profile wall temperature (ΔT) is used. There is however a difference in HTC between chemical non-equilibrium and frozen chemistry. HTC should, according to earlier findings, only be dependent of the flow and geometry, and as the geometry is identical, the conclusion is that the different chemical models resulted in a slightly different flow around the nozzle. However, since the difference is small, mostly below 10%, frozen chemistry is considered a good enough approximation for heat transfer simulations, if HTC is to be calculated, due to drastic decrease in computational cost. But it should be kept in mind that for future 3D simulations when the HTC is calculated with frozen chemistry, it will probably give a small deviation compared to what a reacting flow would result in. Another thing worth to note is that frozen chemistry cannot be used if heat transfer ($q = h\Delta T$ [W/m^2]) is to be calculated since it will produce a major difference in ΔT compared to chemical non-equilibrium.

4.1.3 Chemical model reduction

As mentioned in the section 3.6.3, the chemical model needed to be reduced from 24-species into 13-species in order to decrease the RAM-usage of the model in 3D. The results from the investigation of flow temperature between full 24-species and reduced 13-species non-equilibrium chemical model can be seen in figure 4.11. The reduced model follow the full model very closely with little to no difference in temperature showing that the reduced model successfully captures the behavior of the full model.

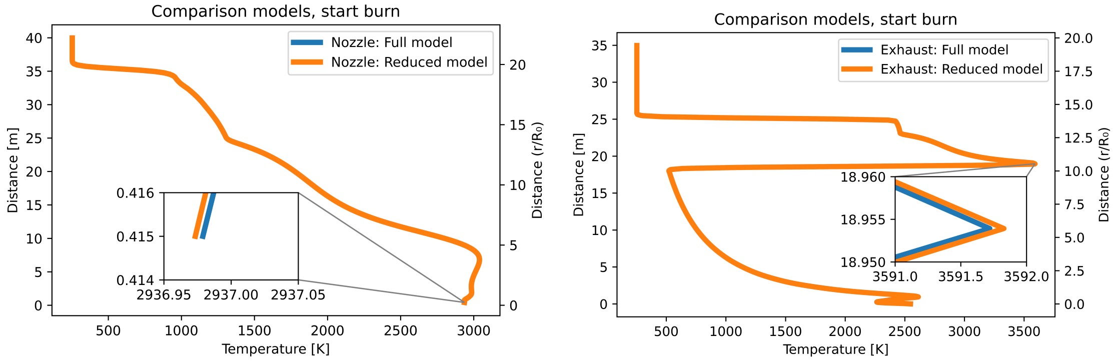

(a) Start burn nozzle measurement. **(b)** Start burn exhaust measurement.

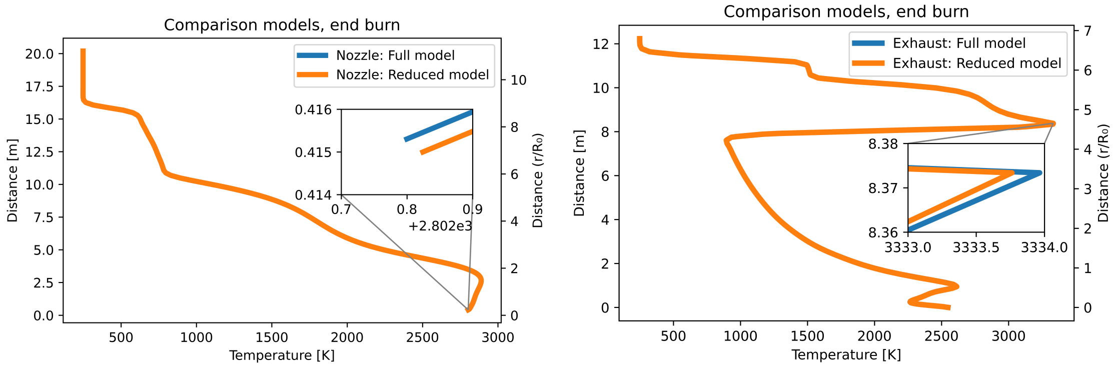

(c) End burn nozzle measurement. **(d)** End burn exhaust measurement.

Figure 4.11: Comparison full 24-species non-equilibrium model and reduced 13-species non-equilibrium model. Measurements taken at location displayed in figure 4.3a and 4.3b.

4.2 3D simulations without retro-propulsion

A contour plot can be seen in figure 4.12 at the end of the burn without retro-propulsion. The results show a similar shock behavior as in 2D with a strong bow shock across the entire front of the rocket where the 3D simulations places the shock slightly further away form the nozzle. Effects from multiple nozzles is seen as the flow accelerates between the nozzles as the flow bends up and the temperature around the central nozzle is similar to the temperature found in the 2D simulations.

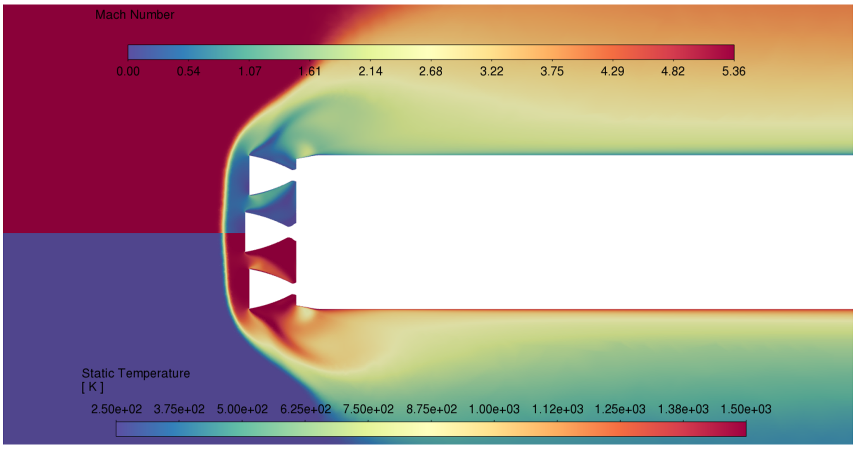

Figure 4.12: Mach number and temperature without retro-propulsion, end burn.

Table 4.1 shows a summary of the results for simulations without retro-propulsion, more details in the following sections. The general trend is that start burn results in a higher wall temperature (approximately 900 K) on all nozzles, however, start burn has a lower maximum heat transfer coefficient and heat flux. The central nozzle has a higher mean temperature compared to the other nozzles, but has a lower maximum temperature. Note that here and moving forward the nozzles may be named in the following way according to figure 3.2: central nozzle (9), activated side nozzle (1, 5), diagonal nozzle (2, 4, 6, 8) and unactivated/non-activated side nozzle (3, 7). All plots will also be along the XZ-plane, in other words cutting through all the active nozzles (1, 9, 5).

Table 4.1: Temperature and heat transfer coefficient (HTC) data for simulations without retro-propulsion.

Mean temperature [K]	Central	Activated side	Diagonal	Unactivated side
Start burn	2458	2419	2422	2420
End burn	1523	1492	1495	1493
Max temperature [K]	Central	Activated side	Diagonal	Unactivated side
Start burn	2460	2473	2470	2471
End burn	1524	1532	1529	1531
Max HTC [W/(m^2 K)]	Central	Activated side	Diagonal	Unactivated side
Start burn	29.4	69.0	72.6	71.5
End burn	80.0	196.9	154.3	157.6
Max heat flux [kW/m^2]	Central	Activated side	Diagonal	Unactivated side
Start burn	44.6	102.4	104.8	102.6
End burn	105.0	197.3	145.1	198.3

4.2.1 Start burn

The results from the simulation at the start of the reentry burn without retro-propulsion are shown below in figure 4.13. From figure 4.13a one can see that the central nozzle has a fairly constant temperature and that the other nozzles has a larger temperature variation between 2300 and 2470 K with a maximum near the throat. The streamlines in figure 4.13b show significant flow of air through the nozzle cluster with recirculation between the outer nozzles and the central nozzle. As illustrated in figure 4.13c the highest heat transfer coefficient (HTC) can be found at the throat of the outer nozzles as well as the base plate with a slight variation between the outer nozzles. The maximum HTC is approximately 60 W/(m^2 K) at the throat and larger areas where the HTC is around 20 W/(m^2 K) is found on the outer nozzles at the surfaces facing the central nozzle. Similarly there is an increase in the Nusselt number near the throat compared to the rest of the nozzle which indicates that a larger part of the heat transfer at that place is due to convection as can be seen in figure 4.13d. From figure 4.13e it is evident that the highest pressure (approximately 2 kPa) is in the same location as the localized hot spot and maximum heat transfer coefficient where the flow stagnates when it recirculates.

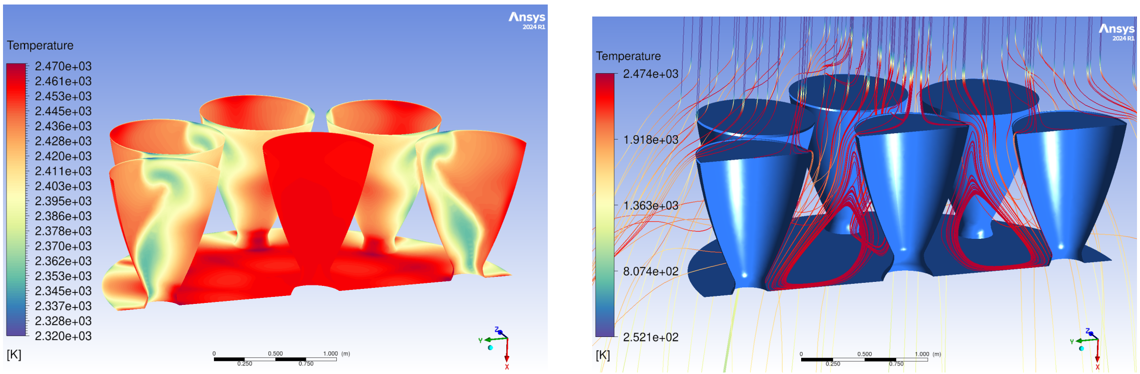

(a) Adiabatic temperature distribution. **(b)** Temperature streamlines .

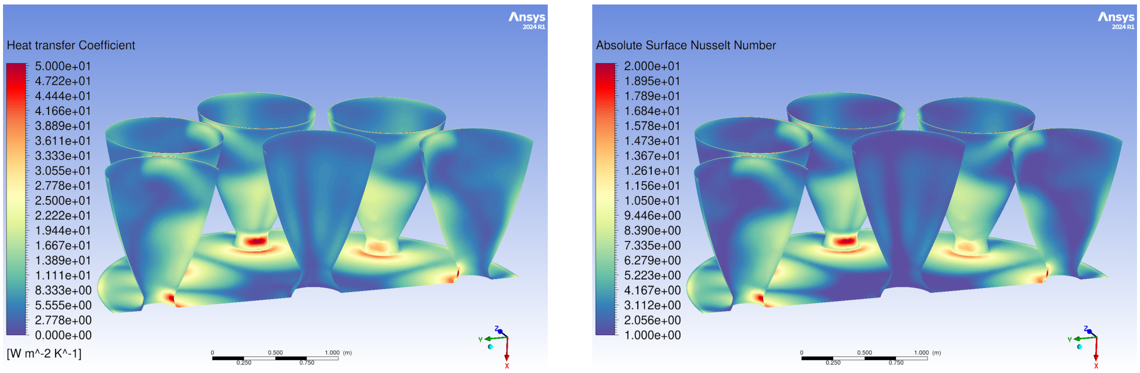

(c) Heat transfer coefficient, calculated from $\Delta T = 100$K. **(d)** Surface Nusselt number, calculated from $\Delta T = 100$K.

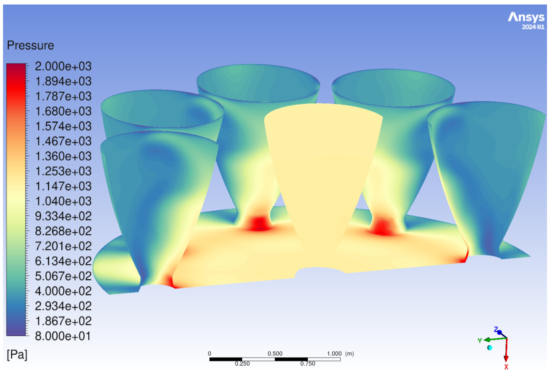

(e) Pressures achieved at the walls, calculated from $\Delta T = 100$K.

Figure 4.13: 3D analysis of start burn without retro-propulsion.

If one looks closely at figure 4.13c, it's clear that there is a slight difference between the HTC between nozzle 3 and 4 (the unactivated side nozzle which is the outer one at the middle and the one beside it to the right, see figure 4.17a) where nozzle 3 display slightly higher values at the throat compared to nozzle 4. Since the geometry, without retro-propulsion is entirely symmetric around all of the nozzles, in theory there should not be any difference in the results. The difference is believed to be due to the placement of the symmetry plane cutting through nozzle 3. The symmetry plane places stronger restrictions on the flow around the nozzle and is likely to result in the higher HTC in that location. If one instead looks at the streamlines in figure 4.13b, there is not as clear of a stagnation point on the central nozzle as it has more of a uniform pressure distribution which is the most probable reason for its constant adiabatic wall temperature.

The results for the heat flux simulation with a constant temperature of 300 K for the nozzles and base plate is displayed in figure 4.14. The heat flux is locally calculated to be 100 kW/m^2 on the nozzle and slightly higher on the base plate at the start of the burn. The majority of heat transfer is located at the inside of the nozzle while the outside is substantially lower. The region between the central nozzle and the outer nozzles are also the location where a lot of recirculation can be observed (figure 4.13b).

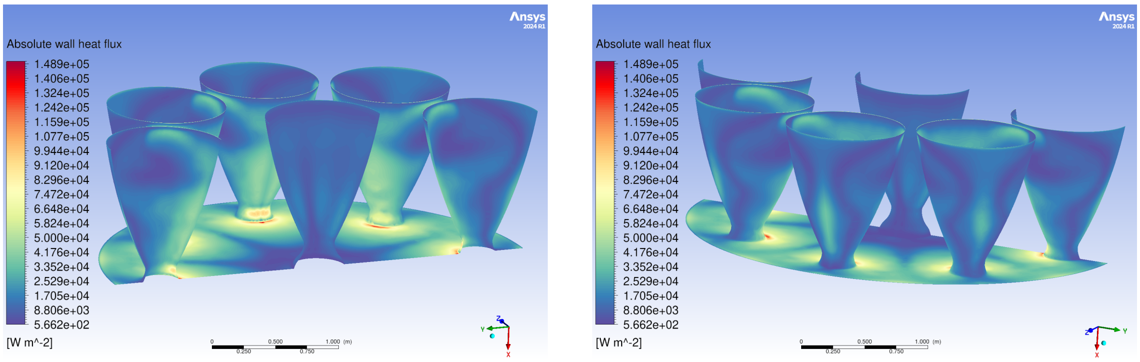

(a) Inside view of the nozzles. **(b)** Outside view of the nozzles.

Figure 4.14: 3D analysis of the absolute value of the heat flux at start burn, calculated with constant wall temperature of 300 K.

The heat flux is visibly higher locally for the base plate compared to the nozzle, which is surprising as it is in contradiction with the results from the HTC simulations which indicated higher heat transfers on the nozzle. As the adiabatic wall temperature on the nozzle and the base plate, in the area of the throat, are similar in magnitude, one would expect that the heat transfer, defined as $q = h(T_{aw} - T_w)$, would be higher where the HTC is higher. This indicates that the set wall temperature of 300 K might be affecting the behavior and characteristics of the flow. There is also less of a difference between the nozzles in the heat flux simulations compared to the HTC simulations where the results on the base plates are visually identical while there is a slight difference between the throat of the nozzles.

4.2.2 End burn

As illustrated in figure 4.15, end burn display similar behavior and trends as start burn with constant (but significantly lower) temperature on the central nozzle and a variation between 1450 and 1530 K for the outer nozzles. The area with the highest heat transfer coefficient can, as in start burn, be found at the throat of the outer nozzles and base plate but with a value of 150 W/(m^2 K), compared to 60 W/(m^2 K) for start burn. The pressure for end burn is noticeably higher with local pressures of 12 kPa at the stagnation region near the throats.

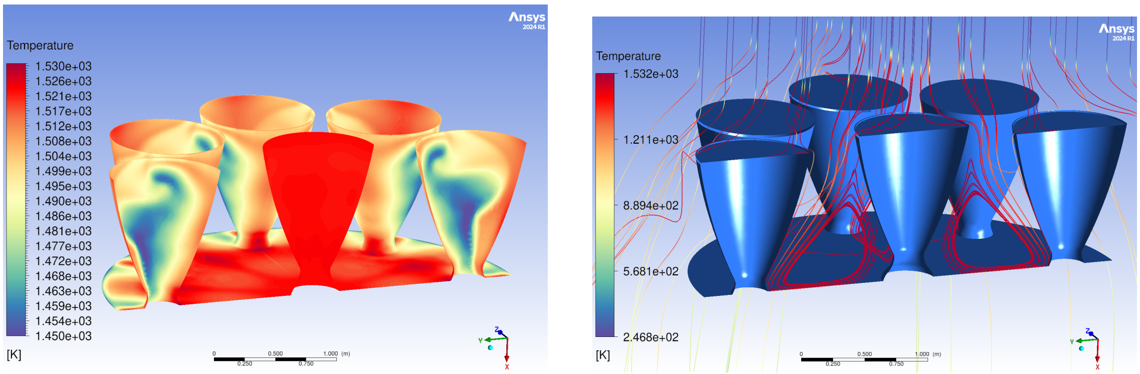

(a) Adiabatic temperature distribution. **(b)** Temperature streamlines .

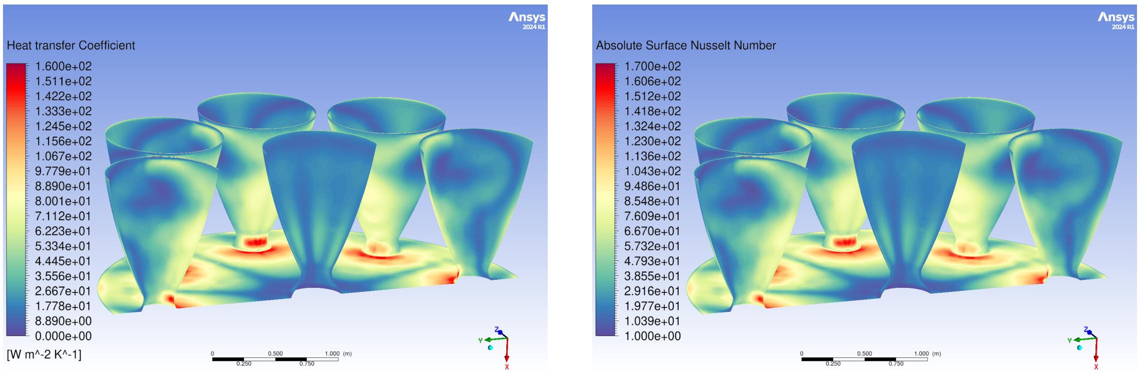

(c) Heat transfer coefficient, calculated from $\Delta T = 100$K. **(d)** Surface Nusselt number, calculated from $\Delta T = 100$K.

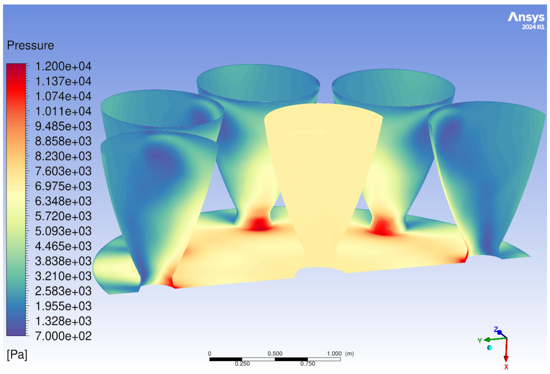

(e) Pressures on the walls, calculated from $\Delta T = 100$K.

Figure 4.15: 3D analysis of end burn without retro-propulsion.

The behaviour for end burn is very similar to that found at the start burn, but with different magnitudes. The temperature plots appear almost identical, except that the end burn temperature is approximately 1000 K lower. The HTC distribution is also very similar, with higher values near nozzle 3, which has the symmetry plane going through it, and lower for nozzle 4. The HTC is approximately 3 times higher for end burn compared to start burn, which is most likely due to the higher atmospheric pressures (5 to 6 times the pressure on the nozzle walls) and density. As the pressures increase, the flow is able to not only transfer the heat to the surface better, but also carry more heat and energy per volume gas.

The same simulation was made for the heat flux, calculated from a constant wall temperature of 300 K but for end burn. In figures 4.16, local heat fluxes of 200 kW/m^2 can be observed at the throat of the nozzle. Similar to start burn, the majority of heat transfer is located on the outer nozzles on the sides facing inwards toward the direction of the central nozzle.

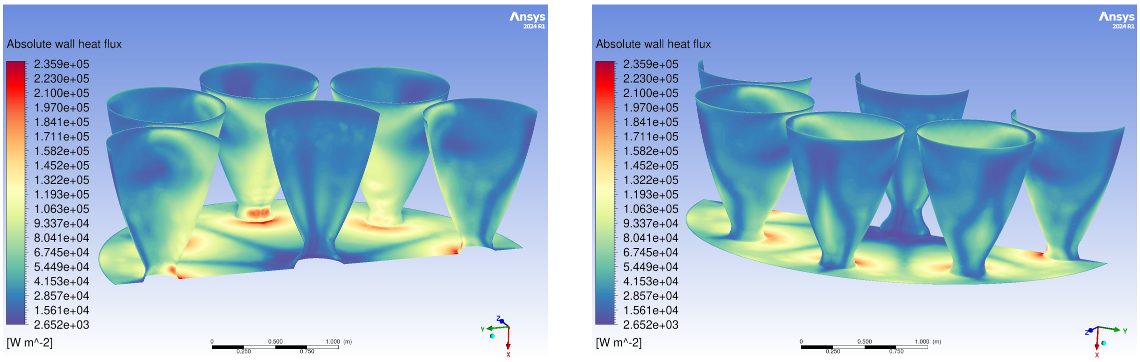

(a) Inside view of the nozzles.

(b) Outside view of the nozzles.

Figure 4.16: 3D analysis of the heat flux at end burn, calculated with constant wall temperature of 300 K.

The heat flux behaviour, not surprisingly is also similar to start burn and was found to be approximately 50% higher, even though the HTC is 3 times higher. This is due to the lower Mach numbers resulting in a lower ΔT at the end burn. The heat transfer for the end of the burn at nozzle 3, was similar in magnitude compared to the base plate, a difference found from what is seen in start burn. Another distinction compared to start burn is a greater variation of heat flux between nozzle 3 and 4.

4.3 3D simulations with retro-propulsion

A summarize of the results with retro-propulsion can be seen in table 4.2. The mean temperature is similar for both start and end burn where end burn is approximately 2800 to 3000 K for all nozzles and start burn is approximately 100 to 250 K higher. At the start of the burn, all of the nozzles are subjected to a maximum HTC of 132 to 187 W/(m^2 K) while for end burn there is a larger spread ranging from 70 to 158 W/(m^2 K). For heat flux, the most exposed nozzle is the center nozzle at the end of the burn, while the second-most exposed is the diagonal nozzle during start burn.

Table 4.2: Temperature and heat transfer coefficient (HTC) data for simulations with retro-propulsion.

Mean temperature [K]	Central	Activated side	Diagonal	Unactivated side
Start burn	3132	3084	3094	3194
End burn	3013	2838	2925	2944
Max temperature [K]	Central	Activated side	Diagonal	Unactivated side
Start burn	3409	3351	3465	3388
End burn	3407	3228	3220	3291
Max HTC [W/(m^2 K)]	Central	Activated side	Diagonal	Unactivated side
Start burn	162.9	186.6	159.1	131.7
End burn	157.7	133.2	70.3	110.0
Max heat flux [kW/m^2]	Central	Activated side	Diagonal	Unactivated side
Start burn	317.6	190.5	404.4	355.1
End burn	471.8	131.8	179.4	282.1

The plume structure for end burn during retro-propulsion can be seen in figure 4.17, with the XY-plane in figure 4.17b and XZ-plane in figure 4.17c. For the XZ-plane view the plume widens and then contracts as a shock is formed and peak Mach number is found just before the shock. The wide exhaust plume is due to the absence of another plume at that plane making it possible for the exhaust to expand past the nozzles. While for the XY-plane view, the plume is more compact and there is plume-plume interactions between the engines. The expansion goes on to higher mach numbers and therefore a stronger shock.

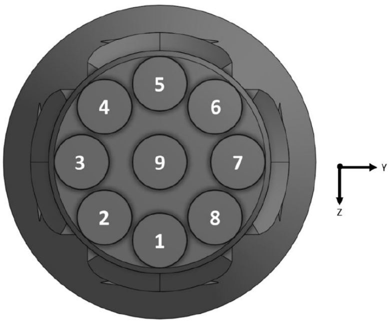

(a) The active side nozzles 5-9-1 is seen in YZ-plane and non-active side nozzles 3-9-7 seen in XY-plane [24].

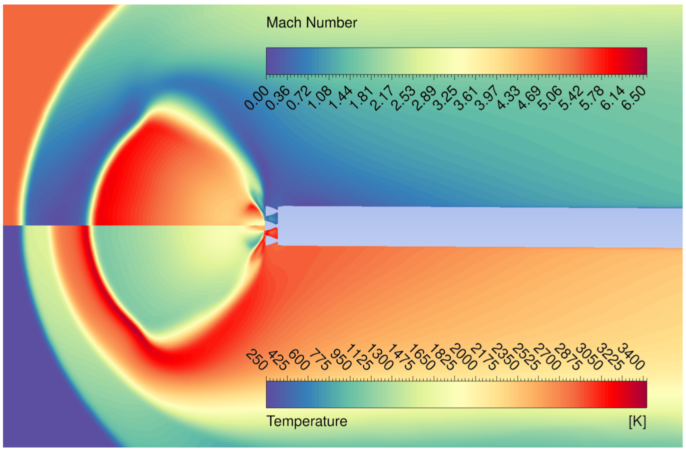

(b) Mach numer (upper) and temperature (lower). View from XY-plane.

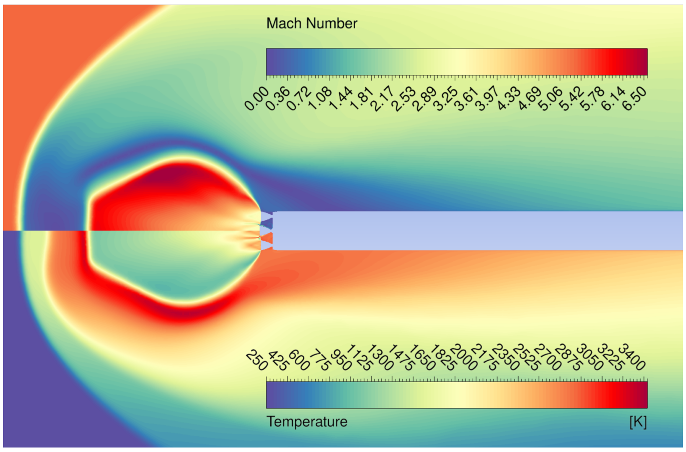

(c) Mach numer (upper) and temperature (lower). View from XZ-plane.

Figure 4.17: Plume structure for 3D simulation, end burn.

From figure 4.18 the energy created or used in the reactions is shown. It's noted that there is only a very small heat source in the plume, located shortly after the nozzle exit, indicating limited post combustion. This reaction is most likely caused by the steep flow gradients caused by expansion fans and oblique shocks. There is however, specially for end burn, a significant heat source located behind the bow shock from the atmosphear. A major region with heat sink is found after the Mach disk, indicating endothermic reactions, suggesting significant dissociation. In between the heat sink and heat source after the shock wave, is the location of the mixing plane between the flow from the freestream and the flow from the exhaust. This means that it is probable that the heat source is a result of the newly dissociated exhaust, coming from a oxygen-deficient region and combusting as it meets oxygen coming from the freestream.

The total heat of reaction, both heat source and heat sink, are considerably higher for end burn compared to start burn. The cause of the difference can be explained due to the non-equilibrium chemical model used and the physics at role at different altitudes. As explained in section 2.7 and figure 2.3, at higher atmospheres and velocities, the distance between the molecules increase resulting in decreased likelihood of collision between molecules and therefore of a reaction. This means that the higher altitudes and higher velocities found in start burn will result in slower reactions and the chemical state being further from equilibrium. Another result of the low pressures and densities at start burn is the fact that there are fewer species per volume, effectively resulting in fewer species able to react.

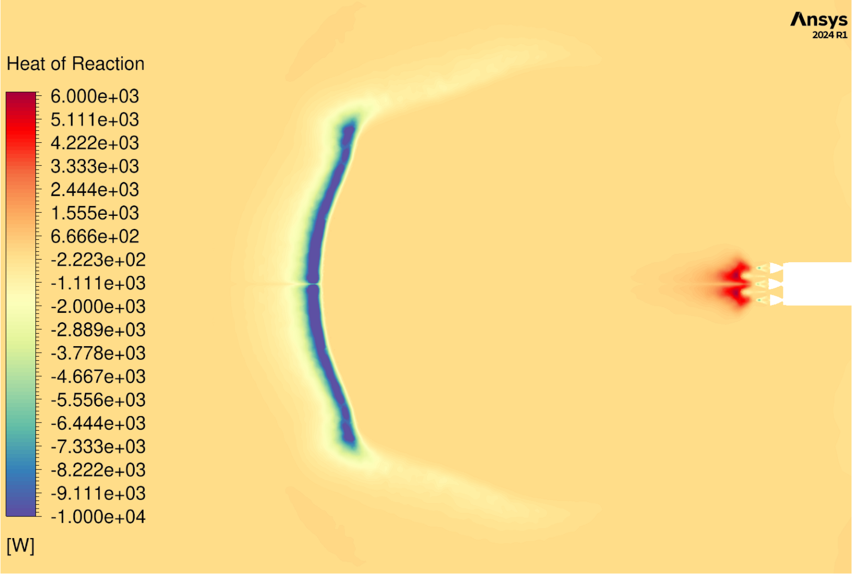

(a) Heat of reactions, start burn.

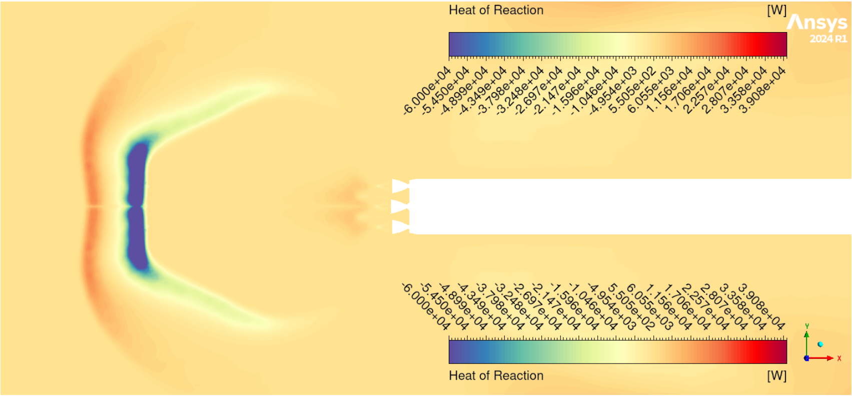

(b) Heat of reactions, end burn.

Figure 4.18: Heat of reaction in plume and shock wave. Note the difference of value in the color bars.

4.3.1 Start of the burn

In figure 4.19, the adiabatic temperature, HTC and streamlines from the exhaust is shown. Note that these simulations are run with frozen chemistry, resulting in unrealistically high temperatures. It can be noted that the side facing outward on the activated side nozzles (5 and 9) achieve the highest temperatures of over 4100 K. These hot spots are due to the exhaust expanding from the nozzle exit and then experience a temperature increase after the shock. This high temperature gas will then be transported downwards and circulate around the outer nozzles which will heat the nozzle walls as seen in figure 4.20. For the nozzle walls facing inward, the exhaust from the nozzles will expand into the other nozzles and circulate down into the cluster. For this frozen chemistry simulation, the temperature of the exhaust from the nozzle (figure 4.19c) is lower than the exhaust recirculating after the shockwave (figure 4.20a), effectively resulting in the recirculation inside the nozzle cluster cooling the walls facing inwards compared to the outside. The HTC shown in figure 4.19b indicates that the highest HTC is located near the edge of the unactivated outer nozzles as well as the center nozzle. These high value regions can be explained by figures 4.19c and 4.19d. It's clear that the exhaust from the activated side nozzles are expanding into the edge of both the center nozzle but also the side nozzles next to it. These high velocity exhausts hits the nozzle walls and results in the regions with high heat transfer coefficient. It's also evident that the exhaust is mainly coming from the activated side nozzles as the center nozzle is mainly expanding upwards and away from the other nozzles.

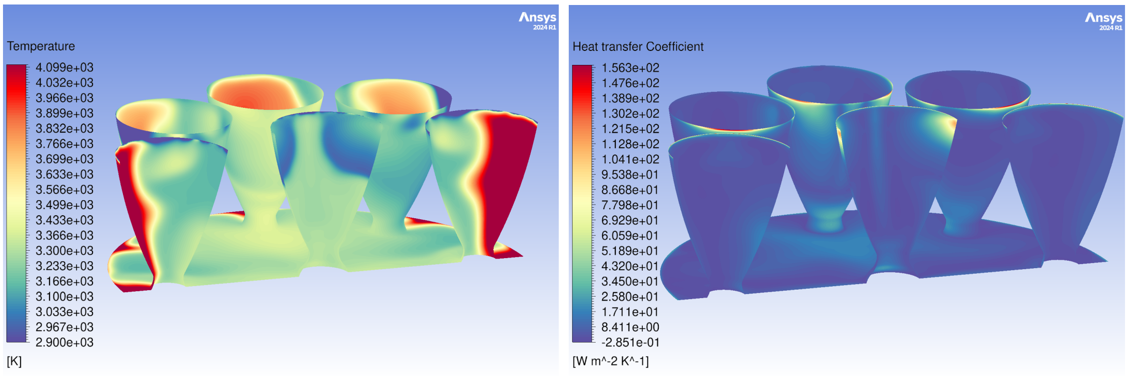

(a) Adiabatic nozzle wall temperature, frozen chemistry.

(b) Heat transfer coefficient.

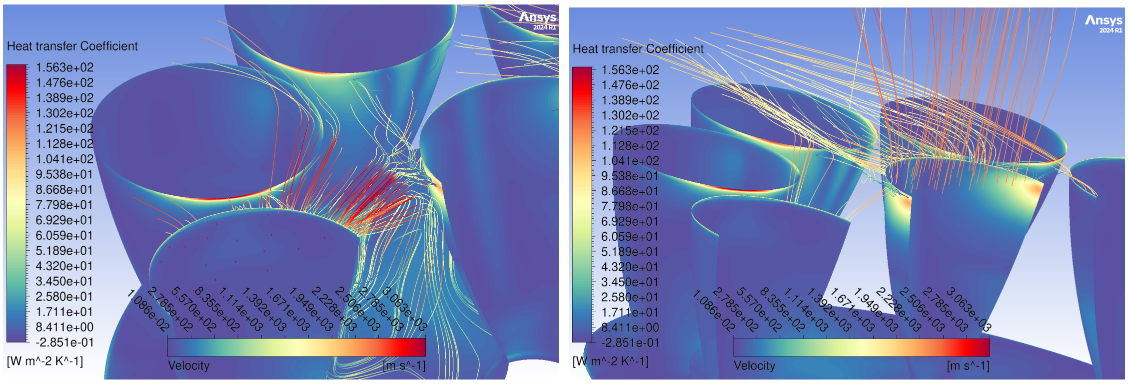

(c) Exhaust streamlines from side nozzle.

(d) Exhaust streamlines from center nozzle.

Figure 4.19: Adiabatic temperature and heat transfer coefficient from start burn simulations, frozen chemistry. Heat transfer coefficient calculated with wall temperature as a profile ($dT = 100\,\mathrm{K}$).

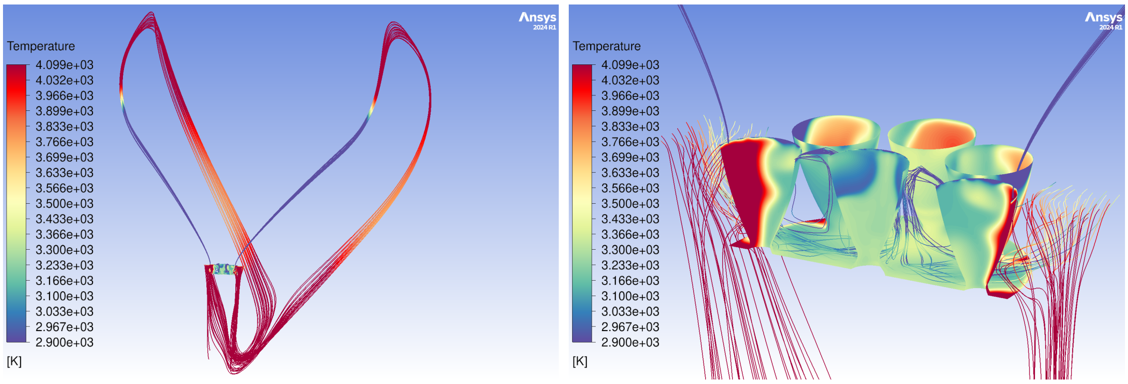

(a) The exhaust streamlines from the side nozzles, frozen chemistry.

(b) A zoom in on the nozzles to showcase the streamlines coming out of the nozzles and the ones heating up the outside of the nozzles, frozen chemistry.

Figure 4.20: Adiabatic temperature streamlines from the exhaust of the side nozzles.

The adiabatic temperature for the non-equilibrium simulation is show below in figure 4.21, it's noted that the temperature reaches a maximum temperature of around 3500 K which is significantly lower than the 4300 K achieved in the frozen chemistry model. The largest differences are seen at the activated side nozzles on the side facing outward where the temperatures are around 1000 K lower with a chemical non-equilibrium model compared to frozen chemistry. This can be explained by examining the streamlines from the exhaust in figure 4.21c and 4.21d respectively. Similar to the frozen chemistry simulation the temperature increases after the shock, but compared to the frozen model it's noted that the temperature doesn't reach as high of a temperature as well as decreases drastically in the recirculation zone. This results in the flow at the outward facing side of the nozzles reaching a temperature of around 3000 K while in the frozen chemistry model the temperature results in over 4000 K. The difference is most likely due to the endothermic reactions in the non-equilibrium model, taking place after the shockwave effectively reducing the temperature compared to the frozen chemistry model. If the temperatures of the center nozzle and the side facing inward on the outer nozzles in figure 4.21b is compared, it's noted that they are similar to that of the frozen model in figure 4.21a. This indicates that the temperatures in this region is more dependent on the exhaust gases from the nozzle exit which circulates inside the nozzle cluster. The flow in the cluster will have minimal reactions compared to behind the shock, this is due to the timescale of the flow being smaller than that of the chemical timescale which means that the species don't have time to react and therefore the chemical non-equilibrium model will display similar results to the frozen chemistry.

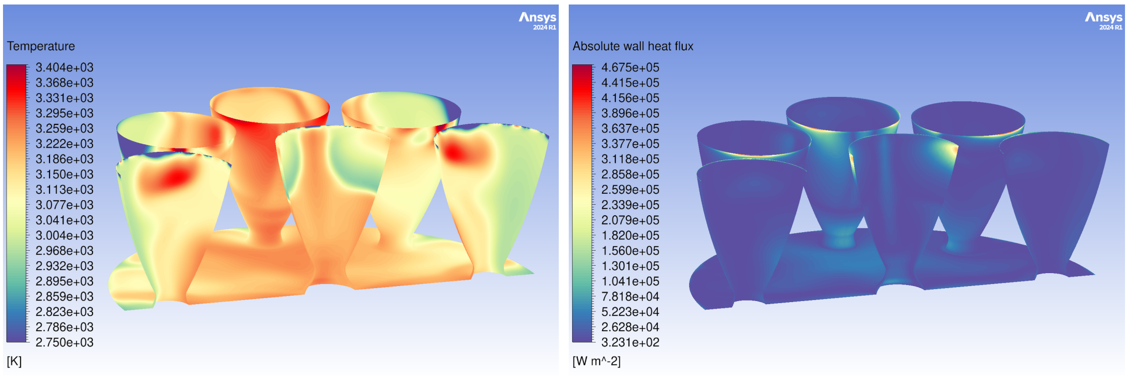

(a) Adiabatic nozzle wall temperature, chemical non-equilibrium.

(b) Heat transfer, $T = 300$K.

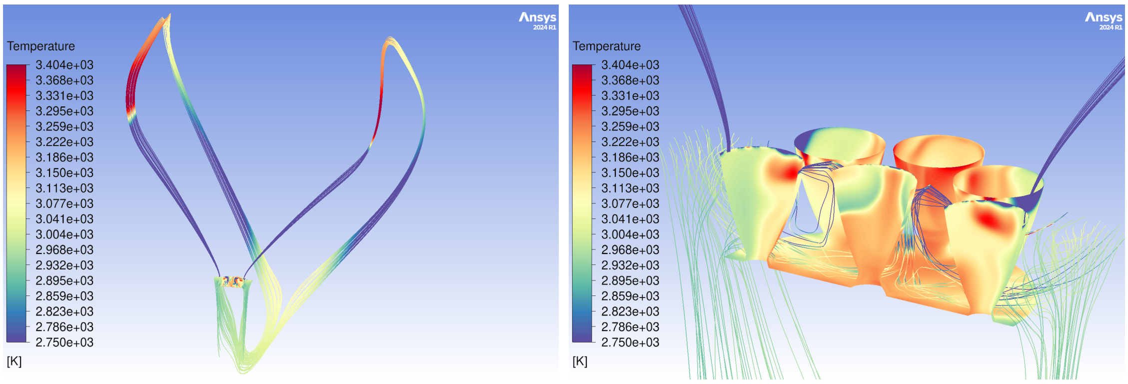

(c) The exhaust streamlines from the side nozzles, chemical non-equilibrium.

(d) A zoom in on the nozzles to showcase the streamlines coming out of the nozzles are the ones heating up the outside of the nozzles, chemical non-equilibrium.

Figure 4.21: Adiabatic temperature and heat transfer coefficient from start burn simulations. As well as the streamlines from the exhaust.

4.3.2 End of the burn

The HTC simulations were made with frozen chemistry and with a wall temperature as a profile such as for the start of the burn and can be seen in figure 4.22. The adiabatic wall temperature measures between 4100 and 2900 K with peak temperatures found on the outside of the nozzles, specially the unactivated side nozzles 3 and 7 (from figure 3.2). The heat transfer coefficient peaks at around 150 $\mathrm{W/(m^2\,K)}$ locally on the center nozzle towards the activated side nozzles 1 and 5. The unactivated side nozzles 3 and 7 also show an increased HTC at approximate 60 $\mathrm{W/(m^2\,K)}$. Figures 4.22c and 4.22d show recirculation from the exhaust from both side- and center nozzle down into the nozzle cluster.

Similar to start burn the nozzles exhibits the highest temperature at the outside of the nozzles due to the exhaust gases after the shock circulating back and into sides of the nozzles facing outward. But in contrast to start burn where there is a clear difference in temperature between the side facing inward and outward of the nozzles there is also a clear difference between the upper and lower part of the nozzle in terms of temperature at end burn for the side activated nozzles. There is also a difference in the center nozzle where the start burn (figure 4.21a) has a colder region at the top of the nozzle while at the end burn (figure 4.24a) the cold region extends down until the throat. This is due to the exhaust from the side nozzles which hits the center nozzle wall as in figure 4.23 will stay attached to the wall and, as the exhaust is colder than the surrounding gas, it will cool down the nozzle. For the start burn the flow will separate much earlier explaining the smaller colder region at the top portion of the nozzle. As for the side nozzles, similarly to the start burn, there is a lot of high temperature gas at the side facing outward but, in contrast, there is a colder region at the lower part of the nozzles. This is most probably due to the increased amount of recirculation occurring at the end burn, as seen in figure 4.23. This recirculation within the cluster includes lower temperature exhaust which circulates around the lower part of the side nozzles which will result in lower temperature there compared to the start of the burn.

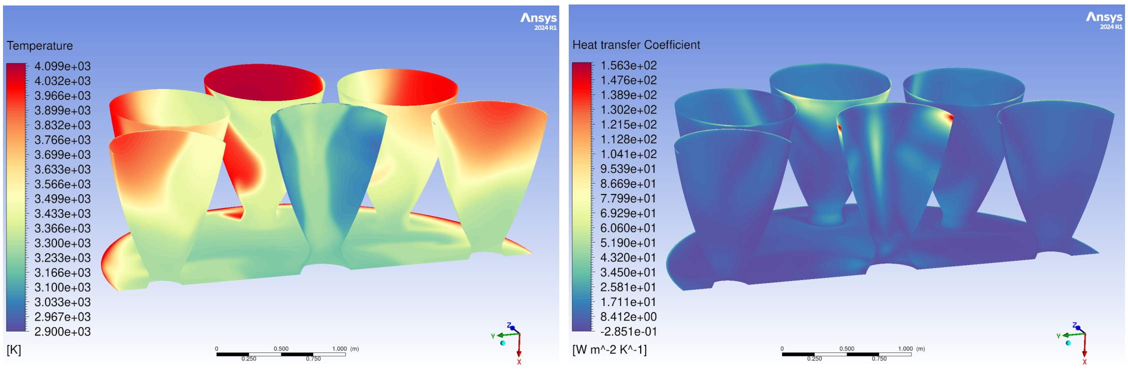

(a) Adiabatic nozzle wall temperature, frozen chemistry.

(b) Heat transfer coefficient.

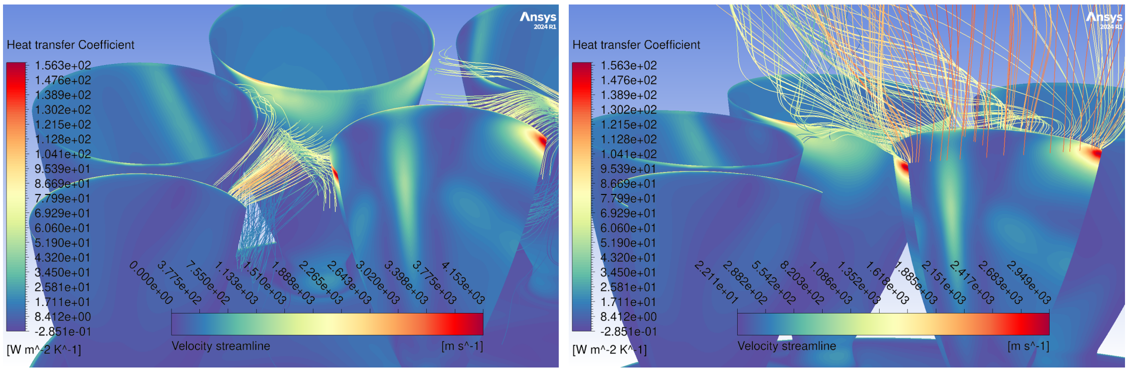

(c) Exhaust streamlines from side nozzle.

(d) Exhaust streamlines from center nozzle.

Figure 4.22: Adiabatic temperature and heat transfer coefficient from end burn simulations, frozen chemistry. Heat transfer coefficient calculated with wall temperature as a profile ($dT = 100\,\mathrm{K}$).

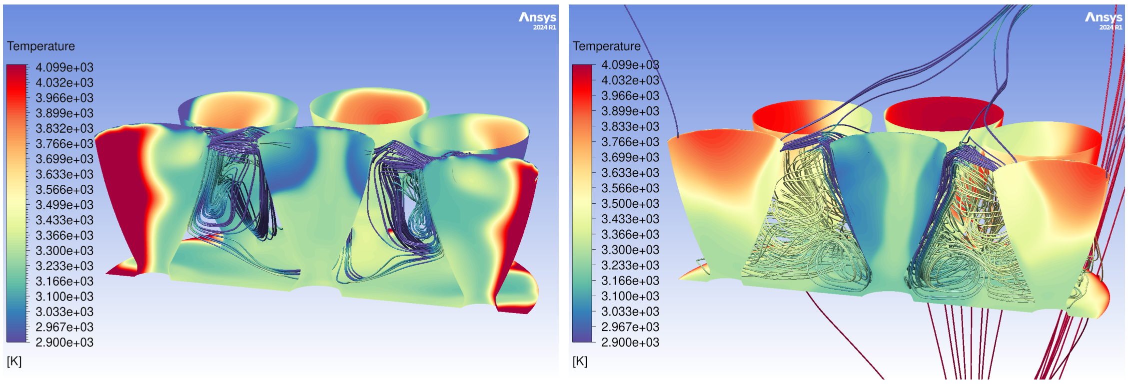

(a) Streamlines from the side nozzles at the start of the burn.

(b) Streamlines from the side nozzles at the end of the burn.

Figure 4.23: Comparison of the exhaust from the side nozzles at the start and end of the burn, frozen chemistry.

The adiabatic wall temperature and absolute wall heat flux with chemical non-equilibrium can be seen in figure 4.24. The adiabatic wall temperature spans between 2750 and 3400 K with the highest values on the unactivated side nozzle 3 and 7 and generally a higher temperature is found on the side facing the central nozzle than the side facing outwards. Local wall heat fluxes around 450 kW/m^2 on the central nozzle and values of approximately 200 kW/m^2 on the unactivated side nozzles 3 and 7. Similar to the start of the burn the temperatures on the walls facing outward will be lower than the frozen chemistry model due to endothermic reactions in the chemical non-equilibrium model.

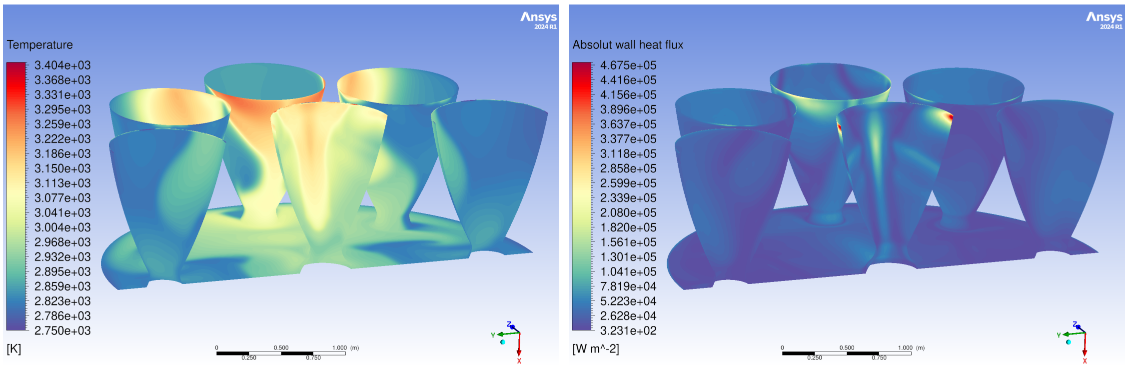

(a) Adiabatic nozzle wall temperature, chemical non-equilibrium.

(b) Heat transfer, $T = 300$K.

Figure 4.24: Adiabatic temperature and heat transfer coefficient from end burn simulations.

The pressures achieved at the nozzle walls during retro-propulsion during the start and end of the burn is shown in figure 4.25 below. It's evident that the highest pressures are achieved near the edge of the center nozzle which is the same location which the exhaust hits the nozzle when expanding from the side nozzles as seen in figure 4.19c. The maximum pressure achieved at the start of the burn is around 1500 Pa while at the end of the burn it's 2000 Pa. The pressure on most places of the nozzle walls is around 500 Pa for the end of the burn while at the start of the burn it's around 100 Pa. Similarly to the simulation without retro-propulsion the higher pressures at the end of the burn is probably due to the higher atmospheric pressure at that altitude.

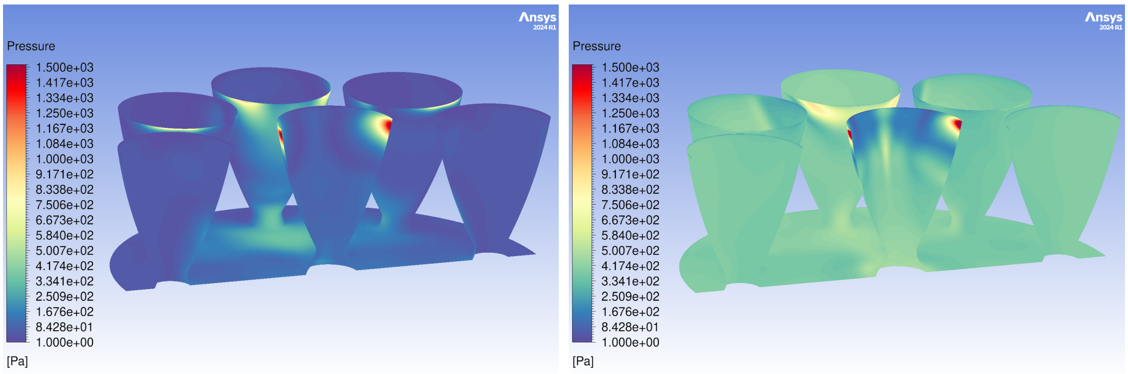

(a) Pressure at the nozzles at the start of the burn.

(b) Pressure at the nozzles at the end of the burn.

Figure 4.25: Comparison of the pressures during the start and end of the burn.

5

Challenges and future prospects

In this section some thoughts regarding implications of the results and potential sources of error will be discussed.

5.1 Implications for retro-propulsion designs

So far only the results from the simulations has been discussed, and not the implications it has on the nozzle or rocket. The magnitudes of the heat transfer coefficients as well as heat transfers are relatively low for all investigated phases of flight. This means that it's a possibility that the original designs, designed only for ascent, would be able to handle the thermal loads before, during and after reentry phase, however in order to claim this further investigation needs to be conducted. One can still use these results in order to potentially improve the design and mitigate the thermal loads and local hot spots. Two major design modifications are found: move the central nozzle so the exit is inline with the exit of the outer nozzles and not using an engine cluster but rather one larger engine in the center.

The first potential design modification in order to mitigate the thermal loads would be to have the exit of all of the nozzles level with one another, in other words, not have the central nozzle extended outward further than the outer nozzles. Since one of the major heat transfer areas during retro-propulsion is on the central nozzle when the exhaust from the side nozzles bend downward and hit the central nozzle. Though no further studies has been made, this behavior is believed to be greatly minimized if the center nozzle would be level with the other nozzles, this due to the stagnation point between the exhausts from the nozzles would then be on equal distance from both the nozzles. This is believed to have the most significant effects at lower altitudes where there is less plume spreading as the higher altitudes has significant heat transfer on the non-active side nozzles as well.

The second design modification would be to only have one larger engine in the center of the rocket. The major heat transfer without retro-propulsion is located at the throat of the outer nozzles due to the stagnation points and recirculation in the cluster arrangement. If a design where only one larger engine, as found in Ariane 6 rocket, this heat transfer would most likely be drastically lowered. Having only one engine would also mitigate the effects of recirculation from the nozzles during retro-propulsion. This design would however result in a complete redesign of the entire engine, as it would need to produce power equal to the existing 9 engines, and most likely the rocket as well. The other issue of this design would be the necessity of throttling and a greater thrust vectoring in order to perform a safe and reliable landing.

5.2 Limitations and sources of error

This project is unfortunately not without its sources of errors and the major errors will be discussed and its potential effects.

The possible error, as discussed earlier, is the mesh convergence of the retro-propulsion simulations in 3D. With the final mesh which has around 6 million cells and the chemical non-equilibrium model, the RAM usage and high computational cost put limitations on not using a fully converged mesh. As seen in table 3.3, the average nozzle temperature decreased with the Richardson extrapolation which indicates that the chosen mesh (fine) is most likely on the conservative side when it comes to heat transfer. How the non converged mesh effects the HTC is however harder to say, as it is dependent on the flow, and would require further investigation in order to determine.

The methane chemistry model used should also be discussed. The model used in this project, as well as most other earlier studies, is a methane model intended for combustion simulations, in other words high temperature and high pressure simulations. In this application however, there is a large variation of temperature over the domain, and very low pressures. As previously described, CHEMKIN format uses the modified Arrhenius equation which is a semi-empirical format with constants derived from experiments, most likely conducted in high pressure environments. As mentioned in section 3.6.2, the model was evaluated for 60 bar, which is about 200,000 times higher pressure than the ≈ 30 Pa atmospheric pressure found at start burn. It is therefore possible that there is large difference in chemical behavior between the models intended use and the application of retro-propulsion.

Another source of error is the extremely low pressures found in start burn with retro-propulsion. Pressures of below 1 Pa are found near the edge of the exit of the nozzle which most likely results in a Knudsen number above 0.001, which is the limit for the continuum regime and the use of CFD and the Navier-Stokes equations. This means that there are most certain great errors in this region due to the reduction in accuracy of the numerical methods used. The CFD software, ANSYS Fluent, limits the pressure to not be able to go below 1 Pa which further increases the uncertainty of the true behavior of the fluid in this region. It is possible to decrease this lower limit, this would however only resulted in a further decrease in accuracy of the simulations.

A source of error which was found later is that when running the chemical non-equilibrium simulations with a constant wall temperature of 300 K the wall y^+ is increased by around a factor of 10. So instead of having an area weighted average wall y^+ of under 0.1 it's now instead over 0.1 but still below 1. This could be explained by the temperature boundary condition at the walls. For the adiabatic simulation during retro-propulsion at the start of the burn the area weighted average temperature of the center nozzle is 3132.14 K which is around 2800 K higher than the prescribed wall temperature of 300 K. With that much higher temperature, the adiabatic simulation will therefore have a lower viscosity which means that the y^+ will be lower for the same cell distance. The y^+ for the adiabatic simulations where 0.045 while for the 300 K case it was 0.477 so a significant difference. This should be taken into consideration as it could affect the heat flux but as the value is still below 1 it means that the solver is still resolving the boundary layer and not using wall functions. Therefore the results are still deemed okay even though they do not fulfill the set criteria.

A last thing to note is that all the simulations are run with a steady state RANS simulations whereas the retro-propulsion simulations are highly unsteady and require higher fidelity transient simulations such as LES. So a lot of the analysis made would look different if a transient simulation was utilized.

5.3 Future work

Even though the project was able to answer the questions that were set out at the beginning, there is much more to be investigated in the field of thermal loading on nozzles during retro-propulsion. A common approach to aerothermal investigation during a launch, is by developing an aerothermal database, where multiple phases of flight are simulated. The results from the simulations are then interpolated and used for thermal simulations in solid mechanics. However, the computational costs for the final 3D simulations with retro-propulsion and necessary chemistry were extremely high with the heaviest simulation running for over 20.000 CPU-hours before reaching convergence. This means that additional research needs to be conducted in order to reduce the model to be able to conduct more rapid investigations to extend the database and get a better understanding of the loading during the entire reentry phase of flight.

Another major area in need of further investigation, is the landing burn for a rocket using a liquid methane-oxygen engine. This topic has not been investigated in this thesis nor any other publicly available research with focus on thermal loading on or around the nozzles. During this phase there is substantially different flow behavior and physics as the rocket is no longer flying in supersonic speeds while there is a significantly higher ambient pressure. Another major difference is the plume-ground interaction which will not only affect the flow behavior of the exhaust, but will also heat the ground resulting in the ground omitting thermal radiation. A finding noted in this thesis is that during the end burn, higher HTC and pressure loads were achieved during the end burn where the dynamic pressure and density is higher. Therefore an interesting simulation to conduct is to look at the heat loads and pressure loads at lower altitudes where the highest dynamic pressures are achieved. That point could potentially result in higher HTC and pressures even when the engines are off during that time and should therefore be investigated in the future.

The Prometheus engine, the engine GKN Aerospace is contributing to the development, is a gas generator cycle where its exhaust gets ejected through an exhaust pipe at the base of the rocket. According to Tamas Bykerk [2], methane produces less soot than kerosene fuels. However, they also state that soot radiation can have a significant impact on thermal loading [2]. Even though methane produces less it should still be taken into consideration. Bykerk [2] also state that the placement of the secondary generator exhaust can heavily effect the flow inside the nozzle cluster and reduce the flow reversal. However, as most gas generators burns fuel rich, there is likely to be significant post combustion as oxygen is introduced to the flow. As the effect of the exhaust from the gas generator may have an important impact on the thermal loading, it motivates further investigation.

The last major proposed future work is the influence of turbulence model. As earlier studies have stated, the choice of turbulence model has a significant impact on plume structure and flow behavior, however this has only been scarcely studied. Turbulence, which often is prevalent near walls and boundary layers, will also have considerable effect on heat transfer for reentry which needs to be understood in order to accurately simulate the thermal loads on the nozzles during reentry. It was also noted that there are unsteady effects which needs to be taken into consideration and therefore a future work would be to use transient simulations. That would be a challenge as the simulation time is already time consuming in a steady state simulation but the transient simulation and especially with higher fidelity could result in a lot of new knowledge found.

6

Conclusion

This study set out to investigate the flow behavior and aerothermal loads on and around the nozzles during reentry of a first-stage rocket booster, identify possible simplifications to the model and analyze the physics present on and around the nozzles during retro-propulsion. To achieve this, CFD simulations were carried out and analyzed in 2D and 3D where four different phases- and flight configurations were investigated. Hopefully these insights, brought on with this thesis, will shed light on an area of research not broadly investigated in the academic field.

The prestudy provided valuable results and understanding on how the model could be reduced in order to decrease computational cost, without compromising accuracy. The prestudy concluded that, during the reentry burn without retro-propulsion, calorically perfect gas was an imprecise model as the temperature reached above its range of use, but as the temperatures and Damköhler number are relatively low, it makes the frozen chemistry model appropriate, reducing the cost compared to reacting chemical models. For simulations with retro-propulsion however, the temperatures are significantly higher with a larger variation of Damköhler number over the domain, chemical non-equilibrium was necessary and the most accurate model in order to capture the relevant chemistry in the flow and temperatures around the nozzles. The heat transfer coefficient (HTC) results from the prestudy concluded that the HTC is temperature independent for both wall temperature as a profile (ΔT) and constant wall temperature, where the constant wall temperature gave a slight variation downstream of the flow. HTC simulations with retro-propulsion were found to have only a small variation between chemical non-equilibrium and frozen chemistry. Lastly, the developed 13-species scheme was found to produce close to identical results to the original 24-species reaction scheme significantly reducing the computational time and RAM usage.

The 3D simulations provided more detailed understanding of the flow behavior capturing 3D effects and effects from an engine cluster. The results without retro-propulsion show a maximum adiabatic wall temperature of approximately $2460\,\mathrm{K}$ and $1524\,\mathrm{K}$ for start and end burn respectively. The throat is the area of the nozzles most exposed to thermal loads where local HTC and heat flux measure $70\,\mathrm{W/(m^2\,K)}$ and $150\,\mathrm{kW/m^2}$ at the start of the burn. End burn simulations result in higher heat loads, most likely due to higher atmospheric pressures and density, of approximately $150\,\mathrm{W/(m^2\,K)}$ and $200\,\mathrm{kW/m^2}$. With retro-propulsion the adiabatic wall temperatures varies between 2800 and 3300 K for the chemical non-equilibrium model and the HTC is locally approximately 150 W/(m^2 K) for both end and start burn while the heat flux is 400 and 450 kW/m^2 for start and end burn respectively. The HTC and heat flux was found to be mainly due to high speed exhaust hitting the nearby engines and the recirculation inside the engine cluster. While thermal exposure such as maximum temperature differed depending on the model used. For the chemical non-equilibrium model which is most likely the one closest to reality, the exhaust gases passing the shock will have a lower temperature than the frozen chemistry model due to reactions and will therefore not expose the nozzles at the side facing outward as much as the frozen chemistry model. So while the frozen chemistry model will result in highest temperature at the sides facing outward in reality it will most likely be the surfaces facing the center which will be most exposed as seen in the chemical non-equilibrium model. But nonetheless it's noted that the HTC is most dependent on high speed flows where a more turbulent flow and flows with higher pressures and density as during the end burn will result in higher HTC.

The results from this study can clearly describe much of the flow behavior and impact of chemical models. The conclusions and derived thermal loads are predicted to help GKN Aerospace in their future work in investigation and design of future reusable rocket nozzles.

Bibliography

[1] Roger D. Launius. *The Smithsonian History of Space Exploration: From the Ancient World to the Extraterrestrial Future*. Quarto Publishing Prt., 2018.

[2] Tamas Bykerk et al. “Retro-propulsion in rocket systems: Recent advancements and challenges for the prediction of aerodynamic characteristics and thermal loads”. In: *Progress in Aerospace Sciences* 151 (2024), p. 101044. ISSN: 0376-0421. DOI: `https://doi.org/10.1016/j.paerosci.2024.101044`. URL: `https://www.sciencedirect.com/science/article/pii/S0376042124000708`.

[3] Mariasole Laureti et al. “Aerothermal analysis of the RETPRO flight configuration”. In: *9th Edition of the 3AF International Conference on Space Propulsion 2024*. Ed. by 3AF. May 2024, pp. 1–11. URL: `https://elib.dlr.de/198838/`.

[4] Daniel Kirchheck et al. “Validation of Wind Tunnel Test and CFD Techniques for Retro-propulsion (RETPRO): Overview on a Project within the Future Launchers Preparatory Programme (FLPP)”. In: Oct. 2019.

[5] Etienne Dumont et al. “CALLISTO - Reusable VTVL launcher first stage demonstrator”. In: May 2018.

[6] Alessandra Iannetti et al. “Prometheus, a LOX/LCH4 reusable rocket engine”. In: *Proceedings of the 7th European Conference for Aeronautics and Space Sciences (EUCASS), Milan, Italy*. 2017, pp. 1–6.

[7] Tobias Ecker et al. “Aerothermal characterization of the CALLISTO vehicle during descent”. In: *CEAS Space Journal* (Aug. 2024). ISSN: 1868-2510. DOI: `10.1007/s12567-024-00561-z`. URL: `http://dx.doi.org/10.1007/s12567-024-00561-z`.

[8] Yipu Zhao and Haiming Huang. “Numerical study of hypersonic surface heat flux with different air species models”. In: *Acta Astronautica* 169 (2020), pp. 84–93. ISSN: 0094-5765. DOI: `https://doi.org/10.1016/j.actaastro.2020.01.002`. URL: `https://www.sciencedirect.com/science/article/pii/S0094576520300023`.

[9] Wei Zhao et al. “Evaluation of Thermodynamic and Chemical Kinetic Models for Hypersonic and High-Temperature Flow Simulation”. In: *Applied Sciences* 13 (Sept. 2023), p. 9991. DOI: `10.3390/app13179991`.

[10] Ansgar Marwege and Ali Gülhan. “Unsteady Aerodynamics of the Retro-propulsion Reentry Burn of Vertically Landing Launchers”. In: *Journal of Spacecraft and Rockets* 60.6 (2023), pp. 1939–1953. DOI: `10.2514/1.A35647`.

eprint: `https://doi.org/10.2514/1.A35647`. URL: `https://doi.org/10.2514/1.A35647`.

[11] Lars Davidson. *Fluid mechanics, turbulent flow and turbulence modeling*. Chalmers, 2025.

[12] Florian R Menter. *Improved two-equation k-omega turbulence models for aerodynamic flows*. Tech. rep. 1992.

[13] John D. Andersson. *Modern Compressible Flow: with historical perspective*. McGraw-Hill Education, 2021.

[14] Phillip G. Hill and Carl R. Peterson. *Mechanics and Thermodynamics of Propulsion*. Addison-Wesley publishing Company, 1992.

[15] P. O. Jarvinen and R. H. Adams. *The aerodynamic characteristics of large angled cones with retrorockets*. Tech. rep. NASA-CR-124720. NASA Technical Reports Server (NTRS), 1970. URL: `https://ntrs.nasa.gov/search.jsp?R=19720005324`.

[16] Balaji Venkatachari et al. "Numerical Study of Counterflowing Jet Effects on Supersonic Slender-Body Configurations". In: June 2015. DOI: `10.2514/6.2015-3010`.

[17] Kevin Gutsche, Ansgar Marwege, and Ali Gülhan. "Similarity and Key Parameters of Retropropulsion Assisted Deceleration in Hypersonic Wind Tunnels". In: *Journal of Spacecraft and Rockets* 58.4 (July 2021), pp. 984–996. ISSN: 1533-6794. DOI: `10.2514/1.a34910`. URL: `http://dx.doi.org/10.2514/1.A34910`.

[18] Tobias Ecker et al. "Aerothermal Analysis of Reusable Launcher Systems during Retro-Propulsion Reentry and Landing". In: *Space Propulsion Conference 2018*. Sevilla, Spain, 2018. URL: `https://elib.dlr.de/120072/`.

[19] Paolo Barbante. "Fundamentals of hypersonic flight-Properties of high temperature gases". In: (Mar. 2015).

[20] Wenqing Zhang et al. *A review of the mathematical modeling of equilibrium and nonequilibrium hypersonic flows*. 2022. DOI: `10.1186/s42774-022-00125-x`. URL: `/article/id/b24c2182-94b8-4ab1-bcf2-8e471166102e`.

[21] Benjamin J. Isaac et al. "A Novel Methodology for Chemical Time Scale Evaluation with Detailed Chemical Reaction Kinetics". In: *Energy & Fuels* 27.4 (2013), pp. 2255–2265. DOI: `10.1021/ef301961x`. eprint: `https://doi.org/10.1021/ef301961x`. URL: `https://doi.org/10.1021/ef301961x`.

[22] W Malalasekera H K Versteeg. *An Introduction To Computational Fluid Dynamics: The Finite Volume Method*. Pearson Education Limited, 2007.

[23] K. J. Laidler. In: *Pure and Applied Chemistry* 68.1 (1996), pp. 149–192. DOI: `doi:10.1351/pac199668010149`. URL: `https://doi.org/10.1351/pac199668010149`.

[24] Tamas Bykerk. "A standard model for the investigation of aerodynamic and aerothermal loads on a re-usable launch vehicle". In: July 2023.

[25] Sebastian Karl, Tamas Bykerk, and Mariasole Laureti. "Design of a truncated ideal nozzle for a re-usable first stage launcher". In: Mar. 2025.

[26] *Ansys®, Release 24.R2, Help System, Chemkin Input Manual 2.2 Default Data Format*. Available online: `https://ansyshelp.ansys.com/public/account/`

secured?returnurl=////////Views/Secured/corp/v242/en/chemkin_in/i63642.html. ANSYS, Inc. 2025.

[27] *Ansys®, Release 24.R2, Help System, Chemkin Input Manual 5.1 Transport Data Format.* Available online: https://ansyshelp.ansys.com/public/account/secured?returnurl=////////Views/Secured/corp/v242/en/chemkin_in/i63642.html. ANSYS, Inc. 2025.

[28] *Ansys®, Release 24.R2, Help System, Chemkin Input Manual 4.5.2. Reaction Data.* Available online: https://ansyshelp.ansys.com/public/account/secured?returnurl=////////Views/Secured/corp/v242/en/chemkin_in/marker-1085538.html. ANSYS, Inc. 2025.

[29] *Ansys®, Release 24.R2, Help System, Chemkin Input Manual 4.5.3 Auxiliary Reaction Data.* Available online: https://ansyshelp.ansys.com/public/account/secured?returnurl=////////Views/Secured/corp/v242/en/chemkin_in/i43758.html. ANSYS, Inc. 2025.

[30] Chul Park, Richard Jaffe, and Harry Partridge. "Chemical-Kinetic Parameters of Hyperbolic Earth Entry". In: *Journal of Thermophysics and Heat Transfer - J THERMOPHYS HEAT TRANSFER* 15 (Jan. 2001), pp. 76–90. DOI: 10.2514/2.6582.

[31] Victor P. Zhukov and Alan F. Kong. "A Compact Reaction Mechanism of Methane Oxidation at High Pressures". In: *Progress in Reaction Kinetics and Mechanism* 43.1 (2018), pp. 62–78. DOI: 10.3184/146867818X15066862094914. eprint: https://doi.org/10.3184/146867818X15066862094914. URL: https://doi.org/10.3184/146867818X15066862094914.

A

Chemical models

A.1 Air chemical model

Table A.1: Arrhenius constants for chemical reactions in air model, constants from Park2001 [30]. Preexponential factor A_r in [cal/mole] and activation energy E_r in [mole-cm-s-K]

Species				
N_2, O_2, N, O, NO				
	Reaction	A_r	n	E_r
1.	$O_2 + N \leftrightarrow 2O + N$	$1.000 \cdot 10^{22}$	-1.500	$1.179 \cdot 10^{5}$
2.	$O + O_2 \leftrightarrow 3O$	$1.000 \cdot 10^{22}$	-1.500	$1.179 \cdot 10^{5}$
3.	$O_2 + N_2 \leftrightarrow 2O + N_2$	$2.000 \cdot 10^{21}$	-1.500	$1.179 \cdot 10^{5}$
4.	$2O_2 \leftrightarrow 2O + O_2$	$2.000 \cdot 10^{21}$	-1.500	$1.179 \cdot 10^{5}$
5.	$NO + O_2 \leftrightarrow 2O + NO$	$2.000 \cdot 10^{21}$	-1.500	$1.179 \cdot 10^{5}$
6.	$N + N_2 \leftrightarrow 3N$	$3.000 \cdot 10^{22}$	-1.600	$2.249 \cdot 10^{5}$
7.	$O + N_2 \leftrightarrow O + 2N$	$3.000 \cdot 10^{22}$	-1.600	$2.249 \cdot 10^{5}$
8.	$2N_2 \leftrightarrow 2N + N_2$	$7.000 \cdot 10^{21}$	-1.600	$2.249 \cdot 10^{5}$
9.	$O_2 + N_2 \leftrightarrow 2N + O_2$	$7.000 \cdot 10^{21}$	-1.600	$2.249 \cdot 10^{5}$
10.	$NO + N_2 \leftrightarrow 2N + NO$	$7.000 \cdot 10^{21}$	-1.600	$2.249 \cdot 10^{5}$
11.	$N + NO \leftrightarrow O + 2N$	$1.100 \cdot 10^{17}$	0.000	$1.500 \cdot 10^{5}$
12.	$O + NO \leftrightarrow 2O + N$	$1.100 \cdot 10^{17}$	0.000	$1.500 \cdot 10^{5}$
13.	$NO + N_2 \leftrightarrow O + N + N_2$	$5.000 \cdot 10^{15}$	0.000	$1.500 \cdot 10^{5}$
14.	$NO + O_2 \leftrightarrow O + N + O_2$	$5.000 \cdot 10^{15}$	0.000	$1.500 \cdot 10^{5}$
15.	$2NO \leftrightarrow O + N + NO$	$1.100 \cdot 10^{17}$	0.000	$1.500 \cdot 10^{5}$
16.	$O + NO \leftrightarrow N + O_2$	$8.400 \cdot 10^{12}$	0.000	$3.855 \cdot 10^{4}$
17.	$O + N_2 \leftrightarrow N + NO$	$5.700 \cdot 10^{12}$	0.420	$8.532 \cdot 10^{4}$

A.2 Methane chemical model

The Arrhenius constants for equation 2.48 used in chemical equilibrium and non-equilibrium simulations with exhaust can be seen in tables A.2 - A.4. M in the reactions refers the collision with an arbitrary third party specie. In notes: '*' refers to additional information for reaction found in table A.4 and *Duplicate* refers to identical reactions occurring through different reaction paths. Table A.4 provides information on how the reactions vary with different species of M. The term *LOW* refers to chemical parameters at low pressures, while *TROE* describes the pressure-dependent behavior in transition regions. For further details, consult the ANSYS and CHEMKIN manuals.

Table A.2: Arrhenius constants for chemical reactions in methane model, constants from Zhukov-Kong 2018 [31]. Pre-exponential factor A_r is in [cal/mole] and activation energy E_r is in [mole-cm-s-K].

<table>
<tr><th colspan="6">Species</th></tr>
<tr><td colspan="6">$H_2, H, O, O_2, OH, H_2O, HO_2, H_2O_2, CH_2, CH_3, CH_4, CO, CO_2$
$HCO, CH_2O, CH_3O, C_2H_3, C_2H_4, C_2H_5, CH_3O_2, N, C_2H_6$</td></tr>
<tr><th></th><th>Reaction</th><th>A_r</th><th>n</th><th>E_r</th><th>Note</th></tr>
<tr><td>1.</td><td>$O_2 + CH_2O \leftrightarrow HO_2 + HCO$</td><td>$1.000 \cdot 10^{14}$</td><td>$0.000$</td><td>$4.000 \cdot 10^{4}$</td><td></td></tr>
<tr><td>2.</td><td>$H + O_2 + M \leftrightarrow HO_2 + M$</td><td>$2.800 \cdot 10^{18}$</td><td>$-0.860$</td><td>$0.000$</td><td>*</td></tr>
<tr><td>3.</td><td>$H + 2O_2 \leftrightarrow HO_2 + O_2$</td><td>$3.000 \cdot 10^{20}$</td><td>$-1.720$</td><td>$0.000$</td><td></td></tr>
<tr><td>4.</td><td>$H + CH_2O(+M) \leftrightarrow CH_3O(+M)$</td><td>$5.400 \cdot 10^{11}$</td><td>$0.454$</td><td>$2.600 \cdot 10^{3}$</td><td>*</td></tr>
<tr><td>5.</td><td>$2OH(+M) \leftrightarrow H_2O_2(+M)$</td><td>$7.400 \cdot 10^{13}$</td><td>$-0.370$</td><td>$0.000$</td><td>*</td></tr>
<tr><td>6.</td><td>$OH + HO_2 \leftrightarrow O_2 + H_2O$</td><td>$2.900 \cdot 10^{13}$</td><td>$0.000$</td><td>$-500.000$</td><td></td></tr>
<tr><td>7.</td><td>$OH + H_2O_2 \leftrightarrow HO_2 + H_2O$</td><td>$1.750 \cdot 10^{12}$</td><td>$0.000$</td><td>$320.000$</td><td>Dublicate</td></tr>
<tr><td>8.</td><td>$OH + H_2O_2 \leftrightarrow HO_2 + H_2O$</td><td>$5.800 \cdot 10^{14}$</td><td>$0.000$</td><td>$9.560 \cdot 10^{3}$</td><td>Dublicate</td></tr>
<tr><td>9.</td><td>$OH + CH_4 \leftrightarrow CH_3 + H_2O$</td><td>$1.000 \cdot 10^{8}$</td><td>$1.600$</td><td>$3.120 \cdot 10^{3}$</td><td></td></tr>
<tr><td>10.</td><td>$2HO_2 \leftrightarrow O_2 + H_2O_2$</td><td>$1.300 \cdot 10^{11}$</td><td>$0.000$</td><td>$-1.630 \cdot 10^{3}$</td><td>Dublicate</td></tr>
<tr><td>11.</td><td>$2HO_2 \leftrightarrow O_2 + H_2O_2$</td><td>$4.200 \cdot 10^{14}$</td><td>$0.000$</td><td>$1.200 \cdot 10^{4}$</td><td>Dublicate</td></tr>
<tr><td>12.</td><td>$HO_2 + CH_3 \leftrightarrow O_2 + CH_4$</td><td>$1.000 \cdot 10^{12}$</td><td>$0.000$</td><td>$0.000$</td><td></td></tr>
<tr><td>13.</td><td>$HO_2 + CH_3 \leftrightarrow OH + CH_3O$</td><td>$2.000 \cdot 10^{13}$</td><td>$0.000$</td><td>$0.000$</td><td></td></tr>
<tr><td>14.</td><td>$HO_2 + CO \leftrightarrow OH + CO_2$</td><td>$1.500 \cdot 10^{14}$</td><td>$0.000$</td><td>$2.360 \cdot 10^{4}$</td><td></td></tr>
<tr><td>15.</td><td>$HO_2 + CH_2O \leftrightarrow HCO + H_2O_2$</td><td>$1.000 \cdot 10^{12}$</td><td>$0.000$</td><td>$8.000 \cdot 10^{3}$</td><td></td></tr>
<tr><td>16.</td><td>$CH_3 + O_2 \leftrightarrow O + CH_3O$</td><td>$2.675 \cdot 10^{13}$</td><td>$0.000$</td><td>$2.880 \cdot 10^{4}$</td><td></td></tr>
<tr><td>17.</td><td>$CH_3 + O_2 \leftrightarrow OH + CH_2O$</td><td>$3.600 \cdot 10^{10}$</td><td>$0.000$</td><td>$8.940 \cdot 10^{3}$</td><td></td></tr>
<tr><td>18.</td><td>$CH_3 + H_2O_2 \leftrightarrow HO_2 + CH_4$</td><td>$2.450 \cdot 10^{4}$</td><td>$2.470$</td><td>$5.180 \cdot 10^{3}$</td><td></td></tr>
<tr><td>19.</td><td>$CH_3 + CH_2O \leftrightarrow HCO + CH_4$</td><td>$3.320 \cdot 10^{3}$</td><td>$2.810$</td><td>$5.860 \cdot 10^{3}$</td><td></td></tr>
<tr><td>20.</td><td>$CH_3O + HO_2 \leftrightarrow CH_2O + H_2O_2$</td><td>$1.200 \cdot 10^{13}$</td><td>$0.000$</td><td>$0.000$</td><td></td></tr>
<tr><td>21.</td><td>$CH_3O_2 + CH_3 \leftrightarrow CH_3O + CH_3O$</td><td>$3.000 \cdot 10^{13}$</td><td>$0.000$</td><td>$-1.200 \cdot 10^{3}$</td><td></td></tr>
<tr><td>22.</td><td>$CH_3O + O_2 \leftrightarrow HO_2 + CH_2O$</td><td>$4.280 \cdot 10^{-13}$</td><td>$7.600$</td><td>$-3.530 \cdot 10^{3}$</td><td></td></tr>
<tr><td>23.</td><td>$CH_3 + O_2 \leftrightarrow CH_3O_2$</td><td>$1.700 \cdot 10^{60}$</td><td>$-15.100$</td><td>$1.8785 \cdot 10^{4}$</td><td></td></tr>
<tr><td>24.</td><td>$CH_3O + CH_3 \leftrightarrow CH_2O + CH_4$</td><td>$2.410 \cdot 10^{13}$</td><td>$0.000$</td><td>$0.000$</td><td></td></tr>
<tr><td>25.</td><td>$O + CH_4 \leftrightarrow OH + CH_3$</td><td>$1.020 \cdot 10^{9}$</td><td>$1.500$</td><td>$8.600 \cdot 10^{3}$</td><td></td></tr>
<tr><td>26.</td><td>$H + O_2 \leftrightarrow O + OH$</td><td>$8.300 \cdot 10^{13}$</td><td>$0.000$</td><td>$1.4413 \cdot 10^{4}$</td><td></td></tr>
<tr><td>27.</td><td>$H + O_2 + H_2O \leftrightarrow HO_2 + H_2O$</td><td>$9.380 \cdot 10^{18}$</td><td>$-0.760$</td><td>$0.000$</td><td></td></tr>
<tr><td>28.</td><td>$O + H_2 \leftrightarrow H + OH$</td><td>$5.000 \cdot 10^{4}$</td><td>$2.670$</td><td>$6.290 \cdot 10^{3}$</td><td></td></tr>
<tr><td>29.</td><td>$O + CH_3 \leftrightarrow H + CH_2O$</td><td>$8.430 \cdot 10^{13}$</td><td>$0.000$</td><td>$0.000$</td><td></td></tr>
<tr><td>30.</td><td>$O + CO + M \leftrightarrow CO_2 + M$</td><td>$6.020 \cdot 10^{14}$</td><td>$0.000$</td><td>$3.000 \cdot 10^{3}$</td><td>*</td></tr>
<tr><td>31.</td><td>$H + OH + M \leftrightarrow H_2O + M$</td><td>$2.200 \cdot 10^{22}$</td><td>$-2.000$</td><td>$0.000$</td><td>*</td></tr>
<tr><td>32.</td><td>$H + CH_3(+M) \leftrightarrow CH_4(+M)$</td><td>$1.270 \cdot 10^{16}$</td><td>$-0.630$</td><td>$383.000$</td><td>*</td></tr>
<tr><td>33.</td><td>$H + HCO(+M) \leftrightarrow CH_2O(+M)$</td><td>$1.090 \cdot 10^{12}$</td><td>$0.480$</td><td>$-260.000$</td><td>*</td></tr>
<tr><td>34.</td><td>$H + C_2H_4(+M) \leftrightarrow C_2H_5(+M)$</td><td>$1.080 \cdot 10^{12}$</td><td>$0.454$</td><td>$1.820 \cdot 10^{3}$</td><td>*</td></tr>
<tr><td>35.</td><td>$H + C_2H_4 \leftrightarrow C_2H_3 + H_2$</td><td>$1.325 \cdot 10^{6}$</td><td>$2.530$</td><td>$1.2240 \cdot 10^{4}$</td><td></td></tr>
</table>

Table A.3: Continue of Arrhenius constants for chemical reactions in methane model, constants from Zhukov-Kong 2018 [31]. Pre-exponential factor A_r in [cal/-mole] and activation energy E_r in [mole-cm-s-K].

	Reaction	A_r	n	E_r	Note
36.	$H + C_2H_6 \leftrightarrow C_2H_5 + H_2$	$1.150 \cdot 10^8$	1.900	$7.530 \cdot 10^3$	
37.	$OH + H_2 \leftrightarrow H + H_2O$	$2.160 \cdot 10^8$	1.510	$3.430 \cdot 10^3$	
38.	$OH + CH_2 \leftrightarrow H + CH_2O$	$2.000 \cdot 10^{13}$	0.000	0.000	
39.	$OH + C_2H_6 \leftrightarrow C_2H_5 + H_2O$	$3.540 \cdot 10^6$	2.120	870.000	
40.	$HCO + O_2 \leftrightarrow HO_2 + CO$	$7.600 \cdot 10^{12}$	0.000	400.000	
41.	$HCO + M \leftrightarrow H + CO + M$	$1.870 \cdot 10^{17}$	-1.000	$1.7000 \cdot 10^4$	*
42.	$CH_3 + OH \leftrightarrow CH_2O + H_2$	$8.000 \cdot 10^{12}$	0.000	0.000	
43.	$CH_2 + CH_3 \leftrightarrow H + C_2H_4$	$4.000 \cdot 10^{13}$	0.000	0.000	
44.	$O_2 + CO \leftrightarrow O + CO_2$	$2.500 \cdot 10^{12}$	0.000	$4.7800 \cdot 10^4$	
45.	$OH + CO \leftrightarrow H + CO_2$	$4.760 \cdot 10^7$	1.228	70.000	
46.	$OH + CH_2O \leftrightarrow HCO + H_2O$	$3.430 \cdot 10^9$	1.180	-447.000	
47.	$H + CH_2O \leftrightarrow HCO + H_2$	$2.300 \cdot 10^{10}$	1.050	$3.275 \cdot 10^3$	
48.	$2CH_3(+M) \leftrightarrow C_2H_6(+M)$	$2.120 \cdot 10^{16}$	-0.970	620.000	*
49.	$H + CH_4 \leftrightarrow CH_3 + H_2$	$6.600 \cdot 10^8$	1.620	$1.0840 \cdot 10^4$	
50.	$H + O_2 + N_2 \leftrightarrow HO_2 + N_2$	$2.600 \cdot 10^{19}$	-1.240	0.000	

Table A.4: Additional information used in methane reaction model in table A.2 and A.3, values taken from [31].

Reaction	Added line
2.	$O_2/0.00/H_2O/0.00/CO/0.75/CO_2/1.50/C_2H_6/1.50/N_2/0.00/$
3.	LOW / $2.200 \cdot 10^{30}$ -4.800 5560.00/ TROE/ 0.7580 94.00 1555.00 4200.00 / $H_2/2.00/H_2O/6.00/CH_4/2.00/CO/1.50/CO_2/2.00/C_2H_6/3.00/$
5.	LOW / $2.300 \cdot 10^{18}$ -0.900 -1700.00/ TROE/ 0.7346 94.00 1756.00 5182.00 / $H_2/2.00/H_2O/6.00/CH_4/2.00/CO/1.50/CO_2/2.00/C_2H_6/3.00/$
30.	$H_2/2.00/O_2/6.00/H_2O/6.00/CH_4/2.00/CO/1.50/CO_2/3.50/C_2H_6/3.00/$
31.	$H_2/0.73/H_2O/3.65/CH_4/2.00/C_2H_6/3.00/$
32.	LOW / $2.477 \cdot 10^{33}$ -4.760 2440.00/ TROE/ 0.7830 74.00 2941.00 6964.00 / $H_2/2.00/H_2O/6.00/CH_4/2.00/CO/1.50/CO_2/2.00/C_2H_6/3.00/$
33.	LOW / $1.350 \cdot 10^{24}$ -2.570 1425.00/ TROE/ 0.7824 271.00 2755.00 6570.00 / $H_2/2.00/H_2O/6.00/CH_4/2.00/CO/1.50/CO_2/2.00/C_2H_6/3.00/$
34.	LOW / $1.200 \cdot 10^{42}$ -7.620 6970.00/ TROE/ 0.9753 210.00 984.00 4374.00 / $H_2/2.00/H_2O/6.00/CH_4/2.00/CO/1.50/CO_2/2.00/C_2H_6/3.00/$
41.	$H_2/2.00/H_2O/12.0/CH_4/2.00/CO/1.50/CO_2/2.00/C_2H_6/3.00/$
48.	LOW / $1.770 \cdot 10^{50}$ -9.670 6220.00/ TROE/ 0.5325 151.00 1038.00 4970.00 / $H_2/2.00/H_2O/6.00/CH_4/2.00/CO/1.50/CO_2/2.00/C_2H_6/3.00/$

A.3 Reduced 10-specie methane chemical model

Table A.5: Arrhenius constants for chemical reactions in reduced 10-specie methane, constants from Zhukov-Kong 2018 [31]. Pre-exponential factor A_r is in [cal/mole] and activation energy E_r is in [mole-cm-s-K].

Species					
$H_2, H, O, O_2, OH, H_2O, HO_2, H_2O_2, CO, CO_2$					
	Reaction	A_r	n	E_r	Note
2.	$H + O_2 + M \leftrightarrow HO_2 + M$	$2.800 \cdot 10^{18}$	-0.860	0.000	*
3.	$H + 2O_2 \leftrightarrow HO_2 + O_2$	$3.000 \cdot 10^{20}$	-1.720	0.000	
5.	$2OH(+M) \leftrightarrow H_2O_2(+M)$	$7.400 \cdot 10^{13}$	-0.370	0.000	*
6.	$OH + HO_2 \leftrightarrow O_2 + H_2O$	$2.900 \cdot 10^{13}$	0.000	-500.000	
7.	$OH + H_2O_2 \leftrightarrow HO_2 + H_2O$	$1.750 \cdot 10^{12}$	0.000	320.000	Duplicate
8.	$OH + H_2O_2 \leftrightarrow HO_2 + H_2O$	$5.800 \cdot 10^{14}$	0.000	$9.560 \cdot 10^{3}$	Duplicate
10.	$2HO_2 \leftrightarrow O_2 + H_2O_2$	$1.300 \cdot 10^{11}$	0.000	$-1.630 \cdot 10^{3}$	Duplicate
11.	$2HO_2 \leftrightarrow O_2 + H_2O_2$	$4.200 \cdot 10^{14}$	0.000	$1.200 \cdot 10^{4}$	Duplicate
14.	$HO_2 + CO \leftrightarrow OH + CO_2$	$1.500 \cdot 10^{14}$	0.000	$2.360 \cdot 10^{4}$	
26.	$H + O_2 \leftrightarrow O + OH$	$8.300 \cdot 10^{13}$	0.000	$1.4413 \cdot 10^{4}$	
27.	$H + O_2 + H_2O \leftrightarrow HO_2 + H_2O$	$9.380 \cdot 10^{18}$	-0.760	0.000	
28.	$O + H_2 \leftrightarrow H + OH$	$5.000 \cdot 10^{4}$	2.670	$6.290 \cdot 10^{3}$	
30.	$O + CO + M \leftrightarrow CO_2 + M$	$6.020 \cdot 10^{14}$	0.000	$3.000 \cdot 10^{3}$	*
31.	$H + OH + M \leftrightarrow H_2O + M$	$2.200 \cdot 10^{22}$	-2.000	0.000	*
37.	$OH + H_2 \leftrightarrow H + H_2O$	$2.160 \cdot 10^{8}$	1.510	$3.430 \cdot 10^{3}$	
44.	$O_2 + CO \leftrightarrow O + CO_2$	$2.500 \cdot 10^{12}$	0.000	$4.7800 \cdot 10^{4}$	
45.	$OH + CO \leftrightarrow H + CO_2$	$4.760 \cdot 10^{7}$	1.228	70.000	
50.	$H + O_2 + N_2 \leftrightarrow HO_2 + N_2$	$2.600 \cdot 10^{19}$	-1.240	0.000	

A.4 Results

A.4.1 Comparison start and end burn

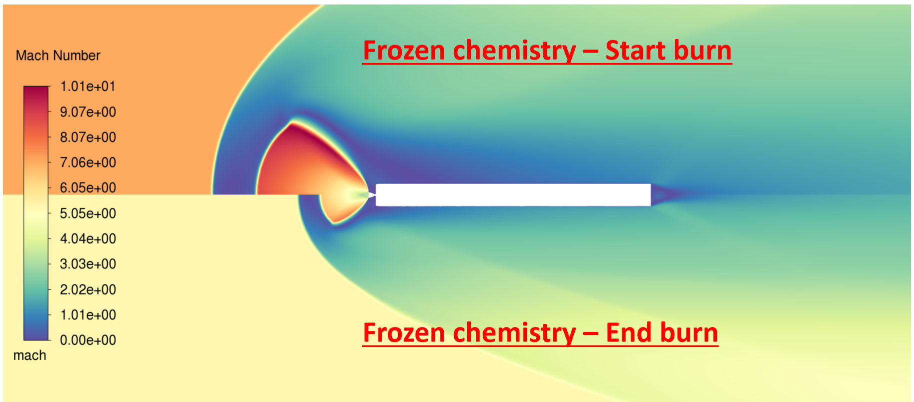

Figure A.1: Comparison start and end burn, frozen chemistry

A.4.2 Chemistry comparison 2D

(a) Chemical equilibrium start burn. Mole fraction of NO (upper half) and O (lower half)

(b) Chemical non-equilibrium start burn. Mole fraction of NO (upper half) and O (lower half)

Figure A.2: Comparison species from chemical reactions during start burn no exhaust.

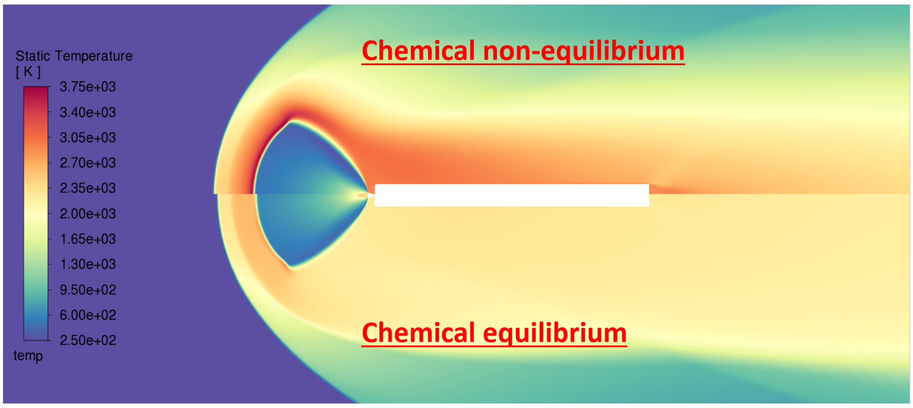

(a) Temperature comparison chemical equilibrium and chemical non-equilibrium

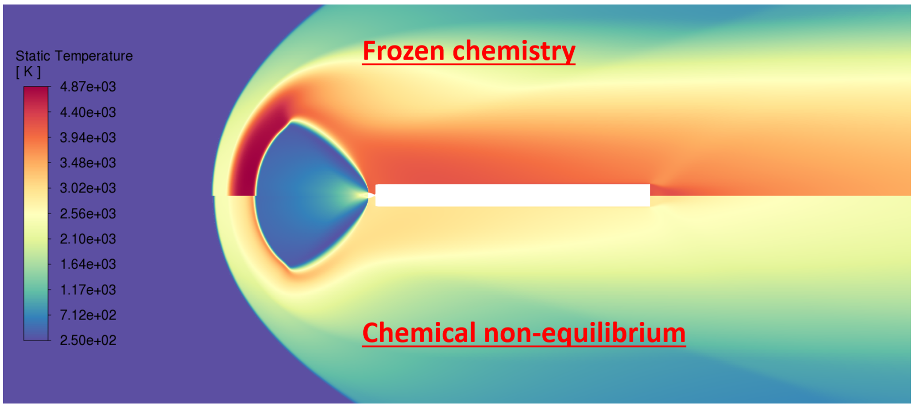

(b) Temperature comparison frozen chemistry and chemical non-equilibrium

Figure A.3: Comparison temperature between chemistry models

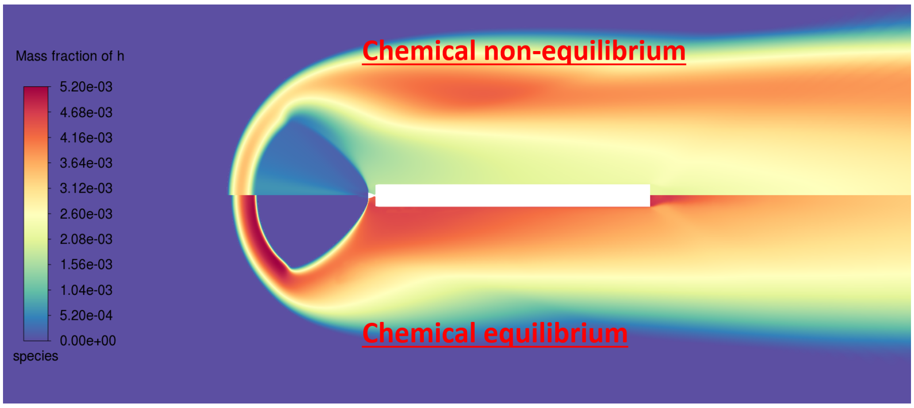

(a) Comparison of massfraction H between chemical equilibrium and chemical non-equilibrium

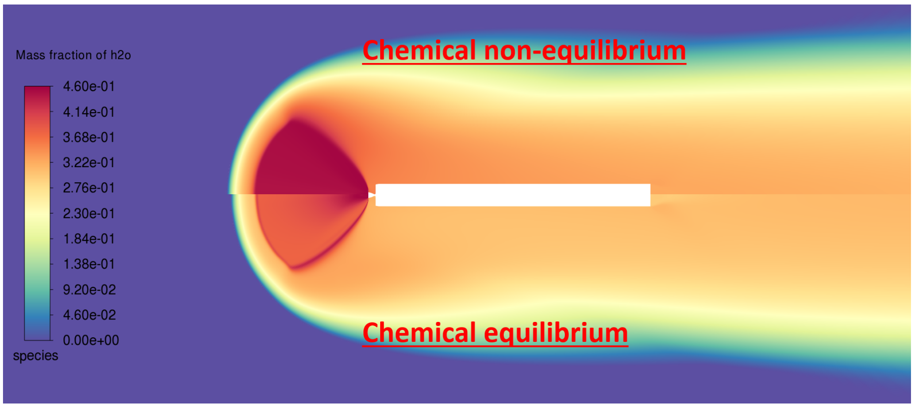

(b) Comparison of massfraction H_2O between chemical equilibrium and chemical non-equilibrium

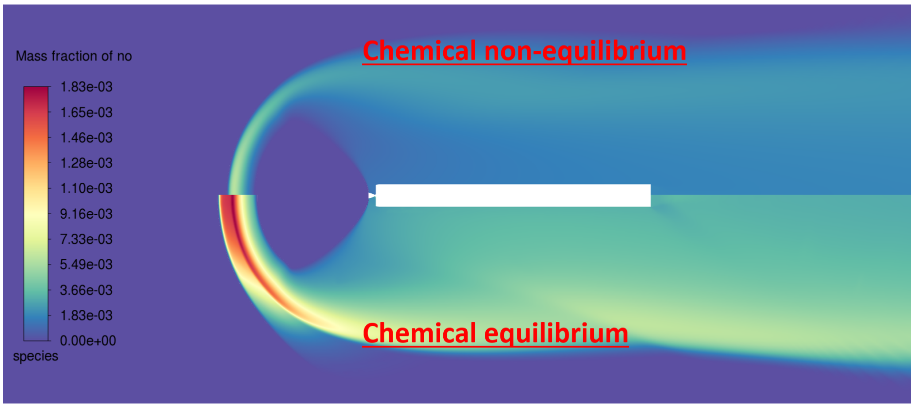

(c) Comparison of massfraction NO between chemical equilibrium and chemical non-equilibrium

Figure A.4: Comparison of species between chemistry models

A.4.3 Species 3D simulations

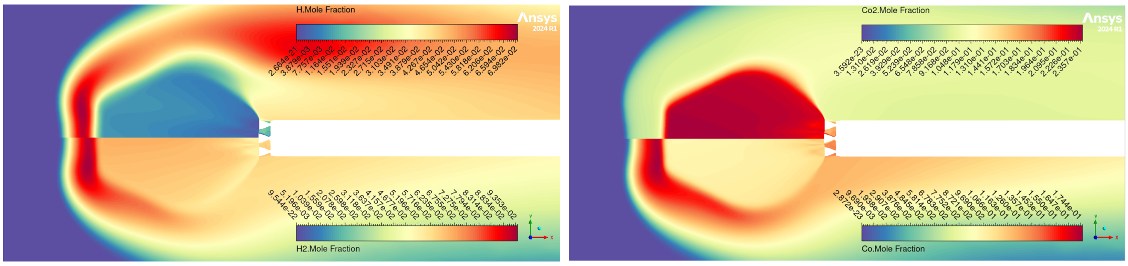

(a) Mole fractions of H (upper) and H_2 (lower).

(b) Mole fractions of CO_2 (upper) and CO (lower).

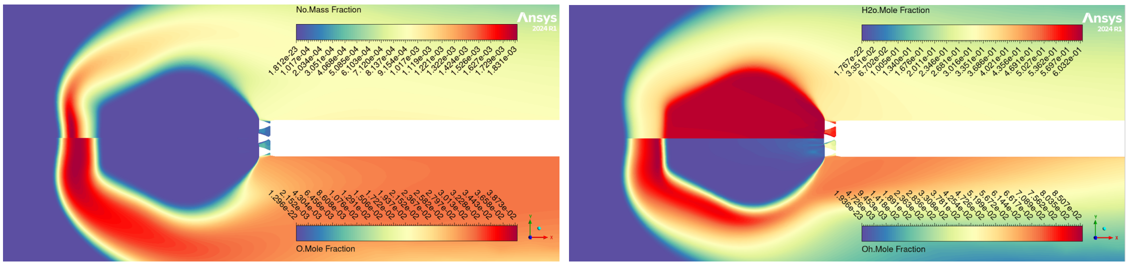

(c) Mole fractions of NO (upper) and O (lower).

(d) Mole fractions of H_2O (upper) and OH (lower).

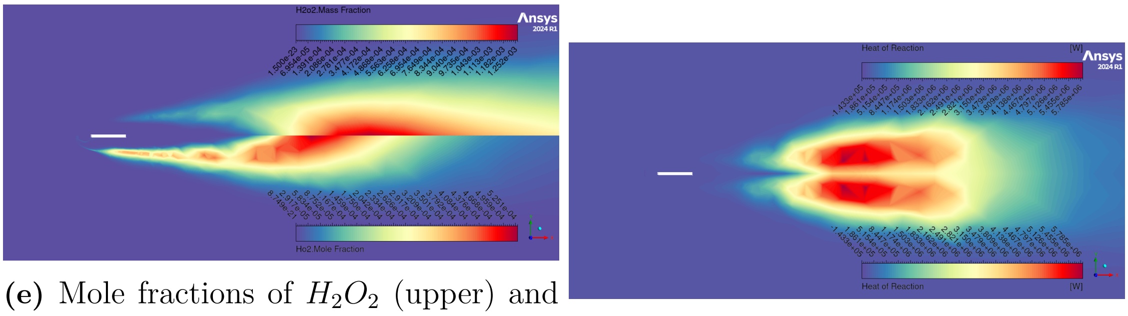

(e) Mole fractions of H_2O_2 (upper) and HO_2 (lower).

(f) Heat production from reaction.

Figure A.5: Species for end burn chemical non-equilibrium.

DEPARTMENT OF MECHANICS AND MARITIME SCIENCE
CHALMERS UNIVERSITY OF TECHNOLOGY
Gothenburg, Sweden
www.chalmers.se

CHALMERS
UNIVERSITY OF TECHNOLOGY